

REPORT DOCUMENTATION PAGE				Form Approved OMB No. 0704-0188	
<p>The public reporting burden for this collection of information is estimated to average 1 hour per response, including the time for reviewing instructions, searching existing data sources, gathering and maintaining the data needed, and completing and reviewing the collection of information. Send comments regarding this burden estimate or any other aspect of this collection of information, including suggestions for reducing the burden, to the Department of Defense, Executive Service Directorate (0704-0188). Respondents should be aware that notwithstanding any other provision of law, no person shall be subject to any penalty for failing to comply with a collection of information if it does not display a currently valid OMB control number.</p> <p>PLEASE DO NOT RETURN YOUR FORM TO THE ABOVE ORGANIZATION.</p>					
1. REPORT DATE (DD-MM-YYYY) 13-08-13		2. REPORT TYPE Final Report		3. DATES COVERED (From - To) 5/01/10 to 4/30/13	
4. TITLE AND SUBTITLE Wave Chaos and HPM Effects on Electronic Systems			5a. CONTRACT NUMBER		
			5b. GRANT NUMBER FA95501010106		
			5c. PROGRAM ELEMENT NUMBER		
6. AUTHOR(S) Thomas M. Antonsen Jr., Edward Ott, John Rodgers, and Steven Anlage			5d. PROJECT NUMBER		
			5e. TASK NUMBER		
			5f. WORK UNIT NUMBER		
7. PERFORMING ORGANIZATION NAME(S) AND ADDRESS(ES) Institute for Research in Electronics and Applied Physics, Dept. of Electrical and Computer Engineering, and Dept. of Physics University of Maryland College Park, MD 20742				8. PERFORMING ORGANIZATION REPORT NUMBER	
9. SPONSORING/MONITORING AGENCY NAME(S) AND ADDRESS(ES) Air Force Office of Scientific Research Dr. Arje Nachman AFOSR/NE (703) 696-8427 DSN 426-8427 FAX (703) 696-8450 E-mail: arje.nachman@afosr.af.mil				10. SPONSOR/MONITOR'S ACRONYM(S) AFOSR	
				11. SPONSOR/MONITOR'S REPORT NUMBER(S)	
12. DISTRIBUTION/AVAILABILITY STATEMENT Unclassified Unlimited					
13. SUPPLEMENTARY NOTES					
14. ABSTRACT <p>We performed research in the field of electromagnetic wave chaos and High Power Microwave (HPM) effects in electronic systems relevant to the coupling of electromagnetic radiation into systems and its effects on systems. Our program addressed the following issues of relevance to the understanding of HPM effects on electronic systems: The extension of a statistical description of wave coupling into enclosures to describe a) the coupling through apertures, b) the coupling to mixed systems for which only part of the ray phase space is chaotic, and c) the coupling to systems of systems in which the components have varying degrees of isolation, for example chains of cavities. The development of time domain models for the response of systems excited by pulses of wave energy, including nonlinear effects. The Extension of HPM upset experimentation and modeling to complex networks of interconnected circuits. Examination of fading, power-delay profiles, and small-signal discrimination in reverberant electroenvironments containing short-ray trajectories.</p>					
15. SUBJECT TERMS High Power Microwaves Wave Chaos Statistical model of coupling					
16. SECURITY CLASSIFICATION OF:			17. LIMITATION OF ABSTRACT	18. NUMBER OF PAGES	19a. NAME OF RESPONSIBLE PERSON
a. REPORT	b. ABSTRACT	c. THIS PAGE			Thomas M Antonsen Jr
UU	UU	UU	UU		19b. TELEPHONE NUMBER (Include area code) 301-405-1635

Final Report: 5/01/10 – 4/30/13

Wave Chaos and HPM Effects on Electronic Systems FA95501010106

By

Thomas M. Antonsen Jr., Edward Ott, John Rodgers, and Steven Anlage

*Institute for Research in Electronics and Applied Physics, Dept. of Electrical and
Computer Engineering, and Dept. of Physics*

University of Maryland

College Park, MD 20742

301-405-1635 (phone)

301-405-1678 (fax)

antonsen@umd.edu, edott@umd.edu, rodgers@glue.umd.edu, anlage@umd.edu

Dr. Arje Nachman AFOSR/NE (703) 696-8427

DSN 426-8427 FAX (703) 696-8450

E-mail: arje.nachman@afosr.af.mil

Summary

We performed research in the field of electromagnetic wave chaos and High Power Microwave (HPM) effects in electronic systems. Our emphasis was on issues likely to be most relevant to the coupling of electromagnetic radiation into systems and its effects on systems, as in electromagnetic attacks of military electronics..

Our program addressed the following issues of relevance to the understanding of HPM effects on electronic systems:

- The extension of the previously developed Random Coupling Model statistical description of wave coupling into enclosures to describe a) the coupling through apertures, b) the coupling to mixed systems for which only part of the ray phase space is chaotic, and c) the coupling to systems of systems in which the components have varying degrees of isolation, for example chains of cavities.
- The further development of time domain models for the response of systems excited by pulses of wave energy, including nonlinear effects

- The Extension of HPM upset experimentation and modeling to complex networks of interconnected circuits. Our aim is to develop a generalized approach for modeling HPM effects in electronic circuits, systems and infrastructures.
- Examination of fading, power-delay profiles, and small-signal discrimination in reverberant electromagnetic environments containing short-ray trajectories.

General theory of HPM coupling to circuits in enclosures through apertures

The RCM is based on the use of Random Matrix Theory (RMT) that has found wide application in mesoscopic and nuclear physics. The model incorporates system-specific information about the near field behavior of the ports of the enclosure, the volume of the enclosure, and a measure of the enclosure's average quality factor, and predicts the statistical behavior of the enclosures scattering parameters (actually the impedance matrix from which the scattering matrix can be obtained). This model was introduced in Refs. 1-3 for a specific geometry, namely planar cavities excited by point like sources. In Ref 6, we developed a formulation of the model for the case of three-dimensional cavities, with arbitrary polarization of the fields inside, with ports that are large compared with a wavelength and with conductors inside that act as antennas. The use of this model allows one to study the coupling process starting from an incident plane wave that penetrates through an aperture, distributing its energy throughout an enclosure and inducing voltages on conductors in the enclosure. This is done by breaking the problem into pieces. The pieces are then combined in the RCM to give a statistical description of the coupling processes.

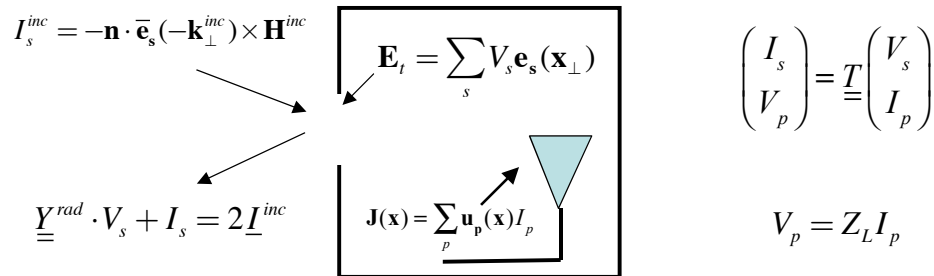


Figure 1: Schematic of an enclosure with an aperture illuminated from the outside and an antenna (representing a circuit element) inside that is connected to a load Z_L . Coupling from the incident wave to the antenna is described by a system of linear matrix equations. Statistics (and the RCM) enter through the T -matrix defined in the text.

Figure 1 illustrates how this is done. A wave is incident on the enclosure illuminating the aperture and is partially reflected. The field on the aperture is represented in a basis of modes with amplitudes V_s . The properties of the aperture are described by the aperture radiation admittance $\underline{\underline{Y}}^{rad} = j \text{Im}[\underline{\underline{Y}}^{rad}] + \underline{\underline{G}}^{rad}$, which gives the amplitudes $I_s = \underline{\underline{Y}}_{ss'}^{rad} V_{s'}$ of the magnetic field basis functions when the enclosure is absent and the aperture radiates into free space. Similarly the currents in the antenna can be represented in a basis of modes with amplitudes I_p . The properties of the antenna are described by its radiation

impedance $\underline{\underline{Z}}^{rad} = j\text{Im}[\underline{\underline{Z}}^{rad}] + \underline{\underline{R}}^{rad}$ giving the voltage on the antenna when radiating into free space. When the antenna (attached to an effective load Z_L) is placed in the enclosure it becomes coupled to the fields in the aperture. The precise characterization of this coupling is a complicated computational electromagnetics problem. However, if the enclosure has chaotic trajectories, the relationship between antenna and aperture voltages and currents is modeled by the matrix $\underline{\underline{T}} = j\text{Im}[\underline{\underline{U}}] + [\underline{\underline{V}}]^{1/2} \cdot \underline{\underline{\xi}} \cdot [\underline{\underline{V}}]^{1/2}$. Here the matrices $\underline{\underline{U}}$ and $\underline{\underline{V}}$ are given in terms of the radiation admittance of the aperture and the radiation impedance of the antenna,

$$\underline{\underline{U}} = \begin{bmatrix} \underline{\underline{Y}}^{rad} & \underline{\underline{0}} \\ \underline{\underline{0}} & \underline{\underline{Z}}^{rad} \end{bmatrix} \quad \text{and} \quad [\underline{\underline{V}}]^{1/2} = \begin{bmatrix} [\underline{\underline{G}}^{rad}]^{1/2} & \underline{\underline{0}} \\ \underline{\underline{0}} & [\underline{\underline{R}}^{rad}]^{1/2} \end{bmatrix}.$$

All the statistics, and coupling between the aperture and antenna, are imbedded in the random matrix $\underline{\underline{\xi}}$ whose properties are given in terms of the eigenfunctions and eigenvalues of a Gaussian Random Matrix and depend only on the average internal losses in the cavity and the average density of modes. The system specific information is provided by the matrices $\underline{\underline{Z}}^{rad}$ and $\underline{\underline{Y}}^{rad}$ that can be computed or measured in isolation from the rest of the system. This formulation provides a compact approach to analyzing coupling for specific configurations based on the properties of the components of the configuration. It has no adjustable parameters. We are currently in the process of testing this formulation in the laboratory.

Distribution of RF power in chains of coupled cavities

Our previous studies focused on the distribution of RF energy throughout a single enclosed space. However, a problem that is often of interest is the distribution of energy

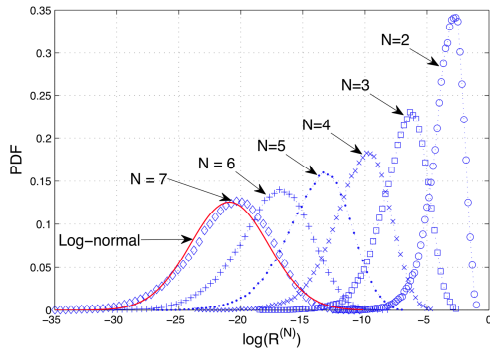


Figure 2 Distributions of power ratios for chains of up to *seven* cavities with moderate losses for a large number of cavities the distribution becomes *log-normal*, from [23]

through a chain of enclosed spaces that are coupled together. These may be either compartments in a vehicle or aircraft, or boxes enclosed within other boxes. We have extended our RCM to the study of the problem of the statistics of fields in a chain of coupled cavities [13]. In the general case, the coupled power is given in terms of a product of random matrices. The distribution of coupled power then has the same statistics as the finite time Lyapunov numbers for a discrete dynamical system. This distribution approaches *log-normal* as the number of cavities (and matrices) is increased. However,

there are significant large deviation departures from *log-normal* which describe the rare cases of large coupled power and are thus of interest. We have derived general expressions for the probability distribution of the power coupled into the N^{th} cavity of a chain in the case in which losses in the cavities is the dominant absorption mechanism.

These expressions, which are in the form of products of system specific factors describing the coupling ports and losses, and universal statistical factors, have been compared with Monte Carlo evaluations of the coupling using the RCM.

Given that the power coupled through a chain of cavities is a product of factors, it is natural that the probability distribution for coupled power tends to *log-normal* as the number of cavities increases. This is illustrated in Fig. 2 where the power transmission factor ($R^{(N)} = \text{power to cavity } N / \text{power to cavity } 1$) for chains of up to seven cavities are plotted for a case in which the cavities have moderate losses ($Q - \text{width equals mode spacing}$). The present model assumes that successive cavities are coupled by ports or transmission lines that support a single mode. In the coming year we intend to extend this to coupling through over-moded or resonant apertures.

Fading in high and low loss environments

Fading is the observation of variations in signal strength measured at a receiver due to time-dependent variations in the propagation of waves from the source, or due to multi-path scattering and interference. It is well known that the quantitative statistical theory of wave chaos - random matrix theory (RMT) - can be successfully applied to predict statistical properties of many quantities, such as the scattering matrix, of a wave chaotic system. We started from the statistical model of the scattering matrix [14] to establish a general fading model valid under all conditions. The model provides a first principles understanding of the most common statistical model used in the communications field, namely Rayleigh fading, and shows that the statistical properties are governed by a single quantity related to the loss or de-phasing parameter of RMT. We also combined the RMT fading model with our random coupling model (RCM) that takes into account system-specific features such as direct and short orbits [13, 25-27], to build a more general fading model that includes Rician fading.

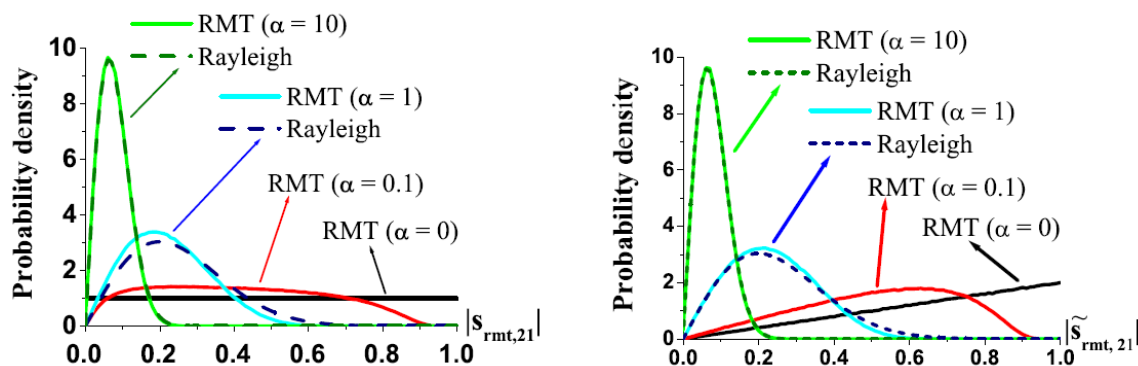


Figure 3: The probability density functions of the fading amplitude $|s_{rmt,21}|$ for the time reversal invariant case (left) and $|\tilde{s}_{rmt,21}|$ for the broken time reversal invariant case (right). Solid curves show the numerical results from the RMT model with different loss parameters ($\alpha = 0, 0.1, 1, 10$). For the higher loss cases ($\alpha = 1$ and $\alpha = 10$), the corresponding Rayleigh distributions are shown as dashed curves.

In the high loss-parameter limit, our model agrees with the Rayleigh/Rice models, however it shows significant deviations from the Rayleigh/Rice distribution in the limit of low loss [17]. We have performed experiments with two ray-chaotic microwave cavities [15-17] to test the RMT/RCM fading model over a wide range of loss parameter values, and our results are in excellent agreement with our theory.

Statistics of field distribution in cavities with both regular and chaotic orbits

This work was included in the Ph.D. thesis of Ming-er Lee, who graduates 8/13. The RCM is based on idea that the ray trajectories describing the propagation of radiation throughout an enclosure are chaotic. However, for some enclosures the walls are flat and facing each other in such a way that some ray trajectories are not chaotic while others are. We have extended our model to an example of such a cavity. We have found that the response of the cavity to excitations in this case can be characterized as a sum of the response of modes whose trajectories are chaotic and modes whose trajectories are not chaotic. The chaotic portion of the response has the same universal features that the RCM predicts. The nonchaotic response of the system has different features that can still be characterized generally, that is, without detailed solution of the field equations in the cavity.

An example of the effect that we consider is illustrated in Fig. 4a and Fig. 4b. Figure 4a shows two eigenmodes (numbers 5005 and 5006) of a two-dimensional mushroom shaped cavity that have nearly the same eigenvalue. The one on the left extends throughout the cavity and corresponds to rays that ergodically fill the cavity, while the one on the right extends mainly to the semicircular region and corresponds to rays bounce along the vertical, horizontal, and outer circular boundary. The histogram for impedances for a port that is placed in the upper right hand side (which will excite both types of mode) of the cavity is shown in Fig. 4b. The histogram is compared with two theories: the red curve corresponds to the case in which all eigenfunctions are supposed to be of the chaotic variety, and the blue curve to the case in which a fraction (as determined by theory) are of the integrable type. As can be seen the theory curve including contributions from both types of eigenfunction matches the computed distribution of impedance values. We are currently generalizing the formulation of this effect to 3D electromagnetic cavities.

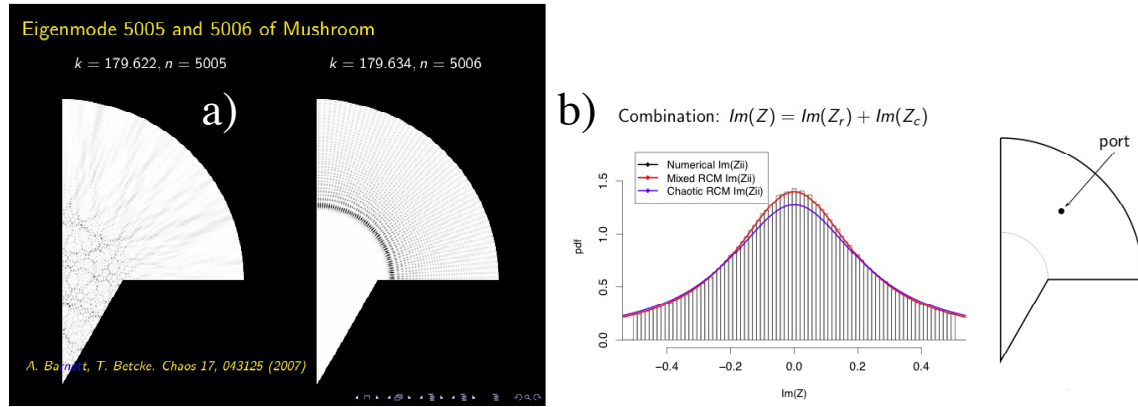


Figure 4: Modes of mushroom shaped cavity. a) two adjacent modes showing reflecting chaotic and regular behavior of classical ray trajectories. b) Histograms of impedance for excitation by a port located in the mushroom cap.

Statistics of tunneling

In collaboration with L. Pecora of NRL we have developed a theory for the coupling of two wave enclosures by a barrier through which waves must tunnel. [18]. The main conclusions of this work is that the mean tunneling rate, which characterizes the coupling between the two enclosures is independent of enclosure shape and only

depends on properties of the tunneling barrier. However, the fluctuations in the tunneling rate from mode to mode depend strongly on the enclosure shape. Enclosures with chaotic ray trajectories have much smaller fluctuations than enclosures with nonchaotic trajectories. This information can aid in design or placement of apertures connecting enclosures to minimize large coupling. This general theory will be tested experimentally in the proposed work as discussed below.

Improving TR wave focusing using iterative techniques

Spatiotemporal focusing of waves has applications in fields such as imaging and communication, but is also extremely useful in inducing HPM effects. Time reversal (TR) mirrors have been used to focus waves in both space and time [19], as discussed above. In practice, TR mirrors have several limitations that result in loss of information about the waves broadcast by the source; these include i) limited coverage by the transceivers, and ii) dissipation during the wave propagation (which breaks TR invariance) [20, 21]. The limitation due to dissipation leads to increasing loss of information as the recording time increases.

The loss of information during the reconstruction results in temporal and spatial sidelobes of the reconstructed pulse. In previous work, we used the compensating technique of exponential-in-time amplification of the rebroadcasted time-reversed signal to partially undo the adverse effects of dissipation, and to enhance the range of sensors which utilize TR mirrors [20, 22]. However, this technique does not improve the temporal focusing of the reconstructed pulse. On the other hand, an iterative TR technique has been shown to be effective in eliminating the spatiotemporal sidelobes of the reconstructed pulse [23]. We introduce into the iteration method an amplification parameter to compensate for dissipation. By tuning this parameter, we can substantially improve the accuracy and convergence of the iterative focusing technique. This is demonstrated both experimentally and numerically [11].

Sensing small perturbations using TR focusing

We demonstrated a remote sensor scheme by applying the quantum mechanical concept of fidelity loss to classical acoustic and electromagnetic waves [8, 9]. The sensor makes explicit use of time-reversal invariance and spatial reciprocity in a wave chaotic system to sensitively and remotely measure the presence of small perturbations. The loss of fidelity is measured by employing a single-channel time-reversal mirror to rebroadcast a probe signal into the perturbed system. We also introduced the use of exponential amplification of the probe signal to partially overcome the effects of propagation losses and to vary the sensitivity.

We then showed that the sensor can be used to quantify a class of perturbations using classical waves. In particular, we investigated perturbations, which change the volume of a strongly scattering wave chaotic cavity, but preserve its shape. The crux of this approach is that the effect of a volume changing perturbation is a change in the frequency spacing of the modes of the cavity. Thus the effect of the perturbation on a response signal from a perturbed cavity can be undone by empirically scaling the phase-information contained along the time-axis of the response signal from the perturbed cavity. The scaling value that undoes the perturbation, and hence quantifies the perturbation, is the ratio of the mode spacing before and after the perturbation. The capability to quantify such volume changing perturbations has been demonstrated both numerically and experimentally. A quasi-1D star graph model [11] was initially used to

demonstrate the results. The quantification of electrical-volume changing perturbations to a one cubic meter aluminum box was demonstrated experimentally; the experimental results are also supported by a finite difference time domain simulation of the full-wave-solution to the time-domain Maxwell's Equations inside the box. Finally, the approach to quantify volume changing perturbations was shown to apply to a generic wave chaotic system by using a time domain version of our Random Coupling Model [24].

Directing wave energy using TR techniques

Nonlinear Time-Reversal Mirror - An ideal time-reversal mirror in an open environment would collect the forward-propagating wave at every point on a closed surface enclosing the transmitter, requiring a very large number of receivers. The receiving array can be simplified, without significant loss of fidelity of the reconstruction, if there is a closed, ray-chaotic environment where a propagating wave (with wavelength

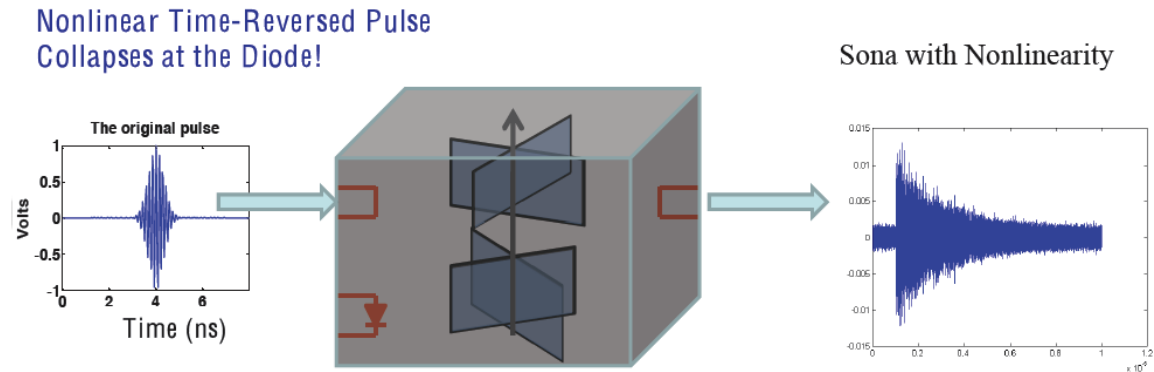


Figure 5 Illustration of the nonlinear time reversal experiment [22]. A pulse is injected at one port of an enclosure. Signals in the enclosure interact with a diode and are then collected at a second port. When that signal is time reversed, filtered, and reinjected, a pulse will form either at the original port or the diode depending on the filter.

much smaller than the size of the enclosure) will eventually reach every point in the environment, allowing the use of a single receiver to capture the signal to be time-reversed. Reconstruction is possible even when only a small fraction of the transmitted energy is collected by the receiver. Now consider a discrete nonlinear element added to the otherwise linear environment. When a waveform is incident on the nonlinear element, excitations are formed at frequencies different from those in the initial pulse. These new excitations appear as a new transmission originating from the nonlinear element, which in principle should be time-reversible in their propagation, and behave similarly to the initial pulse. In particular, the nonlinear excitations should, upon time-reversal, reconstruct as a signal that is focused on the nonlinear element. We have demonstrated this method of nonlinear time-reversal with electromagnetic waves [12] as illustrated in Fig. 5. Furthermore, the generation and time-reversal of nonlinear excitations will not depend upon the location of the object, which may be unknown. This allows creation of an exclusive communication channel with the nonlinear object, and the ability to direct intense energy onto it without interfering with nearby objects.

Experimental studies of circuit effects

Under previous funding a comprehensive program of effects tests on electronic systems lead to characterization of fundamental effects mechanisms from which generalized effects models were developed. A key aspect is illustrated in Fig. 6, which

shows a typical CMOS integrated circuit along with a comparison of results from measurements and simulations. HPM coupled onto the chip is likely to drive semiconductor junctions into nonlinear, non-quasistatic (NQS) regimes of operation. We demonstrated that a modification to the Berkeley (BSIM) device macro-models accurately predicts HPM effects in electronic circuits using commercially available circuit simulators such as CADENCE and Agilent ADS. Our approach involves fabricating basic integrated circuits (IC) and measuring their response when driven by continuous, pulsed and wideband HPM waveforms. The results allow us to characterize the various linear and nonlinear effects transfer functions from which scalable (device-based) macro-models are constructed.

We have shown experimentally that HPM fields couple predominantly to bus wires and board-level interconnects and therefore may be considered as radiation impedances (e.g. as input to RCM). Since the IC dimensions (mm's) are much smaller than typical HPM wavelengths (10's cm), the IC is assumed to be a lumped element excited by the terminal voltages of the interconnects. Everything up to this point in the model is linear. Once the HPM-induced voltage levels and spectra are known the nonlinear device models discussed above are employed to calculate effects.

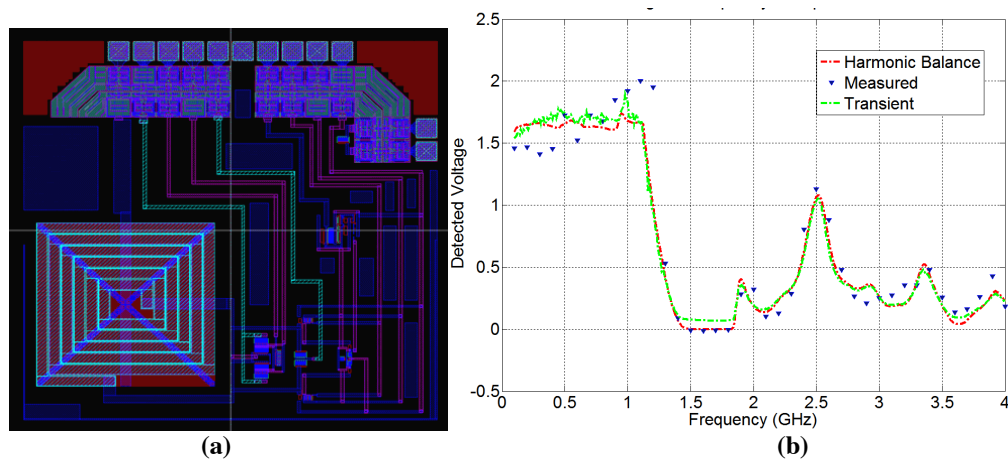


Figure 6: Shown is (a) the VLSI layout of a CMOS integrated circuit and (b) a comparison of the results of measurements and simulation that include a modified MOS channel model that correctly predicts NQS behavior due to HPM excitation.

The capabilities described above will now enable us to design, evaluate and test new concepts for HPM-hardened. We have already evaluated the HPM susceptibility of common and differential mode signaling buses and found that differential busses are 17 dB more robust than SE. Similar improvements aimed at hardening devices, IC boards, system interconnects and electronic enclosures are feasible. Altogether it is likely that vastly superior HPM immunity in mission-critical electronic systems may be achieved.

II. Publications 2011-2012

Journal Articles

1. *Statistical model of short wavelength transport through cavities with coexisting chaotic and regular ray trajectories*, Lee, Ming-Jer; Antonsen, Thomas M.; Ott, Edward,

- PHYSICAL REVIEW E Volume: 87 Issue: 6 , 062906 DOI: 10.1103/PhysRevE.87.062906, JUN 13 2013
2. *Dynamic localization of a weakly interacting Bose-Einstein condensate in an anharmonic potential*, Herrera, M.; Antonsen, T. M.; Ott, E.; et al., PHYSICAL REVIEW A Volume: 87 Issue: 4 Article Number: 041603 DOI: 10.1103/PhysRevA.87.041603, APR 22 2013
 3. *Quantifying volume changing perturbations in a wave chaotic system*, Taddese, Biniyam Tesfaye; Gradoni, Gabriele; Moglie, Franco; et al., NEW JOURNAL OF PHYSICS Volume: 15 Article Number: 023025 DOI: 10.1088/1367-2630/15/2/023025, FEB 15 2013
 4. *Nonlinear Time Reversal in a Wave Chaotic System*, Frazier, Matthew; Taddese, Biniyam; Antonsen, Thomas; et al., PHYSICAL REVIEW LETTERS Volume: 110 Issue: 6 Article Number: 063902 DOI: 10.1103/PhysRevLett.110.063902, FEB 7 2013
 5. *First-principles model of time-dependent variations in transmission through a fluctuating scattering environment*, Yeh, Jen-Hao; Antonsen, Thomas M.; Ott, Edward; et al. PHYSICAL REVIEW E85, 015202 DOI: 10.1103/PhysRevE.85.015202 (2012).
 6. Study of basic effects of HPM pulses in digital CMOS IC inputs. M. Holloway, Z. Dilli, N. Seekhao and J. Rodgers, IEEE Trans. EMC, vol. 54, no. 5, pp. 1017-1027, 2012.
 7. *Fading Statistics in Communications - a Random Matrix Approach*, Yeh, J. -H.; Ott, E.; Antonsen, T. M.; et al., ACTA PHYSICA POLONICA A120, Pages: A85-A88 (2011)
 8. *Chaos regularization of quantum tunneling rates*, Pecora Louis M.; Lee Hoshik; Wu Dong-Ho; et al., PHYSICAL REVIEW E83, 065201 (2011)
 9. *Iterative time reversal with tunable convergence*, Taddese, B. T.; Antonsen, T. M.; Ott, E.; et al., ELECTRONICS LETTERS 47, Pages: 1165-U19, DOI: 10.1049/el.2011.2047 (2011)
 10. *Impedance and power fluctuation in linear chains of wave chaotic cavities*, G. Gradoni, S. M. Anlage, E. Ott, T. Antonsen, Phys. Rev. E (2012).
 11. *Statistical Prediction and Measurement of Induced Voltages on Components within Complicated Enclosures: A Wave-Chaotic Approach*, Sameer Hemmady, Thomas M. Antonsen Jr., Edward Ott, Steven M. Anlage, IEEE Trans. Electromag. Compat., 2011. 10.1109/TEMPC.2011.2177270).
 12. *Sensing small changes in a wave chaotic scattering system*, Taddese, Biniyam Tesfaye; Antonsen, Thomas M.; Ott, Edward; et al., JOURNAL OF APPLIED PHYSICS 108, 114911 DOI: 10.1063/1.3518047 (2010)
 13. *Experimental examination of the effect of short ray trajectories in two-port wave-chaotic scattering systems*, Yeh, Jen-Hao; Hart, James A.; Bradshaw, Elliott; et al., PHYSICAL REVIEW E 82, 041114 DOI: 10.1103/PhysRevE.82.041114 (2010)
 14. *Universal and nonuniversal properties of wave-chaotic scattering systems*, Yeh, Jen-Hao; Hart, James A.; Bradshaw, Elliott; et al., PHYSICAL REVIEW E81, 025201 DOI: 10.1103/PhysRevE.81.025201 (2010)
 15. *Focusing an Arbitrary RF Pulse at a Distance using Time Reversal Techniques*, Sun K. Hong, Biniyam T. Taddese, Zachary B. Drikas, Steven M. Anlage, Tim D. Andreadis, Submitted to IEEE Trans. Microwave Theory Tech..

Conference Proceedings

1. *Wave chaotic characterization of complex cavities: Distributed ports and coupling*, Antonsen T.M. Jr.; Gradoni G.; Anlage S.; et al. 2011 International Symposium on Electromagnetic Compatibility - 2011 International Symposium on Electromagnetic Compatibility - EMC EUROPE Pages: 549-54 (2011).
2. *Wave chaotic analysis of weakly coupled reverberation chambers*, Gradoni Gabriele; Yeh Jen-Hao; Antonsen Thomas M. Jr.; et al., 2011 IEEE INTERNATIONAL SYMPOSIUM ON ELECTROMAGNETIC COMPATIBILITY (EMC) Pages: 202-207 (2011).
3. *Statistical Characterization of Complex Enclosures with Distributed Ports*, Antonsen Thomas M. Jr.; Gradoni Gabriele; Anlage Steven; et al., 2011 IEEE INTERNATIONAL SYMPOSIUM ON ELECTROMAGNETIC COMPATIBILITY (EMC) Pages: 220-225 (2011).
4. *Nonlinear behavior of electrostatic discharge protection structures under high-power microwave excitation: modeling and simulation*, Z. Dilli, A. Akin, M. Holloway, N. Goldsman and J. Rodgers, Proc. IEEE Semicon. Dev. Res. Symp., 2011,
5. *External radiation of complex cavities described by the random coupling model*, Gradoni, G.; Antonsen, T. M.; Anlage, S. M.; et al. IEEE International Conference on Electromagnetics in Advanced Applications (ICEAA) / IEEE-APS Topical Conference on Antennas and Propagation in Wireless Communications (IEEE APWC) / URSI Electromagnetic Environment and Interference Symposium (EEIS) Location: Cape Town, SOUTH AFRICA Date: SEP 02-07, 2012
6. *Coupling of external radiation to circuitry inside complex EM environments*, Gradoni, G.; Antonsen, T. M.; Anlage, S. M.; et al., IEEE International Conference on Electromagnetics in Advanced Applications (ICEAA) / IEEE-APS Topical Conference on Antennas and Propagation in Wireless Communications (IEEE APWC) / URSI Electromagnetic Environment and Interference Symposium (EEIS) Location: Cape Town, SOUTH AFRICA Date: SEP 02-07, 2012
7. *Coupling of external radiation to circuitry inside complex EM environments*, Gradoni, G.; Antonsen, T.M.; Anlage, S.M.; et al., 2012 International Conference on Electromagnetics in Advanced Applications (ICEAA) Location: Cape Town, South Africa Date: 2-7 Sept. 2012
8. *External radiation of complex cavities described by the random coupling model*, Gradoni, G.; Antonsen, T.M.; Anlage, S.M.; et al., 2012 International Conference on Electromagnetics in Advanced Applications (ICEAA) Location: Cape Town, South Africa Date: 2-7 Sept. 2012

III Students Supported 2010-2013

Graduate Students Supported

Trystan Koch
 Nightvid Cole
 Ming-Jer Lee PhD 8/13

Dissertation Title: "Statistical Modeling of Wave Chaotic Transport and Tunneling"

Thesis attached to this document

Mi Jung Jun

Undergraduate Students

Danaiel Haller

IV References

1. Hemmady, X. Zheng, T. M. Antonsen, E. Ott and S. M. Anlage, Phys. Rev. Lett. **94**, 014102 (2005).
2. X. Zheng, T. M. Antonsen and E. Ott, Electromagnetics **26**, 3 (2006).
3. J. Hart, T. M. Antonsen, E. Ott, Phys. Rev. E. **80**, 041109 (2009).
4. J-H Yeh, J. Hart, E. Bradshaw, T. Antonsen, E. Ott, S. Anlage, Phys Rev. E **82**, 041114 (2011).
5. S Hemmady, T. Antonsen Jr., E. Ott, S. Anlage, IEEE Trans EMC, in press. doi: [10.1109/TEMPC.2011.2177270](https://doi.org/10.1109/TEMPC.2011.2177270)
6. T. M. Antonsen, G. Gradoni, S. M. Anlage E. Ott, Proceedings of the 2011 IEEE International Symposium on Electromagnetic Compatibility, pp. 220-225 (2011)
7. E.P. Wigner, Ann. Math **53**, 36 (1951); **62**, 548 (1955); **65**, 203 (1957); **67**, 325 (1958).
8. S. M. Anlage, J. Rodgers, S. Hemmady, J. Hart, T. M. Antonsen, E. Ott, Acta Physica Polonica A **112**, 569 (2007).
9. B. T. Taddese, J. Hart, T. M. Antonsen, E. Ott, and S. M. Anlage, Appl. Phys. Lett. **95**, 114103 (2009).
10. B. Taddese, T. Antonsen, E. Ott, S. Anlage, J. Appl. Phys, **108**, 114911, (2010).
11. B. T. Taddese, T. M. Antonsen, E. Ott, S. M. Anlage, Electronics Letters **47**, 1165-1167 (2011).
12. Matthew Frazier, Biniyam Taddese, Thomas Antonsen, Steven M. Anlage, "Nonlinear Time-Reversal in a Wave Chaotic System," submitted to Phys. Rev. Lett. [arXiv:1207.1667v2](https://arxiv.org/abs/1207.1667v2)
13. Gabriele Gradoni, Thomas Antonsen, and Edward Ott, to be published in Phys Rev A.
14. P. W. Brouwer and C. W. J. Beenakker, Phys. Rev. B **55**, 4695 (1997).
15. Jen-Hao Yeh, *et al.*, Phys. Rev. E **81**, 025201(R) (2010).
16. Jen-Hao Yeh, *et al.*, Phys. Rev. E **82**, 041114 (2010).
17. Jen-Hao Yeh, *et al.*, Phys. Rev. E (Rapid Communications) **85**, 015202 (2012).
18. L. M. Pecora, H. Lee, D.-H. Wu, T. Antonsen, M.-J. Lee, E. Ott, "Chaos regularization of quantum tunneling rates," Phys. Rev. E **83**, 065201 (2011).
19. FINK, M. : 'Time reversal in acoustics'. Contemp. Phys., 1996, 37, 95.
20. Taddese, B.T., Hart, J., Antonsen, T.M., Ott, E., and Anlage, S.M. : 'Sensor Based on Extending the Concept of Fidelity to Classical Waves'. Appl. Phys. Lett., September 2009, 95, 114103.
21. Draegger, C., and Fink, M. : 'One-Channel Time Reversal of Elastic Waves in a Chaotic 2D-Silicon Cavity'. Phys. Rev. Lett., July 1997, 79, 407-410.
22. Taddese, B.T., Antonsen, T.M., Ott, E., and Anlage, S.M. : 'Sensing Small Changes in a Wave Chaotic Scattering System'. J. Appl. Phys., December 2010, 108, 114911.

23. Montaldo, G., Tanter, M., Fink M. : 'Real time inverse filter focusing through iterative time reversal'. J. Acoust. Soc. Am., February 2004, Vol. 115, 2, pp. 768-775.
24. J. A. Hart, *et al.*, Phys. Rev. E 79, 016208 (2009).

ABSTRACT

Title of dissertation: **STATISTICAL MODELING OF WAVE
CHAOTIC TRANSPORT AND TUNNELING**

Ming-Jer Lee, Doctor of Philosophy, 2013

Dissertation directed by: Professor Edward Ott
Professor Thomas Antonsen
Department of Physics

This thesis treats two general problem areas in the field of wave chaos.

The first problem area that we address concerns short wavelength tunneling from a classically confined region in which the classical orbits are chaotic. We develop a quantitative theory for the statistics of energy level splittings for symmetric chaotic wells separated by a tunneling barrier. Our theory is based on the random plane wave hypothesis. While the fluctuation statistics are very different for chaotic and non-chaotic well dynamics, we show that the mean splittings of differently shaped wells, including integrable and chaotic wells, are the same if their well areas and barrier parameters are the same. We also consider the case of tunneling from a single well into a region with outgoing quantum waves.

Our second problem area concerns the statistical properties of the impedance matrix (related to the scattering matrix) describing the input/output properties of waves in cavities in which ray trajectories that are regular and chaotic coexist (i.e., ‘mixed’ systems). The impedance can be written as a summation over eigenmodes

where the eigenmodes can typically be classified as either regular or chaotic. By appropriate characterizations of regular and chaotic contributions, we obtain statistical predictions for the impedance. We then test these predictions by comparison with numerical calculations for a specific cavity shape, obtaining good agreement.

STATISTICAL MODELING OF WAVE CHAOTIC TRANSPORT AND TUNNELING

by

Ming-Jer Lee

Dissertation submitted to the Faculty of the Graduate School of the
University of Maryland, College Park in partial fulfillment
of the requirements for the degree of
Doctor of Philosophy
2013

Advisory Committee:
Professor Edward Ott, Chair/Advisor
Professor Thomas Antonsen, Co-Advisor
Professor Steven Anlage
Professor Adil Hassam
Professor Michelle Girvan

© Copyright by
Ming-Jer Lee
2013

Table of Contents

List of Figures	iv
1 Introduction	1
1.1 Introduction	1
1.2 Billiard	5
1.3 Spectrum	8
1.3.1 Weyl's Formula and Normalized Spacing	8
1.3.2 Random Matrix Theory	8
1.3.3 Level Spacings for Regular Systems	10
1.3.4 Level Spacing for Mixed Systems	10
1.4 Random Plane Wave Hypothesis	11
1.5 Outline of Dissertation	12
2 Theory of Chaos Regularization of Tunneling in Chaotic Quantum Dots	14
2.1 Introduction	14
2.2 Perturbation Theory for the Statistics of Energy Level Splitting for Chaotic Wells	19
2.2.1 Setup	19
2.2.2 Boundary Condition at $x = 0^-$	19
2.2.3 Perturbation expansion	21
2.3 Evaluation of ΔE for Chaotic Eigenfunctions	23
2.4 Monte Carlo Evaluation of Energy Splittings	30
2.5 Green's Function Analysis of Sliding Average of Splittings	35
2.6 Discussion and Conclusion	39
2.6.1 Variance of the Splittings for Large kL and Large $k_B\Delta$	42
2.6.2 Escape Rate from a Chaotic Well to an Open Region	45
2.6.3 Model for the Upper and Lower Bounds on the Splitting Vari- ance	47
3 Statistical Model of Short Wavelength Transport Through Cavities with Co- existing Chaotic and Regular Ray Trajectories	51
3.1 Introduction	51
3.2 Review of Theory	53
3.2.1 Impedance of a cavity	53
3.2.2 Random Coupling Model	57
3.2.3 Impedance in Mixed Systems	61
3.2.4 Mushroom Billiard	62
3.3 Numerical Experiment	67
3.4 Discussion	74
4 Conclusions and Future Work	76
A Efficient Way to Calculate Eigenvalues of Gaussian Random Matrices	78

B	Method of Particular Solutions	83
B.1	Introduction	83
B.2	Method of Particular Solutions	84
B.3	Scaling Method for MPS	86
B.4	Over Counting Eigenmodes	89
B.5	Choice of Basis	90
C	Statistics of Eigenmode	96
C.1	Chaotic Billiard	96
C.2	Mixed Billiard	97
D	Random Wave Model with Boundary Conditions	102
E	Lorentzian Distribution of the Regular Normalized Impedance	105
	Bibliography	108

List of Figures

1.1	First 100 bounces of two trajectories (blue and red) started at the same point with slightly different initial directions in integrable (a)square billiard (b)quarter circle billiard.	5
1.2	First 100 bounces of two trajectories (blue and red) started at the same point with slightly different initial directions in chaotic billiards (a)Sinai billiard (b)Stadium billiard.	6
1.3	First 100 bounces of two trajectories (blue and red) started at the same point with slightly different initial directions in the mushroom billiard (a)chaotic (b)integrable.	6
2.1	Symmetrical double wells of area A separated by a tunneling potential barrier of width 2Δ , length L and height V_B . (a) shows the case of rectangular wells, while (b) shows a case in which all typical orbits are chaotic.	15
2.2	Energy level splittings versus energy plotted as black dots, along with the sliding average (red), $\langle \Delta E \rangle_{E,\epsilon}$. The parameters used in there plots are $V_B = 1000$, $\Delta_B = 0.05$, $L = 2.423$, $A = 4.8$	16
2.3	Sliding average versus E	18
2.4	Propagation directions.	26
2.5	Comparison of (a) sliding average splittings, $\langle \Delta E \rangle$, and (b) sliding average splitting variances, $\sigma_{\Delta E}$, versus E_0 for numerical data (black), Eq. (2.37) (red) and Eq. (2.37) with its denominator replaced by one (green).	32
2.6	Symmetrical double wells of area A separated by a non perfectly coupled tunneling potential barrier of width 2Δ , barrier length L , height V_B and wall length w	33
2.7	(a)Analogous to Fig. 2.5(a) but for Fig 2.6. (b)Analogous to Fig. 2.5(b) but for Fig 2.6.	34
2.8	Geometry for the Green's function.	37
2.9	Tunneling from a single well into an unconfined region.	41
2.10	For $kL/\pi \ll 1$, the angle $\delta \cong \sqrt{2\pi/kL}$	44
2.11	Model billiard for the analysis in Sec. 2.6.3.	48
3.1	(a) Top view of the quasi-two dimensional cavity coupling with $M = 2$ ports (fed by coaxial transmission lines), where the region interior to the cavity is denoted Ω . (b) Side view of the cavity at a port. In some previous works, a mushroom billiard similar to that in (a) was used [60], but the billiard section below the quarter circular cap being a rectangle of width ρ_0 . This, however, introduced neutrally stable ray orbits that bounce back and forth horizontally between the vertical walls of the rectangle. By using the above triangular bottom part (as in Ref. [63]) (a) we avoid the non-generic effects of such orbits. . . .	55

3.2	(a) Two regular orbits with slightly different initial conditions. (b) Two chaotic orbits with slightly different initial conditions.	64
3.3	(a) Magnitude squared of the $n \approx 10,002$ -th eigenmode (regular) and $k_n \approx 253.496413$. (b) $n \approx 10,003$ -th eigenmode (chaotic) and $k_n \approx 253.501722$	65
3.4	(a) Regular eigenmode, $\phi_{14,3}(\vec{x})$, in Ω . (b) Corresponding magnitude of the normal derivative of $\phi_{14,3}(\vec{x})$ versus s	68
3.5	Numerical calculation of $\xi_{C,ii}$ (red triangle) and $\xi_{C,ij}$ (black square) in the mushroom cavity vs. energy (k^2).	70
3.6	Plot of the probability density function from numerical solution (black histogram) and mean probability density function from Monte Carlo simulation (red solid curve), Eq. (3.44), with root mean squared error bounds (blue dashed curve), Eq. (3.45). The black and red dots are the position of coaxial transmission lines (ports) in case (a) one port in chaotic region and the other in mixed region (b) both pots in chaotic region (c) both ports in mixed region.	72
3.7	Plot of the probability density function of $\xi_{ij} = \xi_{R,ij} + \xi_{C,ij}$ from numerical eigenmode solution (black histogram), our statistical model that treats regular and chaotic contributions separately (red solid curve), and previous statistical model that assumes that all eigenmodes are chaotic (blue dashed curve). The black and red dots are the position of coaxial transmission lines (ports) in case (a) one port in chaotic region and the other in mixed region (b) both pots in chaotic region (c) both ports in mixed region. The insets show the probability density function of the regular contribution, $\xi_{R,ij}$, for numerical eigenmode solutions (black histogram) and for the approximate eigenmode in Eq. (3.32) (red solid curve).	73
A.1	Comparison between average time required to solve the eigenvalues of a $N \times N$ GOE matrix using (black) Eq.(A.1) and (red) Eq.(A.17) in log-log plot.	81
B.1	Illustration of over counting eigenmodes.	90
B.2	Difference between mode counting function from numerical calculated eigenmodes (black solid curve) including over counting eigenmodes (red solid curve) excluding over counting eigenmodes and Weyl's formula prediction. The vertical blue dashed line label the location of over counting eigenmodes.	90
B.3	(a) Stadium billiard and (b) Mushroom billiard.	91
B.4	The first 10 engenmodes of the stadium billiard, shown as density plots. Eigenvalue increases rightwards from the top left.	92
B.5	Density plot of the 10 engenmodes of the stadium billiard whose eigenenergies $k_n^2 \in (39139, 39191)$, at $n \approx 10000$	93
B.6	The first 9 engenmodes of the mushroom billiard, shown as density plots. Eigenvalue increases rightwards from the top left.	94

B.7	Density plot of the 9 engenmodes of the mushroom billiard whose eigenenergies $k_n^2 \in (64234, 64285)$, at $n \approx 10000$	95
C.1	Comparison between the probability density function of normalized nearest neighbor eigenvalue spacings of (black histogram) stadium billiard and (red curve) Wigner GOE distribution.	97
C.2	Comparison between (black histogram) the probability density function of the first 23,072 eigenfunction amplitudes of the stadium billiard at different position (see inset) and (red curve) Gaussian distribution.	98
C.3	(a) Comparison between the probability density function of normalized nearest neighbor chaotic eigenvalue spacings of (black histogram) mushroom billiard and (red curve) GOE matrix. (b) Comparison between (black histogram) the probability density function of normalized nearest neighbor regular eigenvalue spacings of mushroom billiard and (red curve) Poisson distribution. (a) Comparison between (black histogram) the probability density function of normalized nearest neighbor eigenvalue spacings of mushroom billiard and (red curve) Berry-Robnik distribution.	99
C.4	Comparison between (black histogram) the probability density function of the first 19,198 chaotic eigenfunction amplitudes of the mushroom billiard at different position (see inset) and (red curve) Gaussian distribution.	100
C.5	The probability density function of the first 19,916 regular eigenfunction amplitudes of the mushroom billiard at different position (see inset).	101
D.1	(a) Stadium Billiard (b) Comparison between (Black Dots) average over $n = 1, \dots, 23072$ of numerical calculated $\phi_n^2(r)$ and (red curves) Eq. (D.10).	104

Chapter 1

Introduction

1.1 Introduction

According to the correspondence principle, the predictions of quantum and classical mechanics should coincide in the limit of short quantum wavelength.

It is particularly interesting to investigate possible manifestations of the correspondence principal in situations where the quantum and classical pictures display seemingly different fundamental properties. For example, classical mechanics, being nonlinear, may commonly yield chaos, while quantum mechanics, e.g., as described by the Schrödinger wave equation, is linear and thus cannot yield chaotic dynamics in the usual classical sense (exponential sensitivity of bounded solutions to small perturbation). Thus, the short wavelength quantum manifestations of chaos in a corresponding classical system has attracted much attention [1, 2, 3, 4, 5], and the study of this issue has been given the appellation ‘quantum chaos’.

An early consideration that later turned out to be important for wave chaos was provided by Wigner who considered energy levels of large nuclei [6, 7, 8, 9, 1, 2]. Since the energy level density at high energy is rather dense and the solution of the wave equation for the levels was inaccessible, Wigner looked for a statistical description of these levels. In recent years, the statistical approach to properties of the solutions of wave equations in systems where the ray trajectories (e.g., classical

orbits of quantum systems) are chaotic has been a very active area, and much work has been done; examples include optical [10], acoustic [11], microwave [12, 13, 14, 15] and electronic cavities [16, 17]. Here, we focus on quasi-two-dimensional microwave cavities and quantum dots, both of which are assumed to be thin in the vertical direction and have ray trajectories which may be chaotic in the other two dimensions (‘billiards’). In Chapter 2, we consider what happens when there is a tunneling barrier in the billiard region, while in Chapter 3 we consider coupling to an external environment through suitable openings (called ‘leads’ or ‘ports’).

With respect to our work in Chapter 3, we note that statistical properties in chaotic cavities with external connections have been well studied using various approaches, e.g., the ‘Poisson Kernel’ [18, 19, 20, 21, 14] or the ‘Random Coupling Model’ (RCM) [12, 13, 14, 15]. However, in general, such systems may have not only either all chaotic or all regular orbits, but also typically have a mixture of coexisting chaotic and regular orbits. We called such systems ‘mixed’. Mixed systems, in spite of their wide occurrence, have been little studied in the previous literature on wave chaos. Extending the application of the RCM to mixed systems is the goal of Chapter 3.

With respect to our work in Chapter 2, we note that, in addition to chaos, the quantum phenomenon of tunneling through classically forbidden regions of phase space presents another striking difference between quantum and classical mechanics. Much past work examining the issue of tunneling in classically chaotic systems has been done (e.g., Refs. [22, 23, 24, 25, 26, 27, 28, 29, 30, 31, 32, 33, 34, 35, 36] and references therein). For example, one question that has been extensively studied is

what happens when a quantum state is initially localized in an integrable region of classical phase space and tunnels through to a chaotic region [22], which is often called dynamical tunneling. In contrast, in Chapter 2, as in Refs. [33, 34, 37], we consider the problem of quantum tunneling from a chaotic region through a classical barrier in the absence of an integrable region. While Refs. [33, 34, 37] treat this problem in the case of smoothly varying potentials with spatially narrow tunneling paths (e.g. ‘instantons’), our concern will be the two-dimensional case where there are piecewise-uniform potentials, long barriers, and confining hard walls [38]¹.

An important point is that smooth Hamiltonians (e.g., $H = (\mathbf{p}^2/2m) + V(\mathbf{q})$ with $V(\mathbf{q})$ smooth function of \mathbf{q}) with completely chaotic dynamics treated in [33, 34, 37] typically do not occur [although they may be thought to approximate systems where regular regions occupy a small fraction of the allowed phase space volume]. On the other hand, completely chaotic phase space dynamics does occur for billiard systems (zero potential regions bounded by hard walls, Sec. 1.2). Because of the flexibility of billiard systems in allowing various types of dynamics (chaotic, non-chaotic, or mixed) this thesis will concentrate on such systems. Other motivations for considering billiard-type systems include: (i) they are potentially realizable in quantum dot contexts and in descriptions of classical optical electromagnetic fields in piecewise-constant dielectrics; (ii) by adjusting the shape of the billiards, it is

¹In contrast with the billiard-type classical chaos that we treat, smooth Hamiltonians typically yield mixed phase spaces with coexisting chaotic and regular regions. In fact, we are aware of only one instance where a smooth Hamiltonian system has been claimed to be fully chaotic, namely, the anisotropic Kepler problem with zero angular momentum.

particularly easy to go from integrable to mixed to chaotic phase space; (iii) comparisons between different shape billiards (e.g., between an integrable and a chaotic case) can be made quantitatively precise by keeping certain gross parameters equal (see Sec. 2.1).

For example, with respect to point (iii) above, a major result of Chapter 2 is that integrable and chaotic cases with the same mean wave tunneling properties differ very greatly in their fluctuation characteristics, with the chaotic case having much smaller fluctuations about the common mean than the integrable case. We believe that, in the billiard case discussed here, point (iii) makes this effect a particularly dramatic instance of a quantum manifestation of classical chaos. We remark that this relative suppression of tunneling fluctuations in the chaotic case occurs because, due to the classical ergodicity of chaotic systems, the quantum states are relatively similar in that they typically effectively spread over the entire classically allowed phase space. In contrast, in integrable systems, due to the existence of extra constants of the motion, different energy states are typically constrained to have much more variation of their distribution in phase space and may avoid the phase space region where tunneling is strongly excited. If so, the tunneling can be exponentially small and very dependent on the particular state. This point, already inherent in the discussions in Refs. [33, 34, 37], applies to both the case of billiard type Hamiltonians and the case of smooth Hamiltonians (e.g., see Fig. 2 of Ref. [33]).

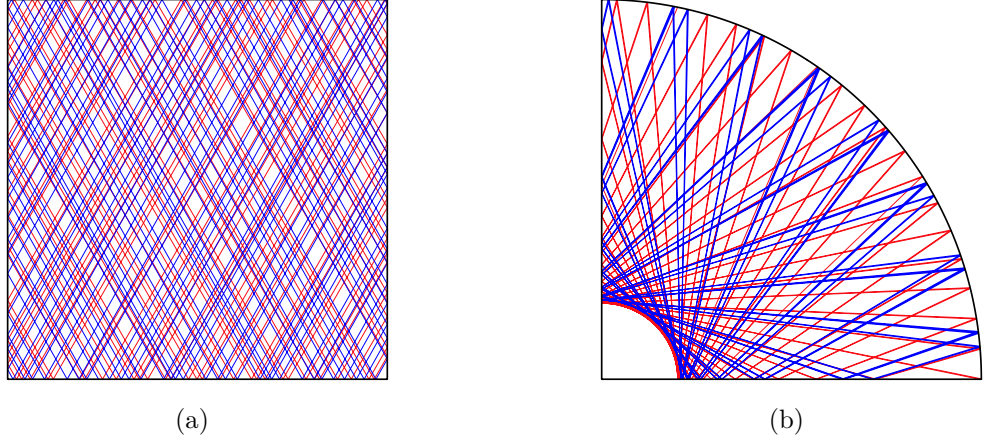


Figure 1.1: First 100 bounces of two trajectories (blue and red) started at the same point with slightly different initial directions in integrable (a)square billiard (b)quarter circle billiard.

1.2 Billiard

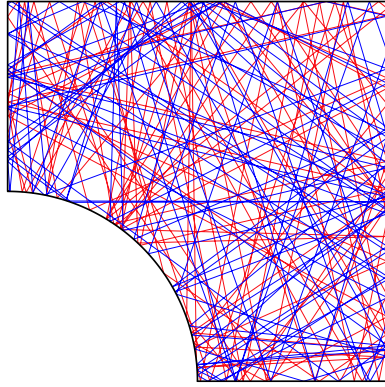
Classically, a billiard is a dynamical system in which a particle moves in a straight line, with constant energy, in a confined region, Ω , and is reflected specularly at the boundary, $\partial\Omega$, without change of speed. Billiard systems have a simple Hamiltonian,

$$H(\mathbf{p}, \mathbf{q}) = \frac{|\mathbf{p}|^2}{2m} + V(\mathbf{q}), \quad (1.1)$$

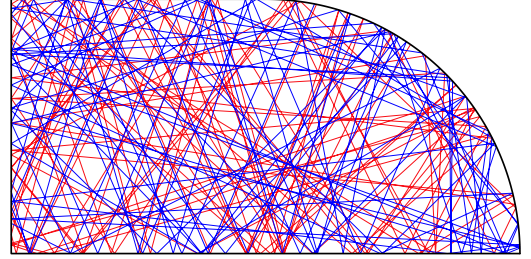
where

$$V(\mathbf{q}) = \begin{cases} 0 & \text{for } \mathbf{q} \in \Omega, \\ \infty & \text{for } \mathbf{q} \notin \Omega, \end{cases} \quad (1.2)$$

but the particle trajectory inside different billiards can have three different behaviors (a) regular, (b) chaotic, and (c) a mixture of regular and chaotic. The shape of the boundary determines which types of trajectories exist in the billiard (see Figs. 1.1, 1.2, and 1.3).

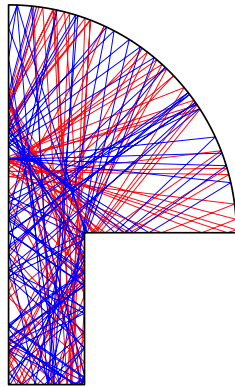


(a)

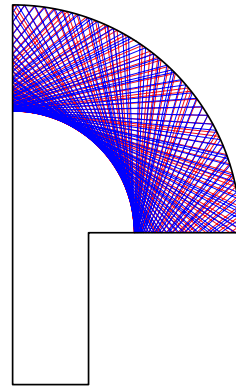


(b)

Figure 1.2: First 100 bounces of two trajectories (blue and red) started at the same point with slightly different initial directions in chaotic billiards (a)Sinai billiard (b)Stadium billiard.



(a)



(b)

Figure 1.3: First 100 bounces of two trajectories (blue and red) started at the same point with slightly different initial directions in the mushroom billiard (a)chaotic (b)integrable.

Considering the quantum billiard, the Hamiltonian of the time-independent Schrödinger equation, $\hat{H}\phi = E\phi$, is replaced by the classical Hamiltonian, Eqs. (1.1, 1.2), i.e.,

$$-\frac{\hbar^2}{2m}\nabla^2\phi_n(\mathbf{q}) = E_n\phi_n(\mathbf{q}) \quad \text{for } \mathbf{q} \in \Omega, \quad (1.3)$$

where ϕ_n and E_n , $n = 1, 2, \dots, \infty$ are real eigenfunctions and eigenvalues, and the infinite potential outside the region translates to the Dirichlet boundary conditions:

$$\phi_n(\mathbf{q}) = 0 \quad \text{for } \mathbf{q} \notin \Omega. \quad (1.4)$$

The eigenfunctions are chosen to be orthogonal:

$$\int_{\Omega} \phi_m^*(\mathbf{q})\phi_n(\mathbf{q})d\mathbf{q} = \delta_{mn}. \quad (1.5)$$

With $k_n^2 = 2mE_n/\hbar^2$, this free-field Schrödinger equation is the same as the Helmholtz equation,

$$(\nabla^2 + k_n^2)\phi_n(\mathbf{r}) = 0. \quad (1.6)$$

The relation between the Schrödinger equation and the Helmholtz equation implies that quantum billiards can be modeled by microwave cavity of a given shape, thus opening a door to experimental verification. In particular, we note that the vertical electric field of modes in a microwave cavity that is vertically thinner than a half-wavelength satisfy (1.6) in two dimensions with Dirichlet boundary conditions.

1.3 Spectrum

1.3.1 Weyl's Formula and Normalized Spacing

For a d -dimensional wave equation, $(\nabla^2 + \lambda^2)\phi = 0$, in a region Ω of volume V , the number N of eigenmodes with λ^2 below k^2 can be described by the Weyl's formula [39],

$$N(k^2) = (2\pi)^{-d} V k^d + O(k^{d-1}). \quad (1.7)$$

Note that the boundary condition of the Helmholtz equation will have a small effect of $O(k^{d-1})$ in the mode counting formula (1.7). Specifically, for 2-dimensional wave equation in a region Ω of area A , the number of eigenmodes below than k^2 is

$$N(k^2) = \frac{A}{4\pi} k^2 + O(k), \quad (1.8)$$

or the mode density is

$$\bar{\rho}(k^2) \cong \frac{A}{4\pi}. \quad (1.9)$$

Thus, the average spacing between eigenvalues $[\Delta(k^2) = k_{n+1}^2 - k_n^2 \text{ for } k_n^2 \cong k^2]$ is

$$\Delta(k^2) = \frac{1}{\bar{\rho}(k^2)} = \frac{4\pi}{A}. \quad (1.10)$$

We define the normalized eigenvalue spacing using the average spacing between eigenvalues, as follows

$$s_n \equiv \frac{k_{n+1}^2 - k_n^2}{\Delta}. \quad (1.11)$$

1.3.2 Random Matrix Theory

Random matrices were introduced by Eugene Wigner to model the spectra of heavy nuclei. Since the energy levels at high energy are rather dense, and the wave

equation was difficult to solve, Wigner sought a statistical description for properties of the spectrum. Wigner hypothesized that the eigenvalue spectrum of complicated nuclei have similar statistical properties to those of the spectra of ensembles of random matrices that depend only on the symmetry of the Hamiltonian.

This led Wigner to consider three types of random matrix ensembles, called Gaussian Orthogonal Ensembles (GOE), Gaussian Unitary Ensembles (GUE) and Gaussian Symplectic Ensembles (GSE). In this thesis, we will be concerned with GOE ensembles which are defined to have the following two properties.

- The ensemble is invariant under every orthogonal transformation

$$\mathbf{H} \rightarrow \mathbf{O}^T \mathbf{H} \mathbf{O} \quad (1.12)$$

where \mathbf{O} is any real orthogonal matrix, $\mathbf{H}^T = \mathbf{H}$ and \mathbf{H} is real.

- The various elements $H_{kj}, k \leq j$, are statistically independent and

$$H_{ij} = H_{ji} \sim \begin{cases} N(0, 1) & \text{for } i = j \\ N(0, 1/2) & \text{for } i \neq j, \end{cases} \quad (1.13)$$

where $N(\mu, \sigma^2)$ is a Gaussian random variable with mean μ and variance σ^2 .

For the GOE ensemble, Wigner found that the distribution of normalized spacing (see Eq. (1.11)) obeyed

$$P_{GOE}(s) \cong \frac{\pi}{2} s \exp\left(-\frac{\pi}{4} s^2\right) \quad (1.14)$$

$$(1.15)$$

In a foundational paper for quantum chaos, the Bohigas-Giannoni-Schmit (BGS) [40] conjectured that the short wavelength spectral statistics of quantum

systems whose classical counterparts exhibit chaotic behavior are described by random matrix theory, and they numerically tested that (1.14) was satisfied for the billiard of Fig. 1.2.

1.3.3 Level Spacings for Regular Systems

In a classically integrable systems, Berry and Tabor [41] showed that corresponding solution of the Schrödinger equation has energy levels that are uncorrelated and that the normalized level spacing distribution is

$$P_{Poisson}(s) = e^{-s}. \quad (1.16)$$

1.3.4 Level Spacing for Mixed Systems

Consider a system whose classical phase space has both regular and chaotic regions, and denote the total volume ratio of the regular regions by ρ_r and the volume ratio of the chaotic region by ρ_c . Percival conjectured that, in the semi-classical limit, the energy levels consist of regular and chaotic parts having certain distinct properties [42]. Berry and Robnik extended this conjecture and assumed that the sequence of the energy levels of a mixed system is given by the superposition of statistically independent sub-sequences corresponding to the classical phase-space regions [43]. In addition, they assumed that the distributions of the sub-sequences corresponding to regular and irregular regions are, respectively, the Poisson and Wigner distributions, see Eqs. (1.14) and (1.16).

1.4 Random Plane Wave Hypothesis

The motivation for the random plane wave hypothesis is the observation that ray trajectories in chaotic billiards (see Figs. 1.2) are distributed uniformly in space and isotropically in direction. Correspondingly, Berry [44] proposed that at any point, not too close to the boundary, the eigenfunction of $(\nabla^2 + k_n^2)\phi_n = 0$ has statistical properties approximately similar to those of a random superposition of many plane waves with same wavenumber, k_n ,

$$\phi_n(\mathbf{x}) \cong \sum_{j=1}^N \alpha_j \exp(i k_n \hat{\mathbf{e}}_j \cdot \mathbf{x} + i \theta_j) + (\text{complex conjugate}), \quad N \gg 1, \quad (1.17)$$

where the amplitude α_j 's are identical independently distributed random variable with some probability density function, the direction $\hat{\mathbf{e}}_j$ are independent isotropically distributed random unit vectors, the phase θ_j are independent uniformly distributed in $[0, 2\pi)$ random variables, and (1.17) is assumed to hold when $2\pi/k_n$ is small compared to a typical length dimension of the billiard. Based on the central limit theorem, it is thus expected that the eigenfunction amplitude $\phi_n(\mathbf{x})$ at any given point \mathbf{x} is Gaussian distributed with zero mean and the variance is $1/V$, where V is the volume of the closed region, i.e.,

$$P_{\mathbf{x}}(\phi) = \frac{1}{2\pi\sigma^2(\mathbf{x})} \exp\left[-\frac{\phi^2}{2\sigma^2(\mathbf{x})}\right], \quad (1.18)$$

where $\sigma^2(\mathbf{x}) = 1/V$ ($\sigma^2(\mathbf{x}) = 1/V$ follows from the normalization condition (1.5)).

From the random plane wave hypothesis, Berry [44] show that the two-point correlation function in a d-dimensional billiard is

$$C(\mathbf{r}_1, \mathbf{r}_2; k) = \frac{1}{V} \Gamma(d/2) \frac{J_{(d-2)/2}(kL)}{(kL)^{(d-2)/2}}, \quad (1.19)$$

where $L = |\mathbf{r}_1 - \mathbf{r}_2|$, V is the d -dimensional volume of the billiard, Γ is the gamma function, and J_n is the n -th order Bessel function of the first kind.

We compare our numerical calculations of eigenfunctions in different shape billiards and Berry's theory in Appendices C and D.

1.5 Outline of Dissertation

This dissertation is organized as follows: In Chapter 2², we study the statistics of the energy level splittings between symmetric and antisymmetric pairs of mirror symmetric wells coupled by a rectangular tunneling barrier. We use the random plane wave hypothesis to develop a theory for the chaotic cases. We also show that the mean splittings of differently shaped wells, including both integrable and chaotic wells, are the same if their well areas and barrier parameters are the same, but that the statistics of fluctuation are very different for chaotic and integrable wells.

In Chapter 3³, we study the statistics of the input/output properties of waves in mixed cavities in which ray trajectories that are regular and chaotic coexist. In particular, we focus on the statistical properties of the impedance matrix (related to the scattering matrix) which can be written as a sum over eigenmodes where the eigenmodes can typically be classified as either regular or chaotic. We obtain statistical predictions for the impedance by separating the regular and chaotic contribu-

²Chapter 2 is a republication of work published in Physical Review E, as approved by the thesis committee [45].

³Chapter 3 is a republication of work published in Physical Review E, as approved by the thesis committee [46].

tions. Finally, we test these predictions by comparison with numerical calculations for a specific mushroom cavity shape and obtain good agreement.

Chapter 2

Theory of Chaos Regularization of Tunneling in Chaotic Quantum Dots

2.1 Introduction

The work presented in this chapter is a continuation of previous work in Ref. [47] in which we reported numerical results and abbreviated heuristic arguments justifying our numerical observations. Our aim now is to provide a fuller theoretical analysis of the results in Ref. [47].

Reference [47] considers symmetric double well situations of the type shown in Figs. 2.1 (a) and (b). There is a barrier region of uniform potential V_B , width 2Δ , and length L . This barrier region separates two mirror-symmetric wells in which the potential is zero and whose (non-barrier) boundaries are hard walls. If the energy E is less than V_B , then a point particle is classically confined to one of the wells, and its orbit follows straight lines between specular reflections from the well boundaries (a billiard system). The character of the orbit depends on the shape of the well. For the rectangular well of Fig. 2.1 (a) the orbits of a point particle are integrable, with separately constant horizontal and vertical kinetic energies. For the shape of the well in Fig. 2.1 (b), the convex walls insure that all typical orbits are chaotic and ergodically fill the full available phase space [47]. In particular, if a typical

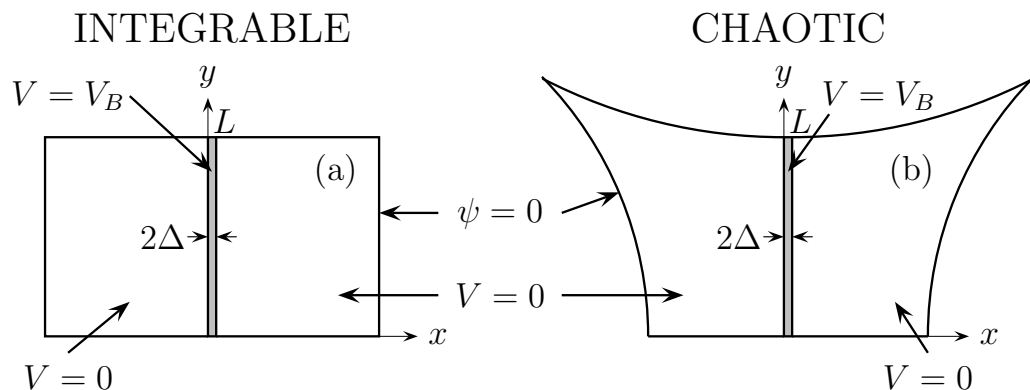


Figure 2.1: Symmetrical double wells of area A separated by a tunneling potential barrier of width 2Δ , length L and height V_B . (a) shows the case of rectangular wells, while (b) shows a case in which all typical orbits are chaotic.

particle orbit in the Fig. 2.1 (b) billiard is sampled at some random time t , then the location of the particle has a uniform probability density per unit area in the well, and the probability density of the direction of particle motion is uniformly isotropic in $[0, 2\pi)$. (Reference [47] also treats other completely regular or chaotic well shapes^{1.})

Considering symmetric wells, as in Fig. 2.1, the quantum eigenstates have either even or odd parity with respect to the center line, and for E sufficiently below the barrier height V_B , we may consider the states to come in symmetric/antisymmetric pairs with nearly equal energies. We denote the σ th such pair (E_σ^S, E_σ^A) . The symmetric state energy is always less than the antisymmetric state energy,

¹These include the stadium billiard, which, although chaotic, due to its continuous family of neutrally stable, 'bouncing-ball' periodic orbits, exhibits scar-type modes with tunneling rates that can substantially deviate from the mean. Note that, due to its convex walls, such orbits are absent in the strongly chaotic case of Fig. 2.1(b)

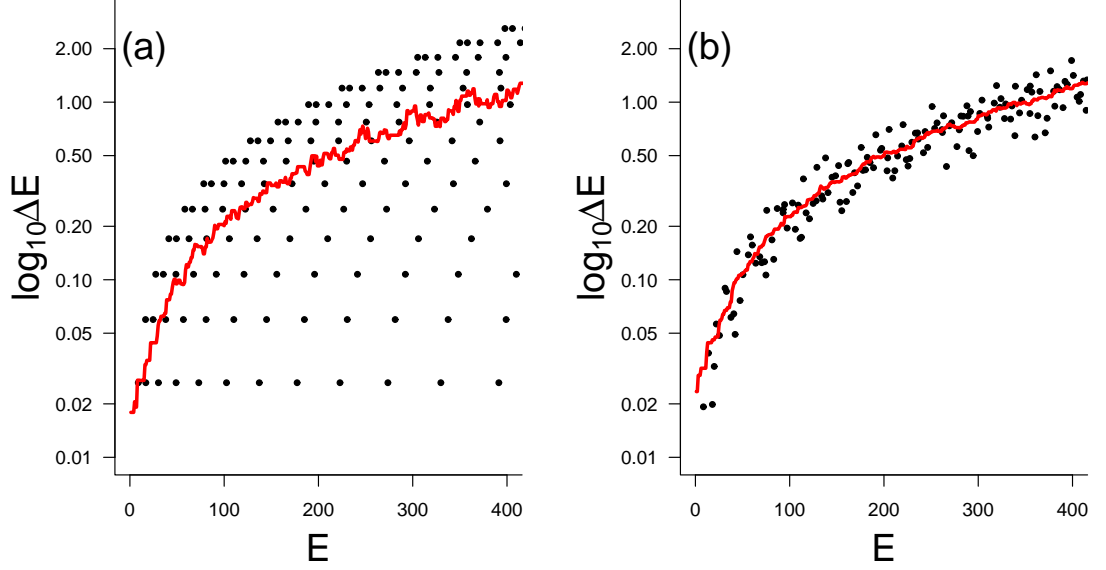


Figure 2.2: Energy level splittings versus energy plotted as black dots, along with the sliding average (red), $\langle \Delta E \rangle_{E,\epsilon}$. The parameters used in there plots are $V_B = 1000$, $\Delta_B = 0.05$, $L = 2.423$, $A = 4.8$.

$E_\sigma^S < E_\sigma^A$. The energy level splitting is denoted

$$\Delta E_\sigma = E_\sigma^A - E_\sigma^S. \quad (2.1)$$

Figure 2.2 shows as black dots values of ΔE_σ versus $E_\sigma = \frac{1}{2}(E_\sigma^A + E_\sigma^S)$ from numerical solutions of the normalized Schrödinger equation,

$$[\nabla^2 + E - V(x, y)]\psi(x, y) = 0, \quad (2.2)$$

with $\psi = 0$ on the hard walls, $V = V_B$ in the barrier region ($0 < x < 2\Delta$) and $V = 0$ in the wells. The parameters V_B , Δ and L and the well area A , are all taken to be the same for the two cases, Fig. 2.1 (a) and Fig. 2.1 (b). Also $EA \gg 1$, i.e., the

well dimensions are large compared to the quantum wavelength, corresponding to the semiclassical regime. Shown in Fig. 2.2 (a) and (b), in red, is a sliding average $\langle \Delta E \rangle_{E,\epsilon}$ of ΔE_σ using a window, $(E - \epsilon)$ to $(E + \epsilon)$, that encompasses 2 to 15 splitting values. Figure 2.3 shows the two sliding averages plotted together on the same graph, in blue for the integrable case (Fig. 2.1 (a)) and in black for the chaotic case (Fig. 2.1 (b)), along with our theoretical result (red) to be derived in Sec. 2.5. The two main conclusions from the numerical results of Ref. [47] are the following:

(1) Fluctuations of the quantum splittings are *very much* larger (note the logarithmic vertical scale) in the integrable well case as compared to the chaotic well case.

(2) For the same gross parameters (A, V_B, Δ, L) , the sliding average $\langle \Delta E \rangle_{E,\epsilon}$ versus E is independent of the well shape.

In Ref. [47] it was found that (1) and (2) hold for all pairs of similarly related chaotic and regular well shapes studied ¹.

The rest of this chapter is organized as follows. Noting that the numerical results in Fig. 2.2 all satisfy

$$\Delta E_\sigma \ll \frac{1}{2} (E_{\sigma+1} - E_{\sigma-1}), \quad (2.3)$$

in Sec. 2.2 we use perturbation theory to develop a formal expression for ΔE_σ . This expression is essentially Herring's formula [48]. Herring's formula was also used in Wilkinson's treatment of tunneling between regular regions adapted to our problem [33]. Section 2.3 then applies Berry's random plane wave hypothesis [44] to obtain the statistics of the splittings $\{\Delta E_\sigma\}$ in the case of chaotic classical dy-

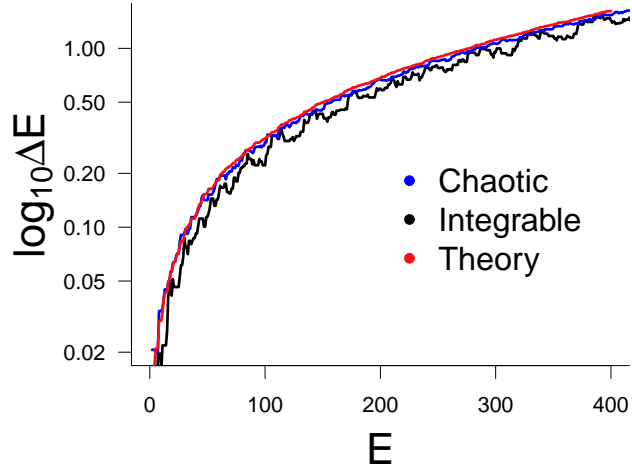


Figure 2.3: Sliding average versus E .

namics. In Sec. 2.4, as an example, we numerically test the result of Sec. 2.3 by comparing its predictions with the data shown in Fig. 2.2 (b). Section 2.5 applies a Green's function technique based on the method of Balian and Bloch for deriving the semiclassical perimeter correlation to the density of state for billiard systems [49, 50, 51, 52] to obtain the sliding average splitting $\langle \Delta E \rangle_{E,\epsilon}$ and show that it is independent of well shape. Section 2.6 concludes with further discussion. As discussed in Sec. 2.6, we report in Sec. 2.6.2 the extension of our method to the treatment of tunneling out of a single chaotic well into an open region with outgoing quantum waves.

2.2 Perturbation Theory for the Statistics of Energy Level Splitting for Chaotic Wells

2.2.1 Setup

We consider the symmetric and antisymmetric wave functions, denoted ψ_S and ψ_A , along with their corresponding energy levels, $E_S \equiv k_S^2$ and $E_A \equiv k_A^2$ (where we choose units in which $\hbar^2/(2m) \equiv 1$). Referring to Fig.2.1, we take the potential to be zero in the left and right wells and to be $V = V_B \equiv k_B^2$ in the barrier region, $0 < x < 2\Delta$. Focusing on the left well, we have that

$$(\nabla^2 + k_{S,A}^2)\psi_{S,A}^2 = 0 \quad \text{for } x < 0, \quad (2.4)$$

$$\left[\frac{\partial}{\partial x} \psi_{S,A}(x, y) \right]_{x=0^-} + \hat{H}_{S,A}[\psi_{S,A}(0^-, y)] = 0, \quad (2.5)$$

and

$$\psi_{S,A}(x, y) = 0 \quad (2.6)$$

on the boundary of the left well other than that at $x = 0$. \hat{H}_S and \hat{H}_A denote operators on functions of y that we now obtain.

2.2.2 Boundary Condition at $x = 0^-$

Within the barrier region, $0 < x < 2\Delta$, ψ_A and ψ_S satisfy the following conditions,

$$\frac{\partial \psi_S}{\partial x} = 0 \quad \text{and} \quad \psi_A = 0 \quad \text{at} \quad x = \Delta. \quad (2.7)$$

Thus, in the barrier, solutions of the time-independent Schrodinger equation,

$$[\nabla^2 - (k_B^2 - k_{S,A}^2)]\psi_{S,A} = 0, \quad \psi_{S,A} = 0 \quad \text{at} \quad y = 0, L, \quad (2.8)$$

can be written as

$$\psi_S(x, y) = \sum_{m=1}^{\infty} S_m \frac{\cosh[\alpha_m(\Delta - x)]}{\cosh(\alpha_m \Delta)} \sin\left(\frac{m\pi y}{L}\right), \quad (2.9)$$

$$\psi_A(x, y) = \sum_{m=1}^{\infty} A_m \frac{\sinh[\alpha_m(\Delta - x)]}{\sinh(\alpha_m \Delta)} \sin\left(\frac{m\pi y}{L}\right), \quad (2.10)$$

$$\alpha_m = \sqrt{k_B^2 + \left(\frac{m\pi}{L}\right)^2 - k^2}. \quad (2.11)$$

Noting that both $\psi_{A,S}$ and $\partial\psi_{A,S}/\partial x$ are continuous at $x = 0$, we have that

\hat{H}_S and \hat{H}_A in (2.5) are given by

$$\begin{aligned} \hat{H}_S[f(y)] &\equiv \sum_{m=1}^{\infty} \hat{H}_S^{(m)} f_m \sin\left(\frac{m\pi y}{L}\right), \\ \hat{H}_S^{(m)} &= \alpha_m \tanh(\alpha_m \Delta), \end{aligned} \quad (2.12)$$

$$\begin{aligned} \hat{H}_A[f(y)] &\equiv \sum_{m=1}^{\infty} \hat{H}_A^{(m)} f_m \sin\left(\frac{m\pi y}{L}\right), \\ \hat{H}_A^{(m)} &= \alpha_m \coth(\alpha_m \Delta). \end{aligned} \quad (2.13)$$

where f_m denote coefficients of the Fourier sine series of $f(y)$,

$$f(y) = \sum_{m=1}^{\infty} f_m \sin\left(\frac{m\pi y}{L}\right). \quad (2.14)$$

Note also that the $\hat{H}_{S,A}$ operators are self adjoint,

$$\int_0^L g(y) \hat{H}_{S,A}[f(y)] dy = \int_0^L f(y) \hat{H}_{S,A}[g(y)] dy. \quad (2.15)$$

2.2.3 Perturbation expansion

As the thickness of the barrier Δ becomes large, we see from (2.12) and (2.13) that \hat{H}_S and \hat{H}_A become the same:

$$\hat{H}_S^{(m)}, \hat{H}_A^{(m)} \rightarrow \alpha_m.$$

We denote this limit by the subscript 0 and define a corresponding wavefunction and energy level, ψ_0 and k_0^2 , that satisfy the problem,

$$(\nabla^2 + k_0^2)\psi_0 = 0 \quad \text{for } x < 0, \quad (2.16)$$

$$\left[\frac{\partial}{\partial x} \psi_0(x, y) \right]_{x=0^-} + \hat{H}_0 [\psi_0(0^-, y)] = 0, \quad (2.17)$$

and $\psi_0 = 0$ on the boundaries of the left well other than that at $x = 0$. The operator \hat{H}_0 is defined as in Eqs. (2.12) and (2.13) with

$$\hat{H}_0^{(m)} = \alpha_m. \quad (2.18)$$

Since \hat{H}_S and \hat{H}_A become equal as $\Delta \rightarrow \infty$, the symmetric and antisymmetric energy eigenfunctions (ψ_S and ψ_A) and energy levels (k_S^2 and k_A^2) also become equal. (In particular, they become ψ_0 and k_0^2 .) Thus, for sufficiently large Δ , we can assume that these symmetric and antisymmetric quantities are close to each other and are close to the solution of Eqs. (2.16)- (2.18). More formally, if we introduce a small expansion parameter ϵ , we have

$$\begin{aligned} \psi_{S,A} - \psi_0 &= O(\epsilon) \\ k_{S,A}^2 - k_0^2 &= O(\epsilon) \\ \hat{H}_{S,A} - \hat{H}_0 &= O(\epsilon). \end{aligned} \quad (2.19)$$

Multiplying Eq. (2.4) by $\psi_0(x, y)dxdy$ and Eq. (2.16) by $\psi_{S,A}(x, y)dxdy$, integrating over the area of the left well, and subtracting the results, we obtain

$$\int_{LW} [\psi_0 \nabla^2 \psi_{S,A} - \psi_{S,A} \nabla^2 \psi_0] dxdy = (k_{S,A}^2 - k_0^2) \int_{LW} \psi_0 \psi_{S,A} dxdy, \quad (2.20)$$

where LW denotes the area of the left well. Applying Green's identity to the left side of this equation, we have essentially Herring's formula [48],

$$\int_0^L \{\psi_0 \hat{H}_{S,A}[\psi_{S,A}] - \psi_{S,A} \hat{H}_0[\psi_0]\}_{x=0} dy = (k_{S,A}^2 - k_0^2) \int_{LW} \psi_0 \psi_{S,A} dxdy, \quad (2.21)$$

where we have used the condition that $\psi_{S,A,0} = 0$ on the boundaries of the left well other than that at $x = 0$. Furthermore, from (2.15) the left side of (2.21) can be rewritten

$$\int_0^L \{\psi_0 \Delta \hat{H}_{S,A}[\psi_{S,A}]\}_{x=0} dy = (k_{S,A}^2 - k_0^2) \int_{LW} \psi_0 \psi_{S,A} dxdy, \quad (2.22)$$

where $\Delta \hat{H}_{S,A}[f(y)] \equiv \hat{H}_{S,A}[f(y)] - \hat{H}_0[f(y)]$. Noting from (2.19) that $\Delta \hat{H}_{S,A}$ and $(k_{S,A}^2 - k_0^2)$ are both $O(\epsilon)$, we see that, to lowest order in ϵ , we can set $\psi_{S,A} = \psi_0$ in (2.22), thus yielding the perturbation theory result,

$$k_{S,A}^2 - k_0^2 = \frac{\int_0^L \{\psi_0 \Delta \hat{H}_{S,A}[\psi_0]\}_{x=0} dy}{\int_{LW} \psi_0^2 dxdy}. \quad (2.23)$$

It follows from (2.12), (2.13) and (2.18) that $\hat{H}_A^{(m)} > \hat{H}_0^{(m)} > \hat{H}_S^{(m)}$. Thus, we have that $k_A^2 > k_0^2 > k_S^2$. We denote the energy level splitting by $\Delta E = \Delta k^2 \equiv k_A^2 - k_S^2$. Taking the difference between the symmetric and antisymmetric versions of (2.23) and employing our definitions of $\hat{H}_{S,A,0}$, we obtain

$$\Delta E = \sum_{m=1}^{\infty} \frac{L \alpha_m C_m^2}{\sinh(2\alpha_m \Delta)} / \int_{LW} \psi_0^2 dxdy, \quad (2.24)$$

where C_m are the Fourier sine coefficients of $\psi_0(0, y)$,

$$\psi_0(0, y) = \sum_{m=1}^{\infty} C_m \sin\left(\frac{m\pi y}{L}\right). \quad (2.25)$$

2.3 Evaluation of ΔE for Chaotic Eigenfunctions

In the region $x < 0$, but near $x = 0$, the upper well boundary in Fig. 2.1 is close to $y = L$. Therefore, in this region we can take

$$\psi_0(x, y) \cong \sum_{m=1}^{\infty} c_m \sin\left(\frac{m\pi y}{L}\right) \sin(k_{x,m}x - \phi_m), \quad (2.26)$$

where $k_{x,m}^2 = k_0^2 - (m\pi/L)^2$, and ϕ_m is determined by the boundary condition $\partial\psi_0/\partial x = -\hat{H}_0[\psi_0]$ at $x = 0$, which yields

$$\tan \phi_m = \frac{k_{x,m}}{\alpha_m}. \quad (2.27)$$

Comparing (2.26) and (2.25), we see that

$$C_m = -c_m \sin \phi_m, \quad (2.28)$$

and from (2.11) and (2.27)

$$\sin \phi_m = \frac{k_{x,m}}{k_B}. \quad (2.29)$$

We will view Eq. (2.26) as is a statistical model and think of the values of the c_m as pseudo-random variables that, for any given two realizations, can be regarded as representing two different eigenfunctions with nearly the same energy k_0^2 . In what follows we will approximate (2.26) by cutting off the sum at $m = M$, where M is the maximum value of m for which $k_{x,m}^2 > 0$,

$$M = \max \left[m \mid k_0 \geq \left(\frac{m\pi}{L} \right) \right]. \quad (2.30)$$

That is, we only include propagating modes.

We now need a model for characterizing the pseudo-random coefficients c_m in (2.26). To do this, we assume $M \gg 1$, follow Berry [44], and utilize the chaotic classical dynamics of particles in the potential wells, together with the correspondence principle. Our chaotic classical particle trajectories have the following ergodic character: For typical initial conditions and any small localized region δR in the well, a very long orbit will pass through δR many times, and, if one examines these passages, one will find that, as the orbit length approaches infinity, (i) the fraction of time spent by the orbit in the region δR is the ratio of the area of δR to the total area of the well, and (ii) the orientation of the particle's velocity, in its passes through δR , is uniformly distributed in angle. Thus, if we imagine sampling the chaotic orbit at some randomly chosen time, its location will have a uniform probability density distribution in space and its velocity (whose magnitude is fixed by the particle energy) will have an isotropic probability distribution in its orientation. Thinking of ψ_0^2 as analogous to the classical probability density in space and invoking property (i), the correspondence principle suggests that, for wavelengths small compared to the cavity size, the coarse grained average of ψ_0^2 over several wavelengths will have a value that is the same near $x = 0$ as in any other region of the well.

We now ask how the coefficients c_m in (2.26) are related to the integral $\int_{LW} \psi_0^2 dx dy$ appearing in the denominator of Eq. (2.24). We see from (2.26) that the integral of ψ_0^2 over a region of area A_B abutting the barrier and extending not too far away from it is $(A_B/4) \sum c_m^2$, where the factor $1/4$ results from taking the spatial average of $\sin^2(m\pi y/L) \sin^2(k_{x,m}x - \phi_m)$ over several wavelengths. If the

wavelength is short, $k_0L \gg 1$, based on point (i) above and the correspondence principle, one might suppose that this result for $\int_{AB} \psi_0^2 dx dy$ can be extended to x values far from the barrier. In particular, we expect that the spatial average of ψ_0^2 near $x = 0$ is approximately the same as in any other region of the well. Thus, we obtain the estimate,

$$\int_{LW} \psi_0^2 dx dy \cong \frac{A}{4} \sum_m c_m^2, \quad (2.31)$$

where (as previously stated) A is the entire area of the left or right well. We expect (2.31) to hold as long as the barrier dimension L is much greater than a wavelength $M\pi \approx k_0L \gg 1$. When the barrier dimension becomes comparable to or smaller than a wavelength, point to point variations in the magnitude of the wavefunction lead to departures between the average value of ψ_0^2 in the well and the corresponding value near the barrier. However, even if k_0L is large, Eq. (2.31) is only approximate, and we expect it to hold with an error that becomes small as $k_0L \rightarrow \infty$. We will find that, when computing fluctuations in energy splittings, the small fluctuating error in (2.31) can be important (e.g., see Sec. 2.6.1 and Sec. 2.4). Use of (2.31) as a strict equality assumes that the coarse grained average of ψ_0^2 is essentially determined throughout the total area, A , by the M amplitudes, C_m of the propagating modes ($k_{x,m}^2 > 0$) near the barrier. This is not always the case. For example, if scars are present, there may be deviation between the average of ψ_0^2 near the barrier and throughout the well. We note that the intensity and frequency of the scarring contribution decreases with increasing k_0L as shown in Refs. [53] and [54]. Thus, in the limit $k_0L \rightarrow \infty$, Eq. (2.31) applies; but the error in (2.31) depends on

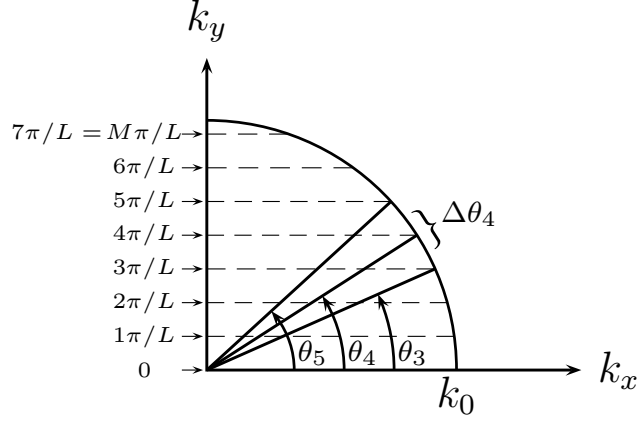


Figure 2.4: Propagation directions.

the shape of the well. For the time being we will proceed on the assumption that the estimate given by Eq. (2.31) can be used for the denominator of (2.24). Although we will find that (2.31) works well for the chaotic shape shown in Fig. 2.1(b), we will also argue that, in other cases, (2.31) may not provide as good a model for fluctuations of ΔE .

To invoke property (ii) (i.e., isotropy of velocity direction), we note that the terms in the sum in (2.26) represent wave propagation directions that make an angle,

$$\theta_m = \arcsin\left(\frac{m\pi}{k_0 L}\right), \quad (2.32)$$

with respect to the x axis; see Fig. 2.4.

We imagine that these wave-quantized angles represent a range of the continuous classical angles, where the range for θ_m is

$$\Delta\theta_m = \frac{1}{2}(\theta_{m+1} - \theta_{m-1}), \quad (2.33)$$

and, for $m = M$, we replace θ_{m+1} by $\pi/2$, while, for $m = 1$, we use $\theta_{m-1} = 0$.

Invoking the classical orientation isotropy of particle velocities, point (ii) above,

the correspondence principle suggests that $\langle c_m^2 \rangle$ is proportional to $\Delta\theta_m$, $\langle c_m^2 \rangle = (\text{constant})\Delta\theta_m$, where the angle brackets denote an average over our pseudorandom fluctuations. Using this in (2.31), we obtain

$$\langle c_m^2 \rangle = 4\langle \psi_0^2 \rangle (\Delta\theta_m / \sum_{m'=1}^M \Delta\theta_{m'}). \quad (2.34)$$

(Note that the sum over $\Delta\theta_{m'}$ is $(\pi/2) - (\theta_1/2)$, rather than $\pi/2$. We have chosen to omit the angles $0 \leq \theta \leq \theta_1/2$ because the normally incident wave corresponding to $m = 0$ is ruled out by our boundary condition, $\psi_0 = 0$ at $y = 0, L$ and $x = 0$. In any case, this choice makes only a small difference for $M \gg 1$.) Since we view the c_m as resulting from the sum of many roughly independent classical ray contributions, the central limit theorem implies that c_m will be a Gaussian random variable. Thus we set

$$c_m = \langle c_m^2 \rangle^{1/2} \xi_m, \quad (2.35)$$

where ξ_m are independent, Gaussian, zero mean, unit variance random variables,

$$\langle \xi_m \xi_{m'} \rangle = \delta_{m,m'}, \quad (2.36)$$

with $\delta_{m,m'} = 1$ if $m = m'$ and $\delta_{m,m'} = 0$ if $m \neq m'$.

Combining (2.31), (3.12), (2.34), (2.29), (2.28) and (2.24), we arrive at our main result,

$$\Delta E = \frac{\sum_{m=1}^M \mu_m \delta E_m \xi_m^2}{\sum_{m=1}^M \mu_m \xi_m^2}, \quad (2.37)$$

where

$$\delta E_m = \frac{4Lk_{x,m}^2 \alpha_m}{Ak_B^2 \sinh(2\alpha_m \Delta)} \quad (2.38)$$

is the contribution to the splitting due to the m -th mode of the barrier,

$$\mu_m = \frac{2\Delta\theta_m}{\pi - \theta_1} \quad (2.39)$$

is the weight assigned to the angle θ_m in the well, and the Gaussian random variables ξ_m satisfy (2.36).

When M is large (i.e., $kL \gg 1$) the number of terms in the sums in (2.37) is large and the denominator is close to unity with relatively small fluctuations. Although the fluctuations of the denominator from unity are small for large M , it can be necessary to include them, as they significantly contribute to the evaluation of the fluctuations of ΔE from $\langle \Delta E \rangle$, which are also small for large M . As before, the angle brackets, $\langle \dots \rangle$, represent an ensemble average over realizations of the random set $\{\xi_m\}$. The sliding average $\langle \dots \rangle_{E,\epsilon}$ in Sec. 3.1 is hypothesized to approximate $\langle \dots \rangle$, if $\langle \dots \rangle$ is approximately constant over the window width ϵ and if many energy levels are contained in the window.

Equation (2.37) is a statistical model for the pseudorandom splittings ΔE . This model can be used to generate ensembles of values of ΔE via the Monte Carlo procedure of generating and inserting random values for the Gaussian quantities ξ_m , from which the statistical properties of ΔE can be numerically determined, as will be illustrated by the example given in Sec. 2.4.

For large $M \approx kL/\pi$, both the numerator and the denominator in Eq. (2.37) will have relative fluctuations from their mean values that are small. Recall that the mean of the denominator is, by construction, one. Thus we expect that replacing the denominator by one (i.e., neglecting denominator fluctuations) will make little

difference in the mean value of ΔE obtained from Eq. (2.37). Fluctuations of the denominator, however, can have a significant effect when looking at fluctuations of ΔE from its mean, as we now discuss. Say the numerator has a large upward (or downward) fluctuation. This might occur because ξ_m^2 for some m values happen to be significantly above (or below) their mean value of one. If this is so, then the denominator will also have a large upward (or downward) fluctuation, and this will mitigate the effect of the numerator fluctuation on ΔE . Thus correlation of the fluctuations of the numerator and the denominator reduce the overall fluctuations of ΔE .

We now use Eq. (2.37) to obtain an expression for the mean value of ΔE in the limit of vary large $M \approx kL/\pi$. (In Sec. 2.6.1 we do an analogous calculation of the variance of ΔE .) Using (2.37) the expected value of ΔE is

$$\langle \Delta E \rangle = \sum_{m=1}^M \mu_m \delta E(\theta_m), \quad (2.40)$$

where $\delta E(\theta_m) \equiv \delta E_m$, $\delta E(\theta) = (4L)(A\Delta)^{-1}F(\theta)$, and

$$F(\theta) = \cos^2 \theta \frac{k_0^2}{k_B^2} \frac{(k_B \Delta \sqrt{1 - (k_0/k_B)^2 \cos^2 \theta})}{\sinh[2k_B \Delta \sqrt{1 - (k_0/k_B)^2 \cos^2 \theta}]}, \quad (2.41)$$

where we have used $\alpha_m = k_B \sqrt{1 - (k_0/k_B)^2 \cos^2 \theta}$ and $k_m = k_0 \cos \theta$. In obtaining (2.40), we have noted that the denominator of (2.37) can be written as

$$\sum_{m=1}^M \mu_m \xi_m^2 = 1 + \sum_{m=1}^M \mu_m (\xi_m^2 - 1), \quad (2.42)$$

where the second term is a fluctuation ($\langle \xi_m^2 - 1 \rangle = 0$) which means that each individual eigenstate in the ensemble is not normalized [55]². For $M \gg 1$, this

²A potential avenue for future elucidation of such fluctuations might be to employ Bogomolny's

fluctuating component is small compared to unity, and we neglect it. (We emphasize, however, that inclusion of this fluctuation can be crucial for a calculation of the variance of ΔE .) In the semiclassical limit $kL \gg 1$, $M \gg 1$, and $\Delta\theta_m$ becomes small, allowing us to approximate the summation over m in (2.40) by an integral. Thus (2.40) becomes

$$\langle \Delta E \rangle = \frac{4L}{A\Delta} I(E/V_B, k_B\Delta), \quad (2.43)$$

$$I(E/V_B, k_B\Delta) = \frac{2}{\pi} \int_0^{\pi/2} F(\theta) d\theta, \quad (2.44)$$

and we recall $E/V_B = k_0^2/k_B^2$.

Equation (2.40) is plotted as the red curve in Fig. 2.3. We next illustrate the use of (2.37) by application to the fluctuation data shown in Fig. 2.2 (b).

2.4 Monte Carlo Evaluation of Energy Splittings

In order to quantitatively compare our theory with the numerical data for energy level splittings in Fig 2.2, we define the sliding average splitting and the sliding average splitting variance as

$$\langle \Delta E \rangle_{E_0, \epsilon} = \frac{1}{N_{E_0, \epsilon}} \sum_{\sigma}^{|E_\sigma - E_0| < \epsilon} \Delta E_\sigma, \quad (2.45)$$

$$\sigma_{\Delta E, E_0, \epsilon}^2 = \frac{1}{N_{E_0, \epsilon}} \sum_{\sigma}^{|E_\sigma - E_0| < \epsilon} (\Delta E_\sigma - \langle \Delta E \rangle_{E_0, \epsilon})^2, \quad (2.46)$$

where $N_{E_0, \epsilon}$ is the number of states such that $|E_0 - E_\sigma| < \epsilon$ and we choose $\epsilon = \sqrt{E_0}$.

This quantity is plotted as a solid line in Figs. 2.2, 2.3 and 2.5. To compare with our semiclassical Green function approach; an example where this approach has been employed in another context is the paper by Ullmo et al. [56]

result, Eq. (2.37), we use Monte Carlo simulations. At each energy level E_σ plotted in Fig. 2.2, we use (2.37) to generate 10000 splitting values, ΔE_{σ_i} , $i = 1, 2, \dots, 10000$. Similar to Eq. (2.45) and (2.46), for each of the 10000 set of Monte Carlo data, $\{\Delta E_{\sigma_i}\}$, we also calculate sliding average splittings,

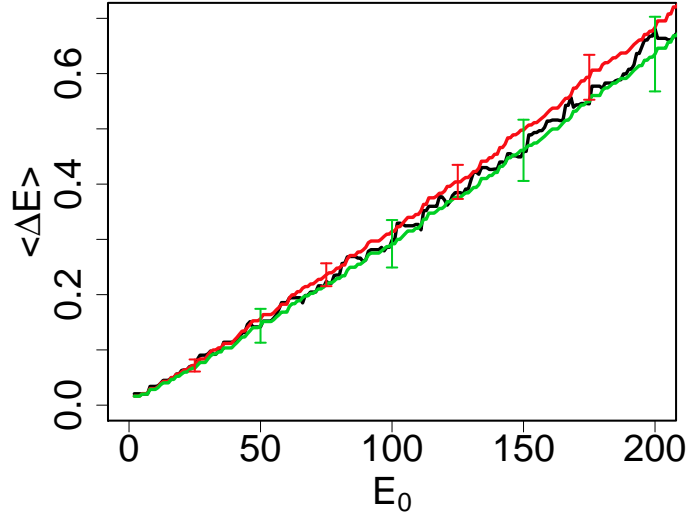
$$\langle \Delta E \rangle_{E_0, \epsilon, i} = \frac{1}{N_{E_0, \epsilon}} \sum_{\sigma_i}^{|E_{\sigma_i} - E_0| < \epsilon} \Delta E_{\sigma_i}, \quad (2.47)$$

and sliding average splitting variances,

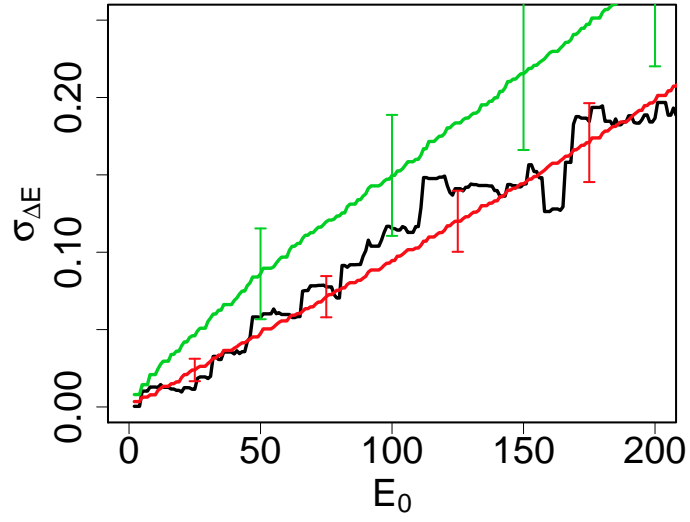
$$\sigma_{\Delta E, E_0, \epsilon, i}^2 = \frac{1}{N_{E_0, \epsilon}} \sum_{\sigma_i}^{|E_{\sigma_i} - E_0| < \epsilon} (\Delta E_{\sigma_i} - \langle \Delta E \rangle_{E_0, \epsilon, i})^2. \quad (2.48)$$

At each E_0 , we can calculate the ensemble average and variance of the sliding average splitting and the sliding average splitting variance. In Fig. 2.5, we compare these Monte Carlo results (plotted in red) with results from numerical solutions of the Schrödinger wave equation (plotted in black); we also compare these results to what (2.37) would predict if the denominator of Eq. (2.37) were set to unity (plotted in green). Figure 2.5(a) shows that no matter whether fluctuations in the denominator are included or neglected, the sliding averages of the splittings for both calculations fall within one ensemble standard deviation of each other, and both agree well with results from numerical solution of the wave equation. In contrast, we see from Fig. 2.5(b) that including the fluctuations in the denominator reduces the splitting variance. That is, correlations between the denominator and numerator reduces the estimated eigenfunction to eigenfunction variations in the splitting energy.

To examine the effect of the correlation between the denominator in Eq. (2.37) and the numerator, we numerically calculate energy splittings for symmetrical dou-



(a)



(b)

Figure 2.5: Comparison of (a) sliding average splittings, $\langle \Delta E \rangle$, and (b) sliding average splitting variances, $\sigma_{\Delta E}$, versus E_0 for numerical data (black), Eq. (2.37) (red) and Eq. (2.37) with its denominator replaced by one (green).

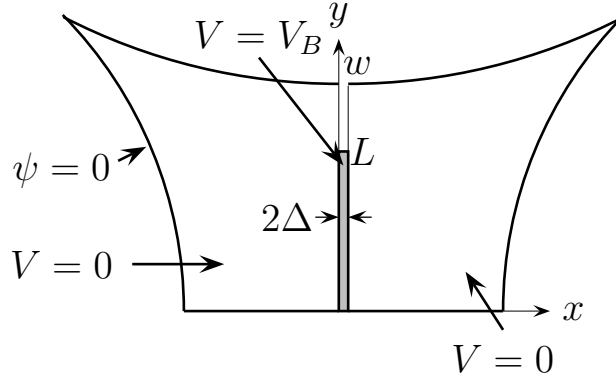
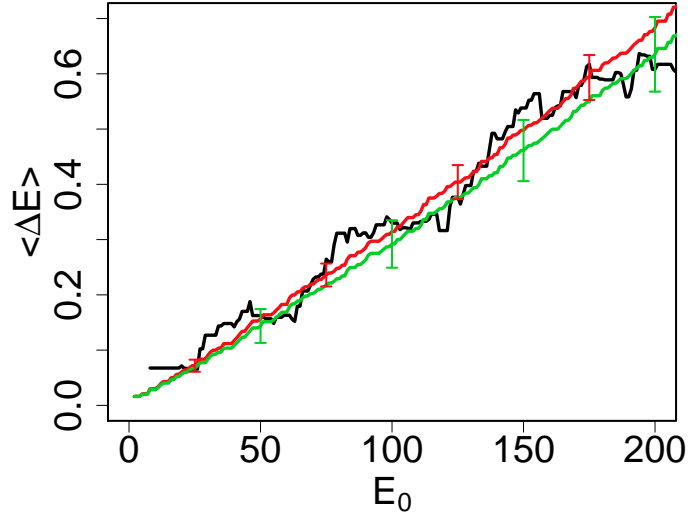
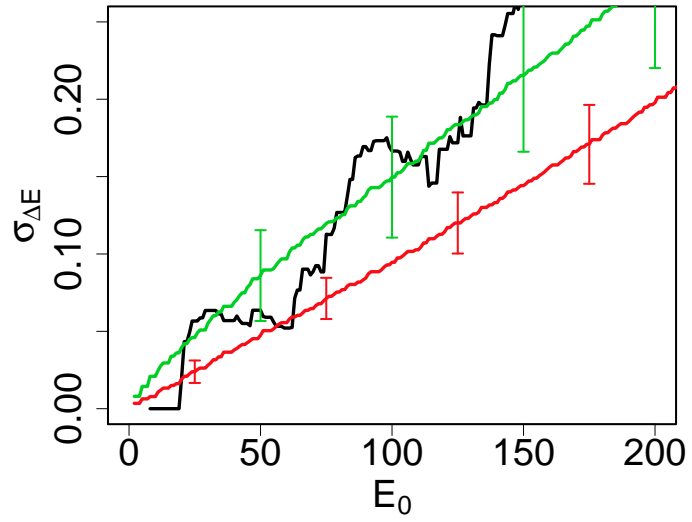


Figure 2.6: Symmetrical double wells of area A separated by a non perfectly coupled tunneling potential barrier of width 2Δ , barrier length L , height V_B and wall length w .

ble well that has the same gross parameters (A, V_B, Δ, L) with Fig. 2.1 but longer wall at $x = 0$, see Fig. 2.6, and make analogous figures to Fig. 2.5 as Fig. 2.7. In order to explain the discrepancy in Fig. 2.7(b) between the theory as expressed by Eq. (2.37) and our data from numerical solution of the Schrödinger equation, we now re-examine our assumption that we can use the approximation (2.31) for $\int_{LW} \psi_0^2 dx dy$ in (2.37). In particular, as explained in the discussion following Eq. (2.31), at finite wavelength, $A^{-1} \int_{LW} \psi_0^2 dx dy$ and $A_B^{-1} \int_{A_B} \psi_0^2 dx dy$ may not be perfectly correlated. As an alternate hypothesis, let us now suppose that fluctuations of $A_B^{-1} \int_{A_B} \psi_0^2 dx dy$ are uncorrelated with those of $A^{-1} \int_{LW} \psi_0^2 dx dy$. If this is the case, the fluctuations of the denominator in Eq. (2.24) are uncorrelated with fluctuations of the numerator. In this situation we can choose to constrain the denominator to be normalized to one, $\int_{LW} \psi_0^2 dx dy = 1$. In particular, this is consistent with our previous definition $\langle \xi_m^2 \rangle = 1$ and conforms with the idea that $\int_{A_B} \psi_0^2 dx dy$ averaged over many modes



(a)



(b)

Figure 2.7: (a) Analogous to Fig. 2.5(a) but for Fig 2.6. (b) Analogous to Fig. 2.5(b) but for Fig 2.6.

should respect the global normalization $\int_{LW} \psi_0^2 dx dy = 1$ for each mode. Thus this alternate hypothesis yields (2.37), but with the denominator replaced by one,

$$\Delta E = \sum_{m=1}^M \mu_m \delta E_m \xi_m^2. \quad (2.49)$$

In Sec. 2.6.3, we provide analytical support for this and show how a transition from applicability of (2.37) to applicability of (2.49) can take place as a geometrical parameter is varied. Equations (2.37) and (2.49) result from two opposite bases, perfect correlation for (2.37) and zero correlation for (2.49). As previously discussed in the text following Eq. (2.37), correlation reduces the fluctuations. Hence, we expect the fluctuation level to lie between the predictions from these two extremes, and we regard the green and red variance curves in Figs. 2.5(b) and 2.7(b) as predicted upper and lower bounds for the fluctuation level. Our data for the two chaotic shapes, indeed conform to this expectation, with the fluctuation level for the shape in Fig. 2.1(b) being close to the lower bound, while that for the shape in Fig. 2.6 is closer to the upper bound.

2.5 Green's Function Analysis of Sliding Average of Splittings

We have obtained an expression, Eq. (2.40) for the average of the splittings, $\langle \Delta E \rangle$, for chaotic cavities. We have also seen (Fig. 2.3) that this result agrees numerically with our results for an integrable cavity of rectangular shape. Here we demonstrate in a formal analysis that our result for $\langle \Delta E \rangle$ applies for all cavity shapes independent of whether they are integrable, chaotic, or a mixture of chaotic and integrable in different regions of phase space. Our analysis makes use of previous

work on perimeter corrections to Weyl's equation for the density of states [49].

We begin with the Green's function of the unperturbed left well ($\Delta \rightarrow \infty$ in Fig.2.1) expanded in orthonormal modes ψ_0^σ of the left well,

$$G_E(\vec{x}, \vec{x}') = \sum_{\sigma} \frac{\psi_0^\sigma(\vec{x})\psi_0^\sigma(\vec{x}')}{E - E_\sigma}, \quad E_\sigma = (k_\sigma)^2, \quad (2.50)$$

where $(\nabla^2 + E)G_E = \delta(\vec{x} - \vec{x}')$, $(\nabla^2 + E_\sigma)\psi_0^\sigma = 0$ with the appropriate boundary conditions, and $\vec{x} = (x, y)$. According to our perturbation theory (Eq. (2.23)) the splitting for unperturbed mode σ is

$$\Delta E_\sigma = \int_0^L \{\psi_0^\sigma(x, y)\Delta\hat{H}[\psi_0^\sigma(x, y)]\}_{x=0^-} dy, \quad (2.51)$$

where the operator $\Delta\hat{H} = \Delta\hat{H}_A - \Delta\hat{H}_S$. Operating on (2.50) with $\Delta\hat{H}$, setting $E = E_0 - i\epsilon$, where $\epsilon > 0$, we obtain

$$\text{Im} \int_0^L \{[\Delta\hat{H}G_{E_0-i\epsilon}]_{\vec{x}'=\vec{x}}\}_{x=0^-} dy = \sum_{\sigma} \frac{\epsilon}{(E_0 - E_\sigma)^2 + \epsilon^2} \Delta E_\sigma. \quad (2.52)$$

For $\epsilon \gg \rho^{-1}(E_0)$, where $\rho^{-1}(E_0)$ is the average spacing between energy levels ($\rho(E_0)$ is the density of states), yet small compared to E_0 , the right hand side of (2.52) is the product of $\pi\rho(E_0)$ and the Lorentzian sliding average of ΔE_σ . This follows from

$$\sum_{\sigma} \frac{\epsilon/\pi}{(E_0 - E_\sigma)^2 + \epsilon^2} \cong \rho(E_0) = \frac{A}{4\pi}, \quad (2.53)$$

where the right hand equality is Weyl's formula for a well of area A and is independent of E_0 for the two-dimensional case we are treating. Equations (2.52) and (2.53) yield the following expression for the sliding average,

$$\langle \Delta E_\sigma \rangle_{E_0, \epsilon} = \frac{4}{A} \text{Im} \left\{ \int_0^L [(\Delta\hat{H}G_{E_0-i\epsilon})_{\vec{x}'=\vec{x}}]_{x=0} dy \right\} \quad (2.54)$$

which yields

$$\Gamma_m = e^{-2i\phi_m(k_x)}, \quad (2.59)$$

$$\phi_m(k_x) = \arctan\left(\frac{\alpha_m}{k_x}\right), \quad (2.60)$$

where

$$\alpha_m = \sqrt{k_B^2 + \left(\frac{m\pi}{L}\right)^2 - E_0}. \quad (2.61)$$

Inserting (2.57) into (2.62), and making use of our results for $\hat{H}_{A,S}$ in Eqs. (2.12) and (2.13), we obtain

$$\langle \Delta E_\sigma \rangle_{E_0, \epsilon} = \frac{4}{A} \sum_m \int_{-\infty}^{+\infty} dk_x \frac{\epsilon}{\pi} \left\{ \frac{\alpha_m}{\sinh(2\alpha_m \Delta)} \frac{Re[1 + \Gamma_m(k_x)]}{[k_x^2 + (\frac{m\pi}{L})^2 - E_0]^2 + \epsilon^2} \right\}. \quad (2.62)$$

In writing (2.62) we have neglected $Im[\Gamma_m(k_x)]$ which will be valid for $E_0 \gg \epsilon$. In this same limit we may also neglect the variation of $\Gamma_m(k_x)$ and α_m in the range,

$$\epsilon \geq \left[k_x^2 + \left(\frac{m\pi}{L}\right)^2 - E_0 \right] \geq -\epsilon.$$

Thus we set $k_x = k_{x_0} \equiv \sqrt{E_0 - (m\pi/L)^2}$ and $\alpha_{m_0} = \sqrt{k_B^2 + (m\pi/L)^2 - E_0}$ in (2.62), yielding

$$\langle \Delta E \rangle = \frac{4}{A} \sum_{m=1}^M \frac{\alpha_{m_0}}{k_{x_0}} \frac{Re[1 + \Gamma_m(k_{x_0})]}{\sinh(2\alpha_{m_0} \Delta)}, \quad (2.63)$$

where we have cut the sum over m off at M [defined by Eq. (2.30)] and dropped the subscript E_0, ϵ . Using our result (2.59) for Γ_m , we finally obtain

$$\langle \Delta E \rangle = \frac{4L}{A\Delta} \sum_{m=1}^M \left(\frac{2\Delta\theta}{\pi} \right) \frac{k_{x_0}^2 \alpha_{m_0}}{k_B^2 \sinh(2\alpha_{m_0} \Delta)}, \quad (2.64)$$

where we have used $\Delta\theta_m = \pi/(k_x L)$, valid in the limit $m \gg 1$. This result is the same as our Eq. (2.40) derived for the chaotic shape, thus demonstrating that it is independent of how the well is shaped, as well as whether the orbits are chaotic, integrable, or mixed.

2.6 Discussion and Conclusion

Defining fluctuating weights w_m by

$$w_m = \frac{\xi_m^2 \mu_m}{\sum_{m=1}^M \xi_m^2 \mu_m}, \quad (2.65)$$

Eq. (2.37) takes the form of a weighted average,

$$\Delta E = \sum_{m=1}^M w_m \delta E_m, \quad (2.66)$$

where δE_m is defined in (2.38). For the case of rectangular wells, the unperturbed states ($\Delta \rightarrow \infty$) are

$$\psi_0(x, y) = \sin\left(\frac{m\pi y}{L}\right) \sin(k_{x,m}x - \phi_m), \quad (2.67)$$

where m labels the vertical wavenumber, $k_y = m\pi/L$. Insertion of (2.67) into the perturbation result (2.24) yields

$$\Delta E = \delta E_m. \quad (2.68)$$

Thus ΔE in the chaotic case is a weighted average over the tunneling rates for the rectangular well. This self-averaging, done by each individual chaotic mode, is responsible for the reduction of the mode-to-mode tunneling fluctuations. The larger the number of m values effectively taking part in the averaging, the lower the fluctuation level. Since this number scales with $M \approx kL/\pi$, we conclude that, as shown in Sec. 2.6.1, the fluctuation level for splittings in the chaotic case decreases with increasing kL ,

$$\frac{\sigma}{\langle \Delta E \rangle} = \frac{\langle (\Delta E - \langle \Delta E \rangle)^2 \rangle^{1/2}}{\langle \Delta E \rangle} \sim (kL)^{-1/2}, \quad (2.69)$$

and that the ratio of the fluctuation level for the chaotic case to that for the integrable case has this same predominant scaling. Thus the difference between fluctuation levels of the chaotic and integrable cases becomes large with increasing energy (however, if E is increased, V_B may also have to be increased, in order to keep E/V_B less than one).

Equation (2.66) also provides a simple way of understanding our observation that the sliding averages for the chaotic and rectangular well cases are the same. We first recall that the weights w_m given by (2.65) have averages corresponding to an isotropic distribution of incident plane waves on the boundary. Furthermore, according to Weyl's law for two dimensional billiards, the distribution of modes in k -space is isotropic and uniform. Thus, if the sliding average for the rectangle includes a sufficient number of modes in the averaging window, then it produces an isotropic averaging, just as in the chaotic case. Thus, as observed in Fig. 2.3 and demonstrated by the analysis of Sec. 2.5, we expect the chaotic and regular wells to yield the same sliding average.

We remark that, from the experimental point of view, due to the short wavelength necessary for observing semiclassical effects, the symmetry required for realizing splitting statistics may be stringent. Another, much less demanding, situation is that of tunneling from a single well into a region of outgoing quantum waves, as pictured in Fig. 2.9. In this case the energy levels acquire an imaginary part, $E_\sigma = E_\sigma^{(R)} - iE_\sigma^{(I)}$, where, for $E_\sigma^{(R)} < V_B$ and Δ sufficiently large, $E_\sigma^{(R)} \gg E_\sigma^{(I)}$, so that a perturbation analysis similar to that in Secs. 2.2 and 2.3 can be applied. The result is that the statistics of the tunneling escape rates $\{E_\sigma^{(I)}\}$ are similar to those

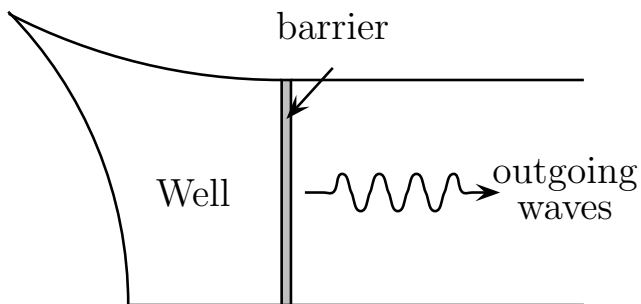


Figure 2.9: Tunneling from a single well into an unconfined region.

for the tunneling-induced splittings $\{\Delta E_\sigma\}$. The statistical model for $\{E_\sigma^{(I)}\}$ (analogous to Eq. (2.37)) is derived in Sec. 2.6.2. The result has the same form as that given in Eqs. (2.65), (2.66). Thus the subsequent discussion, including Eq. (2.69), also applies for $\{E_\sigma^{(I)}\}$. Hence the same chaos regularization of tunneling is expected to apply for the escape rates in situations like that shown in Fig. 2.9

In conclusion we have presented a semiclassical analysis of energy level splitting of symmetric, quantum-dot-type, double-well systems, where the wells are separated by a tunneling barrier. Our analysis quantitatively explains the observed mean splittings and their fluctuations. The mean is found to be independent of the well shape and independent of whether the well orbits are chaotic or not. In contrast, the fluctuation statistics are vastly different when the well orbits are integrable, as compared to when they are chaotic, with the chaotic case yielding much reduced fluctuations when the lateral barrier length is large compared to a wavelength.

2.6.1 Variance of the Splittings for Large kL and Large $k_B\Delta$

Here we apply (2.37) to obtain an analytical expression for the variance of $\{\Delta E_\sigma\}$ for large kL and large $k_B\Delta$. Because of the approximations that we will use, the result will not be applicable for explaining the numerical results in Fig. 2.2 (b), and this is why we used the Monte Carlo procedure in Sec. 2.4. Nevertheless, this calculation is instructive; e.g., it clearly shows that the splitting variance relative to the mean $\langle\Delta E\rangle$ decreases as $(kL)^{-1}$ for increasing kL (also see the discussion in Sec. 2.6).

We begin by using (2.40) and (2.42) to re-express (2.37) as

$$\Delta E = \langle\Delta E\rangle \frac{1 + \alpha}{1 + \beta}, \quad (2.70)$$

where

$$\alpha = \frac{\sum_{m=1}^M \mu_m \delta E_m (\xi_m^2 - 1)}{\langle\Delta E\rangle}, \quad (2.71)$$

$$\beta = \sum_{m=1}^M \mu_m (\xi_m^2 - 1), \quad (2.72)$$

with $\langle\Delta E\rangle$ being the expression given by (2.40), and $\langle\alpha\rangle = \langle\beta\rangle = 0$ by virtue of $\langle\xi_m^2\rangle = 1$.

Anticipating that α and β are small compared to one (i.e., $\langle\alpha^2\rangle, \langle\beta^2\rangle \ll 1$), we expand (2.70) to obtain

$$\frac{\Delta E - \langle\Delta E\rangle}{\langle\Delta E\rangle} \cong \alpha - \beta. \quad (2.73)$$

Squaring (2.73) and averaging over realizations of the Gaussian random variables $\{\xi_m\}$ yields the following expression for the variance σ^2 .

$$\frac{\sigma^2}{\langle\Delta E\rangle^2} = 2 \sum_{m=1}^M \mu_m^2 \left[\frac{\delta E_m}{\langle\Delta E\rangle} - 1 \right]^2, \quad (2.74)$$

where we have used $\langle(\xi_m^2 - 1)(\xi_{m'}^2 - 1)\rangle = 2\delta_{mm'}$. For large M (i.e., large kL), we now attempt to approximate the summation of the right hand side of (2.74) by an integral over θ . For large M and θ_m not too close to $\pi/2$,

$$\mu_m \cong \frac{2}{kL \cos \theta_m}; \quad (2.75)$$

see Fig. 2.4. Using this in (2.74) we obtain

$$\frac{\sigma^2}{\langle \Delta E \rangle^2} = 2 \int_0^{\theta_*} \frac{2}{kL \cos \theta} \left[\frac{\delta E(\theta)}{\langle \Delta E \rangle} - 1 \right]^2 \frac{d\theta}{\pi/2}. \quad (2.76)$$

While the upper limit of the integration in (2.76) might nominally be supposed to be $\pi/2$, we have instead replaced it by θ_* , because, due to the term $1/\cos \theta$ in the integrand, the integral diverges logarithmically at $\theta_* = \pi/2$. This is an artifact of our approximation (2.75), which is not accurate for small $\cos \theta_m$ (e.g., it predicts $\mu_m \rightarrow \infty$ as $\theta_m \rightarrow \pi/2$). Since the divergence is logarithmic, the size of the contribution to the variance from the vicinity of θ near $\pi/2$, can be roughly estimated by appropriately cutting off the integral at θ_* slightly below $\pi/2$. Based on the construction shown in Fig. 2.10, we choose as an appropriate cutoff

$$\theta_* = \frac{\pi}{2} - \sqrt{\frac{2\pi\gamma}{kL}}, \quad (2.77)$$

where γ is of order one. The result will be insensitive to a precise choice of γ . The contribution from θ near $\pi/2$ is then estimated to be of the order of

$$\frac{1}{kL} \ln \left(\frac{kL}{2\pi\gamma} \right), \quad (2.78)$$

where we obtain this result by approximating $\cos \theta$ by $(\pi/2 - \theta)$ setting $\theta = \pi/2$ in $\delta E(\theta)$, and noting from Eq. (2.41) that $\delta E(\pi/2) = 0$.

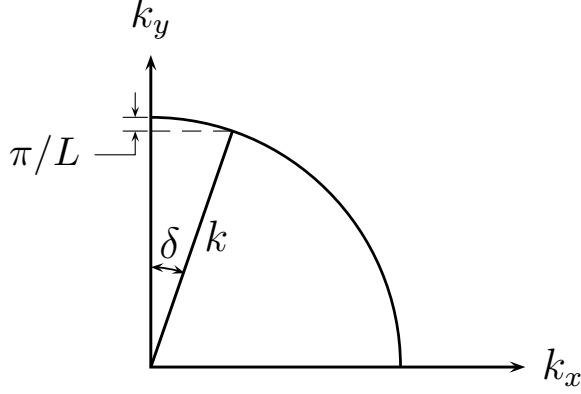


Figure 2.10: For $kL/\pi \ll 1$, the angle $\delta \cong \sqrt{2\pi/kL}$.

We now argue that, in an appropriate parameter regime, the contribution (2.78) is dominated by the contribution to the integral from the vicinity of $\theta = 0$. In particular, for $k_B\Delta$ sufficiently large,

$$\frac{\delta E(0)}{\langle \Delta E \rangle} \gg 1. \quad (2.79)$$

For $\theta^2 \ll 1$, Eqs. (2.41)- (2.51) yield

$$\left(\frac{\delta E(\theta)}{\langle \Delta E \rangle} \right)^2 \cong \left(\frac{16}{\pi} \right) \nu \exp(-2\nu\theta^2), \quad (2.80)$$

where

$$\nu = \frac{k_B\Delta}{\sqrt{1 - (k/k_B)^2}}. \quad (2.81)$$

E.g., for future reference we regard (2.79) to be satisfied for $\nu \gtrsim 5$. Using (2.79) and (2.80) in (2.76) we obtain 1

$$\frac{\sigma^2}{\langle \Delta E \rangle^2} \cong \frac{64}{\pi} \sqrt{\frac{\nu}{2\pi}} \frac{1}{kL}. \quad (2.82)$$

Comparing (2.82) and (2.78), we see that (2.82) is larger than (2.78) for $\nu \sim 5$, if

$$16 \gtrsim \ln \left(\frac{kL}{2\pi} \right) = \ln \left(\frac{L}{\lambda} \right), \quad (2.83)$$

where $\lambda = 2\pi/k$. Thus we conclude from (2.83) that, even when L is many wavelengths λ , the log contribution, (2.78), is not significant and the predominant scaling of σ is as in (2.82),

$$\frac{\sigma}{\langle \Delta E \rangle} \sim (kL)^{-1/2}. \quad (2.84)$$

2.6.2 Escape Rate from a Chaotic Well to an Open Region

In this section we outline the analysis of the situation illustrated in Fig. 2.9. Again taking $x = 0$ to coincide with the left face of the barrier, 2Δ to be the barrier width, and L to be the vertical dimension of the barrier boundary, we write $\psi(x, y)$ in $x \geq 2\Delta$ and $0 \leq x \leq 2\Delta$ respectively as

$$\psi(x, y) = \sum_{m=1}^{\infty} D_m \sin\left(\frac{m\pi y}{L}\right) e^{ik_{x,m}x}, \quad (2.85)$$

$$\psi(x, y) = \sum_{m=1}^{\infty} (E_m e^{-\alpha_m x} + F_m e^{\alpha_m x}) \sin\left(\frac{m\pi y}{L}\right), \quad (2.86)$$

where

$$k_{x,m} = \sqrt{E - \left(\frac{m\pi}{L}\right)^2} \quad \text{for } E \geq \left(\frac{m\pi}{L}\right)^2, \quad (2.87)$$

$$k_{x,m} = i\sqrt{\left(\frac{m\pi}{L}\right)^2 - E} \quad \text{for } E \leq \left(\frac{m\pi}{L}\right)^2, \quad (2.88)$$

$$\alpha_m = \sqrt{\left(\frac{m\pi}{L}\right)^2 + V_B - E}, \quad V_B > E. \quad (2.89)$$

Applying the continuity of ψ and $\partial\psi/\partial x$ at $x = 2\Delta$ and at $x = 0$, we obtain the boundary condition at $x = 0^-$,

$$\left[\frac{\partial\psi(x, y)}{\partial x} \right]_{x=0^-} + \hat{H}[\psi(0^-, y)] = 0, \quad (2.90)$$

where \hat{H} is defined in a manner analogous to Eqs. (2.12) - (2.14) with

$$\hat{H}^{(m)} = \alpha_m \frac{(\alpha_m - ik_m) - (\alpha_m + ik_m) \exp(-4\alpha_m \Delta)}{(\alpha_m - ik_m) + (\alpha_m + ik_m) \exp(-4\alpha_m \Delta)}. \quad (2.91)$$

Proceeding as in Sec. 2.2.3, perturbation theory gives

$$E - E_0 = \frac{\int_0^L \{\psi_0 \Delta \hat{H}[\psi_0]\}_{x=0^-} dy}{\int_{LW} \psi_0^2 dx dy}, \quad (2.92)$$

where $E = E^{(R)} - iE^{(I)}$, $\Delta \hat{H} = \hat{H} - \hat{H}_0$, and \hat{H}_0 is defined by (2.18). Taking the imaginary part of Eq. (2.92), we obtain an expression for the tunneling rate,

$$E^{(I)} = -\frac{\int_0^L \{\psi_0 \text{Im}(\Delta \hat{H}[\psi_0])\}_{x=0^-} dy}{\int_{LW} \psi_0^2 dx dy}. \quad (2.93)$$

Assuming that $\exp(-4\alpha_m \Delta)$ is small we find that

$$\text{Im}(\hat{H}^{(m)} - \hat{H}_0^{(m)}) \approx -\frac{4}{V_B} \alpha_m^2 k_{x,m} \exp(-4\alpha_m \Delta), \quad (2.94)$$

which yields

$$E^{(I)} = \frac{2L}{V_B} \frac{\sum_m C_m^2 \alpha_m^2 k_{x,m} \exp(-4\alpha_m \Delta)}{\int_{LW} \psi_0^2 dx dy}, \quad (2.95)$$

where (2.95) is analogous to (2.24). We can now easily parallel the steps of Sec. 2.3 that lead to Eq. (2.37). Indeed, comparing (2.95) and (2.24), we can obtain (2.95) from (2.24) by making the following replacement in (2.24):

$$\frac{1}{\sinh 2\alpha_m \Delta} \longrightarrow \frac{2}{V_B} \alpha_m k_{x,m} \exp(-4\alpha_m \Delta). \quad (2.96)$$

Using the replacement (2.96) in Eq. (2.37), we obtain the following statistical model for the tunneling rates from a chaotic well to an open region,

$$E^{(I)} = \sum_{m=1}^M w_m E_m^{(I)}, \quad (2.97)$$

where

$$E_m^{(I)} = \frac{8Lk_{x,m}^3 \alpha_m^2 \exp(-4\alpha_m \Delta)}{AV_B^2}, \quad (2.98)$$

and w_m is as defined in Eq. (2.65). Note that Eq. (2.97) has the same form as Eq. (2.66).

2.6.3 Model for the Upper and Lower Bounds on the Splitting Variance

In this section we consider a model which is similar to that in Fig. 2.6, but with a modification that will facilitate analysis. This model is shown in Fig. 2.11. The main feature of this model is the addition of a thin horizontal hard, thin septum a distance L from the bottom of the center of the billiard. This septum separates the region near the vertical part of the well boundary abutting the potential barrier (labeled Region 2 in the figure), from that abutting the vertical hard wall well boundary segment (labeled Region 1 in the figure). Using this model we now present an analysis supporting our claim that, as the parameter, $L/(L + \hat{L})$ (\hat{L} is defined in Fig. 2.11), varies from 1 to 0, the splitting variance $\sigma_{\Delta E}^2$, transitions from the lower bound, Eq. (2.49), to the upper bound, Eq. (2.37).

Applying the random plane wave hypothesis to Region 2, we model the statistics of the spatial averages over Region 2 of ψ_0^2 for given modes as

$$(\bar{\psi}_0^2)_2 = \sum_{m=1}^M \mu_m \xi_m^2, \quad M = \text{Int} \left(\frac{kL}{\pi} \right), \quad (2.99)$$

where the overbar denotes spatial average, $\sum_{m=1}^M \mu_m = 1$, ξ_m are i.i.d. Gaussian

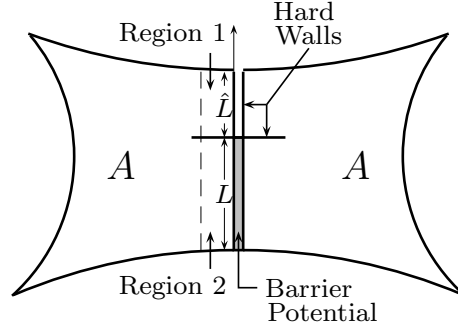


Figure 2.11: Model billiard for the analysis in Sec. 2.6.3.

variables,

$$\langle \xi_m \xi_{m'} \rangle = \langle \xi^2 \rangle \delta_{mm'}, \quad (2.100)$$

and a given random realization of the ξ_m is hypothesized to statistically model a given mode. Doing the same thing for Region 1, we model the statistics of spatial averages of ψ_0^2 over Region 1 for given modes as

$$(\bar{\psi}_0^2)_1 = \sum_{\hat{m}=1}^{\hat{M}} \hat{\mu}_{\hat{m}} \hat{\xi}_{\hat{m}}^2, \quad \hat{M} = \text{Int} \left(\frac{k \hat{L}}{\pi} \right), \quad (2.101)$$

with similar definition of $\hat{\mu}_{\hat{m}}$ and $\hat{\xi}_{\hat{m}}$. Averaging over many modes (such average are denoted $\langle \dots \rangle$),

$$\langle (\bar{\psi}_0^2)_2 \rangle = \langle \xi^2 \rangle, \quad \langle (\bar{\psi}_0^2)_1 \rangle = \langle \hat{\xi}^2 \rangle. \quad (2.102)$$

Since we expect the model averages of ψ_0^2 over any region to be the same, $\langle \xi^2 \rangle = \langle \hat{\xi}^2 \rangle$, and we define $\langle \xi^2 \rangle = \langle \hat{\xi}^2 \rangle = 1$.

We now adapt the additional model hypothesis of perfect, model by mode, correlation between the average of ψ_0^2 over the whole region A and its average over the combined area of Region 1 plus Region 2. While this may not really apply, it

should yield a valid qualitative model for the issue that we wish to study. This gives

$$(\bar{\psi}_0^2)_A = \frac{L}{L + \hat{L}} (\bar{\psi}_0^2)_2 + \frac{\hat{L}}{L + \hat{L}} (\bar{\psi}_0^2)_1, \quad (2.103)$$

where

$$\frac{L}{(L + \hat{L})} = \frac{\text{Area of Region 2}}{\text{Area of Regions 1} + 2}. \quad (2.104)$$

Letting $r \equiv L/(L + \hat{L})$ and following our previous work, application of Herring's formula gives

$$\frac{\Delta E}{\langle \Delta E \rangle} = \frac{1 + \alpha}{1 + r\beta + (1 - r)\gamma}, \quad (2.105)$$

where

$$\begin{aligned} \alpha &= \sum_{m=1}^M \mu_m \frac{\delta E_m}{\langle \Delta E \rangle} (\xi_m^2 - 1), \\ \beta &= \sum_{m=1}^M \mu_m (\xi_m^2 - 1), \\ \gamma &= \sum_{\hat{m}=1}^{\hat{M}} \hat{\mu}_{\hat{m}} (\hat{\xi}_{\hat{m}}^2 - 1), \\ \langle \alpha \rangle &= \langle \beta \rangle = \langle \gamma \rangle = 0. \end{aligned} \quad (2.106)$$

Expanding for small $\alpha \sim \beta \sim \gamma \ll 1$, we obtain the following expression for the normalized splitting fluctuation δ ,

$$\delta \equiv \frac{\Delta E - \langle \Delta E \rangle}{\langle \Delta E \rangle} \cong \alpha - r\beta + (1 - r)\gamma. \quad (2.107)$$

The normalized splitting variance is thus

$$\langle \delta^2 \rangle \cong \langle \alpha^2 \rangle - 2r\langle \alpha\beta \rangle + (1 - r)^2\langle \gamma^2 \rangle, \quad (2.108)$$

where we have used $\langle \alpha\gamma \rangle = \langle \beta\gamma \rangle = 0$, reflecting the assumption that $\langle \xi_m \hat{\xi}_{\hat{m}} \rangle = 0$ for all m and \hat{m} .

Say we keep k , L and A fixed and vary \hat{L} , which is equivalent to keeping α and β fixed and varying r . How does $\langle \delta^2 \rangle$ change as r varies?

From Eq. (2.78) of Sec. 2.6.1

$$\frac{\langle \gamma^2 \rangle}{\langle \beta^2 \rangle} = \frac{L \ln(k\hat{L}/2\pi\gamma)}{\hat{L} \ln(kL/2\pi\gamma)}. \quad (2.109)$$

Thus for $kL \sim k\hat{L} \gg 1$, we have $\langle \gamma^2 \rangle \cong (L/\hat{L})\langle \beta^2 \rangle$, which, when used in our expression for $\langle \gamma^2 \rangle$, gives

$$\langle \delta^2 \rangle = r\langle (\alpha - \beta)^2 \rangle + (1 - r)\langle \alpha^2 \rangle, \quad 1 \geq r \geq 0. \quad (2.110)$$

Thus $\langle \delta^2 \rangle$ varies linearly from its largest value, $\langle \alpha^2 \rangle$ at $r = 0$ (corresponding to Eq. (2.49)), to its smallest value, $\langle (\alpha - \beta)^2 \rangle$ at $r = 1$ (corresponding to Eq. (2.37)).

Chapter 3

Statistical Model of Short Wavelength Transport Through Cavities with Coexisting Chaotic and Regular Ray Trajectories

3.1 Introduction

In principle, for a given configuration, properties of wave systems are completely determined, and thus are not random. However, at short wavelength, these properties can be very sensitively dependent on small configurational changes or changes of the free space wavelength. If the configuration or free space wavelength is regarded as slightly uncertain within some small range and the wave properties vary wildly in this range, then a statistical approach may be warranted. This type of approach was originally introduced by E. Wigner in reference to the energy levels of large nuclei [6, 7, 8, 9, 1, 2], and later employed to study classically chaotic quantum systems [1, 3]. Here we focus on quasi-two-dimensional microwave cavities and quantum dots which couple to an external environment through suitable openings (called ‘leads’ or ‘ports’). The statistical properties in chaotic cavities with external connections have been well studied using various approaches, e.g., the ‘Poisson Kernel’ [18, 19, 20, 21, 14] or the ‘Random Coupling Model’ (RCM) [57, 58, 59]. The RCM (employed in this chapter) focuses on impedance matrices (related to scattering matrices through an elementary transformation) and replaces the eigenfunctions

and eigenvalues in the impedance formula by suitably chosen random quantities. Past work has shown that the RCM, and, equivalently, the Poisson Kernel yield results that agree well with statistical data obtained from experiments and numerical computations on microwave cavities [12, 13, 14, 15]. However, in general, such systems may have not only either all chaotic or all regular orbits, but also typically have a mixture of coexisting chaotic and regular orbits. We called such systems ‘mixed’. The statistical properties of impedance matrices in mixed systems is the subject of this chapter.

For specificity we focus on a particular mixed system, a ‘mushroom’ cavity (Fig. 3.1(a)) [60], which has a clearly divided phase space [61].¹ For most modes of this system, we find that it is possible to separate them into two classes, regular and chaotic (this may not hold for other systems). Using this separation, we decompose the impedance formula into chaotic and regular parts. We then derive the probability distribution associated with the chaotic part of the impedance, while, for the regular part we utilize exact (numerically calculated) or approximate theoretical eigenmodes. To test our theory, we numerically solve for eigenvalues and eigenfunctions of our mushroom cavity and insert them into the exact formula.

¹More generic systems can display infinite hierarchies of KAM island chains encircling other KAM island chains with chaos intermixed. This type of intermingling of chaotic and nonchaotic orbits on all scales is not present in the mushroom billiard where non-smooth shape is designed to yield a clear division between chaotic and regular phase space region. Our motivation in using the mushroom shape is that the simplicity provided by its clear division of chaotic and regular phase space allows a potentially simpler theory. We hope that our work can serve as a basis for future study applicable to the case of generic phase space structure

This chapter is organized as follows. In Sec. 3.2 we review the impedance formula in two dimensional cavities, introduce the random coupling model, generalize the RCM to mixed systems, introduce the mushroom cavity (an example of a mixed system), and apply our generalized RCM to this cavity. In Sec. 3.3 we numerically calculate the impedance matrix of the mushroom cavity and compare the numerical results with results from our statistical theory. Conclusions and discussion are presented in Sec. 3.4.

The general problem of wave properties of systems whose ray equations have a mixed phase space was first addressed by Berry and Robnik [43] who studied the spectra of mixed closed systems. Subsequently, many other researchers have investigated spectra and wavefunctions of closed systems with mixed ray orbit phase space (e.g., [27, 64, 65]). The problem of characterizing the input/output properties of mixed open systems, however, has, to our knowledge, been addressed relatively little [66, 67, 68].

3.2 Review of Theory

3.2.1 Impedance of a cavity

In the presentation that follows, we consider the context of electromagnetic waves. However, we emphasized that, with appropriate notational changes, these considerations apply equally well to quantum waves, acoustic waves, elastic waves, etc.

We consider a vacuum-filled, quasi-two-dimensional (vertically thin) microwave

cavity with cavity height h and M ports as shown in Fig. 3.1. We denote the two dimensional interior of the cavity by $\Omega \in \mathbb{R}^2$. If the frequency is not too high (i.e., the wavelength is greater than $2h$), then only vertical electric fields are excited inside the cavity,

$$\vec{E} = E_z(\vec{x}, t)\hat{z}, \quad (3.1)$$

where $\vec{x} \in \Omega$ is a two dimensional position vector. The surface charge density on the bottom plate of such a cavity is $\rho_s = -\epsilon_0 E_z$, and the voltage difference between the two plates is

$$V_T(\vec{x}, t) = hE_z(\vec{x}, t). \quad (3.2)$$

The surface current density on the bottom plate is related to the magnetic field, \vec{H} , which is perpendicular to \vec{E} , by

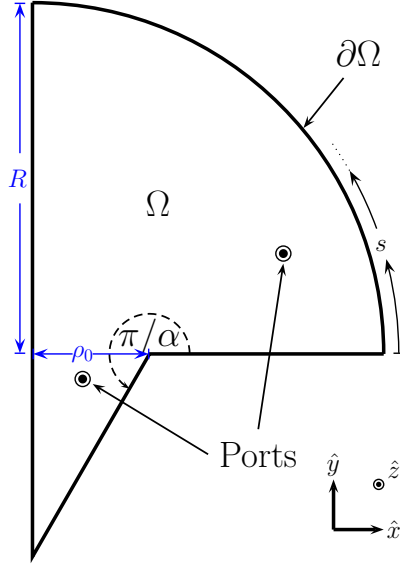
$$\vec{J}_s = \vec{H} \times \hat{z}. \quad (3.3)$$

We assume that the fields are excited by M localized current sources, which inject surface charge density on the bottom plate

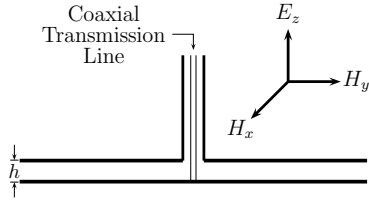
$$\dot{\rho}_s(\vec{x}, t) = \sum_{j=1}^M I_j(t)u_j(\vec{x}), \quad (3.4)$$

where $u_j(\vec{x})$ is the normalized profile function of port j , $\int d^2\vec{x}u_j(\vec{x}) = 1$, and we regard Eq. (3.4) as modeling the currents induced by the transmission line fed ports shown in Fig. 3.1. With Eq. (3.3), the continuity equation for the surface charge can be written as

$$\frac{\partial}{\partial t}(-\epsilon_0 E_z) + \vec{\nabla} \cdot (\vec{H} \times \hat{z}) = \dot{\rho}_s = \sum_{j=1}^M I_j u_j. \quad (3.5)$$



(a)



(b)

Figure 3.1: (a) Top view of the quasi-two dimensional cavity coupling with $M = 2$ ports (fed by coaxial transmission lines), where the region interior to the cavity is denoted Ω . (b) Side view of the cavity at a port. In some previous works, a mushroom billiard similar to that in (a) was used [60], but the billiard section below the quarter circular cap being a rectangle of width ρ_0 . This, however, introduced neutrally stable ray orbits that bounce back and forth horizontally between the vertical walls of the rectangle. By using the above triangular bottom part (as in Ref. [63]) (a) we avoid the non-generic effects of such orbits.

Differentiating Eq. (3.5), using Faraday's law, $\nabla \times \vec{E} = -\mu_0 \partial \vec{H} / \partial t$, and expressing E_z by Eq. (3.2), we obtain

$$\frac{1}{c^2} \frac{\partial^2}{\partial t^2} V_T - \nabla^2 V_T = h\mu_0 \sum_{j=1}^M u_j \frac{\partial}{\partial t} I_j, \quad (3.6)$$

where $c = 1/\sqrt{\mu_0 \epsilon_0}$ is the speed of light. Assuming that $V_T(\vec{x}, t) = \hat{V}_T(\vec{x}) e^{j\omega t}$, $I_i(t) = \hat{I}_i e^{j\omega t}$, Eq. (3.6) can be rewritten as

$$(\nabla^2 + k^2) \hat{V}_T = -jkh\eta_0 \sum_{j=1}^M u_j \hat{I}_j, \quad (3.7)$$

where $k = \omega/c$, and $\eta_0 = \sqrt{\mu_0/\epsilon_0}$ is the free space impedance.

We expand \hat{V}_T in the basis of the eigenfunctions of the closed cavity, i.e.,

$$\hat{V}_T = \sum_{n=1}^{\infty} c_n \phi_n, \quad (3.8)$$

where ϕ_n satisfies the Helmholtz equation with Dirichlet boundary condition and a proper normalization condition, i.e.,

$$(\nabla^2 + k_n^2) \phi_n(\vec{x}) = 0 \quad \vec{x} \in \Omega, \quad (3.9)$$

$$\phi_n(\vec{x}) = 0 \quad \vec{x} \in \partial\Omega, \quad (3.10)$$

$$\int_{\Omega} \phi_i \phi_j d^2\vec{x} = \delta_{ij}, \quad (3.11)$$

and we order the mode labeling according to the convention, $k_{n+1}^2 \geq k_n^2$. Inserting Eq. (3.8) into Eq. (3.7), multiplying $\phi_m(\vec{x})$ and integrating over Ω , we obtain

$$c_m = -jkh\eta_0 \sum_{j=1}^M \frac{\langle u_j \phi_m \rangle \hat{I}_j}{k^2 - k_m^2}, \quad (3.12)$$

where $\langle \cdots \rangle \equiv \int_{\Omega} \cdots d^2\vec{x}$. The voltage at port i is defined as

$$\hat{V}_i = \langle u_i \hat{V}_T \rangle, \quad (3.13)$$

where the port voltages V_i are expressed in phaser form, $V_i = \hat{V}_i e^{j\omega t}$. Using Eqs. (3.8), (3.12) and (3.13), we obtain

$$\hat{V}_i = \sum_{j=1}^M Z_{ij} \hat{I}_j, \quad (3.14)$$

where the i, j element of the impedance matrix \mathbf{Z} is given by

$$Z_{ij} = -jkh\eta_0 \sum_{n=1}^{\infty} \frac{\langle u_i \phi_n \rangle \langle u_j \phi_n \rangle}{k^2 - k_n^2}. \quad (3.15)$$

Equation (3.15) states that, in a lossless cavity, the impedance is purely imaginary, since the eigenfunctions for Eqs. (3.9) and (3.10) are real. It also states that, if we know all the eigenfunctions and eigenvalues of the closed cavity, we can calculate the matrix elements of \mathbf{Z} exactly. Note that $\langle u_i \phi_n \rangle \rightarrow 0$ as the port size becomes much greater than several wavelengths. Thus, the infinite sum in Eq. (3.15) can be replaced by a finite sum, i.e.,

$$Z_{ij} = -jkh\eta_0 \sum_{n=1}^N \frac{\langle u_i \phi_n \rangle \langle u_j \phi_n \rangle}{k^2 - k_n^2}, \quad (3.16)$$

where N satisfies the condition, $2\pi/k_N \ll (\text{size of ports})$. For systems that are large compared to a wavelength ($2\pi/k$) and may have some uncertainty in their specification, it is often of practical interest to dispense with the necessity of numerically calculating all N eigenfunctions and to instead look for a statistical description. The later will be our goal.

3.2.2 Random Coupling Model

The Random Coupling Model (RCM) treats the case where typical ray orbits are *all* chaotic and is based on the supposition that, in the short wavelength limit,

the statistical properties of the impedance of a chaotic cavity can be obtained from Eq. (3.16) by replacing k_n^2 and $\langle u_i \phi_n \rangle$ by suitable random variables.

According to the Weyl's formula [39] for a two dimensional cavity of area A , the mean spacing between two adjacent eigenvalues, $k_n^2 - k_{n-1}^2$, is $4\pi/A$, i.e.,

$$\Delta \equiv \langle k_n^2 - k_{n-1}^2 \rangle = \frac{4\pi}{A}. \quad (3.17)$$

References [6, 7, 8, 9, 1, 5] state that the normalized eigenvalue spacing, $s_n \equiv (k_n^2 - k_{n-1}^2)/\Delta$, of a time-reversible chaotic system has similar statistical properties to the spacings of the eigenvalues of large matrices randomly drawn from the Gaussian Orthogonal Ensemble (GOE) of random matrices with unit mean eigenvalue spacing. In this chapter, our eigenfunctions are always real, as appropriate to time reversible systems, and, henceforth, GOE is automatically assumed when we mention random matrices.

Berry [44] argues that the wavefunction at any point in a chaotic billiard has similar statistical properties to a random superposition of many plane waves,

$$\phi_n(\vec{x}) \approx \text{Re} \left\{ \sum_{j=1}^J \alpha_j \exp(i k_n \vec{e}_j \cdot \vec{x} + i \beta_j) \right\}, \quad J \gg 1, \quad (3.18)$$

where it is assumed that \vec{x} is not too close to the billiard boundary, the wavenumber k_n is fixed, but propagation directions \vec{e}_j , amplitudes α_j , and phases β_j are random variables. To be more specific, directions and phases are uniformly distributed in $[0, 2\pi]$, and all amplitudes have the same distribution. By the central limit theorem, for $J \gg 1$, $\phi_n(\vec{x})$ evaluated at the point \vec{x} is a Gaussian random variable with zero

mean, and its variance can be determined by the normalization condition, i.e.,

$$\int_{\Omega} \phi_n^2 d^2 \vec{x} = 1, \quad (3.19)$$

which implies

$$\text{E}\{\phi_n^2\} = \frac{1}{A}. \quad (3.20)$$

The probability distribution function of the overlap integral $\langle u_i \phi_n \rangle$ is Gaussian with expectation value zero (since ϕ_n is a Gaussian with expected value zero), and by Eq. (3.18) the variance of $\langle u_i \phi_n \rangle$ is

$$\text{E}\{\langle u_i \phi_n \rangle^2\} = \frac{1}{A} \int_0^{2\pi} \frac{d\theta}{2\pi} |\bar{u}(\vec{k}_n)|^2, \quad (3.21)$$

where $\vec{k}_n = (k_n \cos \theta, k_n \sin \theta)$, and $\bar{u}(\vec{k}_n)$ is the Fourier transform of the profile function $u(\vec{x})$,

$$\bar{u}(\vec{k}_n) = \int d^2 \vec{x} u(\vec{x}) \exp(-i\vec{k}_n \cdot \vec{x}). \quad (3.22)$$

Note that, the variance of $\langle u_i \phi_n \rangle$ depends on the eigenvalue k_n^2 through Eq. (3.22) where $|\vec{k}_n| = k_n$. If $2\pi/k_n \gg$ (size of the port), the profile function of the port can be approximated by a delta function, i.e., $\langle u_i \phi_n \rangle = \phi_n(\vec{x}_i)$; if $2\pi/k_n$ is comparable to the port size, we need to consider the variations of ϕ_n over the ports. Eventually, for short enough wavelength we have $\text{E}\{\langle u_i \phi_n \rangle\} \rightarrow 0$ as $k_n \rightarrow \infty$.

For an M port system, we need to consider the same wavefunction at different positions; e.g., if $2\pi/k \gg$ (size of the port), for two ports located at \vec{x}_i and \vec{x}_j , we need to consider $\langle u_i \phi_n \rangle \cong \phi_n(\vec{x}_i)$ and $\langle u_j \phi_n \rangle \cong \phi_n(\vec{x}_j)$, which are not, in general, independent, although independence can be approximately assumed if the ports are

many wavelengths apart. In the RCM, we build in this relation by writing

$$\Phi_n \equiv [\langle u_1 \phi_n \rangle, \dots, \langle u_M \phi_n \rangle]^T = \frac{1}{\sqrt{A}} \mathbf{w}_n, \quad (3.23)$$

where the $1/\sqrt{A}$ factor is based on the expectation value of ϕ_n^2 , and \mathbf{w}_n ($n = 1, 2, \dots, N$) is an M -dimensional, zero mean, standard Gaussian random vectors whose covariance matrix may have nonzero non-diagonal elements reflecting correlation between nearby ports. We can rewrite the impedance matrix as

$$\mathbf{Z} = -jkh\eta_0 \frac{\Delta}{4\pi} \sum_{n=1}^N \frac{\mathbf{w}_n \mathbf{w}_n^T}{k^2 - k_n^2}. \quad (3.24)$$

where we have used Eq. (3.17) to replace A .

In the case of identical transmission line inputs that are far enough apart, we can neglect correlations between the ports and the covariance matrix of \mathbf{w}_n is $\mathbf{1}_{M \times M}$; i.e., $E(w^i w^j) = \delta_{ij}$ for $i, j = 1, 2, \dots, M$. In this case, we introduce the normalized reactance matrix,

$$\Xi = -\frac{1}{\pi} \sum_n \frac{\mathbf{w}_n \mathbf{w}_n^T}{\tilde{k}^2 - \tilde{k}_n^2}, \quad (3.25)$$

where $\tilde{k}^2 = k^2/\Delta$ and the mean spacing, $\tilde{k}_n^2 - \tilde{k}_{n-1}^2$, between normalized eigenvalues is one. In this case the impedance matrix becomes

$$\mathbf{Z} = j \frac{kh\eta_0}{4} \Xi. \quad (3.26)$$

Note that the normalized reactance matrix, Ξ , is independent of all system specific information, such as the cavity shape, area, etc.; namely, it is universal for all chaotic cavities with widely separated ports.

3.2.3 Impedance in Mixed Systems

For a generic two dimensional billiard, both regular and chaotic phase space regions coexist, and we call such a system mixed. Percival's conjecture [42] states that semiclassical eigenmodes in mixed systems live either in regular or chaotic regions. Our numerical computations support this conjecture (see Figs. 3.2 and 3.3). At short wavelength, the number of regular and chaotic eigenstates can be approximately counted by the Partial Weyl law [69],

$$\bar{N}_\Gamma(k^2) = \frac{A_\Gamma}{4\pi} k^2 + O(k), \quad (3.27)$$

where $\Gamma = R$ denotes regular trajectories and $\Gamma = C$ denotes chaotic trajectories, A_Γ/A is the ratio of the phase space volume occupied by Γ , and A_Γ is given by

$$A_\Gamma = \int_\Omega d^2\vec{x} \frac{1}{2\pi} \int_0^{2\pi} d\theta \zeta_\Gamma(\vec{x}, \theta). \quad (3.28)$$

Here, $\zeta_\Gamma(\vec{x}, \theta)$ is the characteristic function of Γ at (\vec{x}, θ) , i.e., $\zeta_\Gamma(\vec{x}, \theta) = 1$ if the trajectory running through \vec{x} at θ angle belongs to Γ and $\zeta_\Gamma(\vec{x}, \theta) = 0$, otherwise.

Following the above approach, we decompose (3.16) into the contributions \mathbf{Z}_R and \mathbf{Z}_C to the impedance from the regular eigenmodes and chaotic eigenmodes, as follows,

$$\mathbf{Z} = \mathbf{Z}_R + \mathbf{Z}_C, \quad (3.29a)$$

and

$$Z_{R,ij} = -jkh\eta_0 \sum_r^{N_R} \frac{\langle u_i \phi_r \rangle \langle u_j \phi_r \rangle}{k^2 - k_r^2}, \quad (3.29b)$$

$$Z_{C,ij} = -jkh\eta_0 \sum_c^{N_C} \frac{\langle u_i \phi_c \rangle \langle u_j \phi_c \rangle}{k^2 - k_c^2}, \quad (3.29c)$$

where $\phi_r(\phi_c)$ denotes regular (chaotic) wavefunctions, $r = 1, 2, \dots, N_R$ ($c = 1, 2, \dots, N_C$), and $N_R + N_C = N$.

The semiclassical wavefunction distribution for chaotic eigenfunctions in mixed systems can be described by the so-called Restricted Random Wave Model [70],

$$P_{\vec{x}}(\phi) = \frac{1}{\sqrt{2\pi\sigma^2(\vec{x})}} \exp \left[-\frac{\phi^2}{2\sigma^2(\vec{x})} \right], \quad (3.30)$$

where

$$\sigma^2(\vec{x}) = \frac{1}{2\pi A_C} \int_0^{2\pi} d\theta \zeta_C(\vec{x}, \theta). \quad (3.31)$$

In a two dimensional pure chaotic cavity, $\sigma^2 = 1/A$ is independent of \vec{x} .

The statistics of k_c^2 in mixed systems is hypothesized to be similar to the statistics of k_n^2 in chaotic systems, but the mean of the spacing between chaotic eigenvalues, $k_{c+1}^2 - k_c^2$, is given by $4\pi/A_C$, as opposed to $4\pi/A$ in the purely chaotic case. Thus, the statistics of the chaotic normalized reactance in mixed systems should be identical to the statistics of the normalized reactance in chaotic systems.

We do not expect to find explicit universal statistics for the regular eigenfunctions ϕ_r as they are dependent on the cavity shape. However, the regular normalized reactance in mixed systems is always Lorentzian distributed (see Appendix E).

3.2.4 Mushroom Billiard

The mushroom billiard [60, 71] was first introduced by Bunimovich. Since the cap of the mushroom is a quarter circle, there are orbits that never leave the cap region and are the same as the orbits in a complete quarter circle billiard having the same radius R (see Fig. 3.2(a)). These orbits are tangent to a circular caustic

with a radius C_r . If the caustic radius $C_r > \rho_0$, (see Fig. 3.1) this orbit is trapped in the cap, and is integrable. There are also chaotic orbits that travel throughout the whole billiard (Fig. 3.2(b)), visiting both the cap region and the triangular region below the cap. Thus, the mushroom billiard is an example of a mixed system.

The eigenmodes of the Helmholtz equation in a quarter circle with radius R can be described by two quantum number, $(m, n) \leftrightarrow r$, and the corresponding eigenfunction is

$$\phi_r \cong \phi_{mn}^{(0)}(\rho, \theta) = \mathcal{N}_{mn} J_m(k_{mn}\rho) \sin m\theta, \quad (3.32)$$

with normalization constant

$$\mathcal{N}_{mn} = \frac{2\sqrt{2}}{\sqrt{\pi} R J'_m(k_{mn}R)}, \quad (3.33)$$

and $\phi_{mn}^{(0)} \equiv 0$ outside the quarter circle. Here J_m is m -th order Bessel function of the first kind, k_{mn} is the eigenwavenumber such that $k_{mn}R$ is the n -th zero of J_m .

To relate the quantum eigenmodes to the classical motion [72], we first define the classical probability distribution for position ρ ,

$$P_{CL}(\rho) = \frac{\rho}{\sqrt{R^2 - C_r^2} \sqrt{\rho^2 - C_r^2}}, \quad (3.34)$$

where $P_{CL}(\rho)d\rho$ represents the fraction of time a classical trajectory spends in the interval $d\rho$ at ρ , $R > \rho > C_r$. The classical caustic radius C_r is defined in terms of the angle of incidence ϕ that the trajectory makes with respect to the boundary at R , $C_r/R = \sin \phi$. The analogous caustic radius C_r from the wavefunction (3.32) is identified by equating the Bessel function order to its argument,

$$C_r = R_{mn} \equiv \frac{m}{k_{mn}} R. \quad (3.35)$$

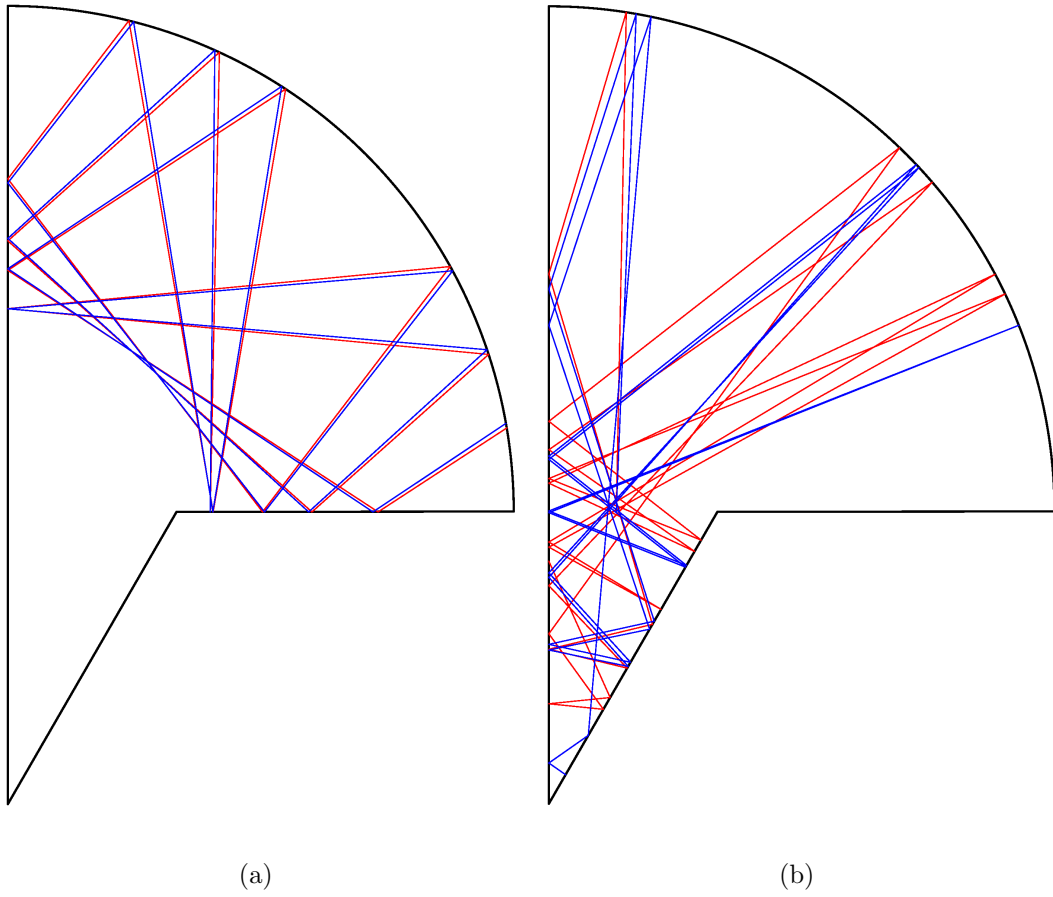


Figure 3.2: (a) Two regular orbits with slightly different initial conditions. (b) Two chaotic orbits with slightly different initial conditions.

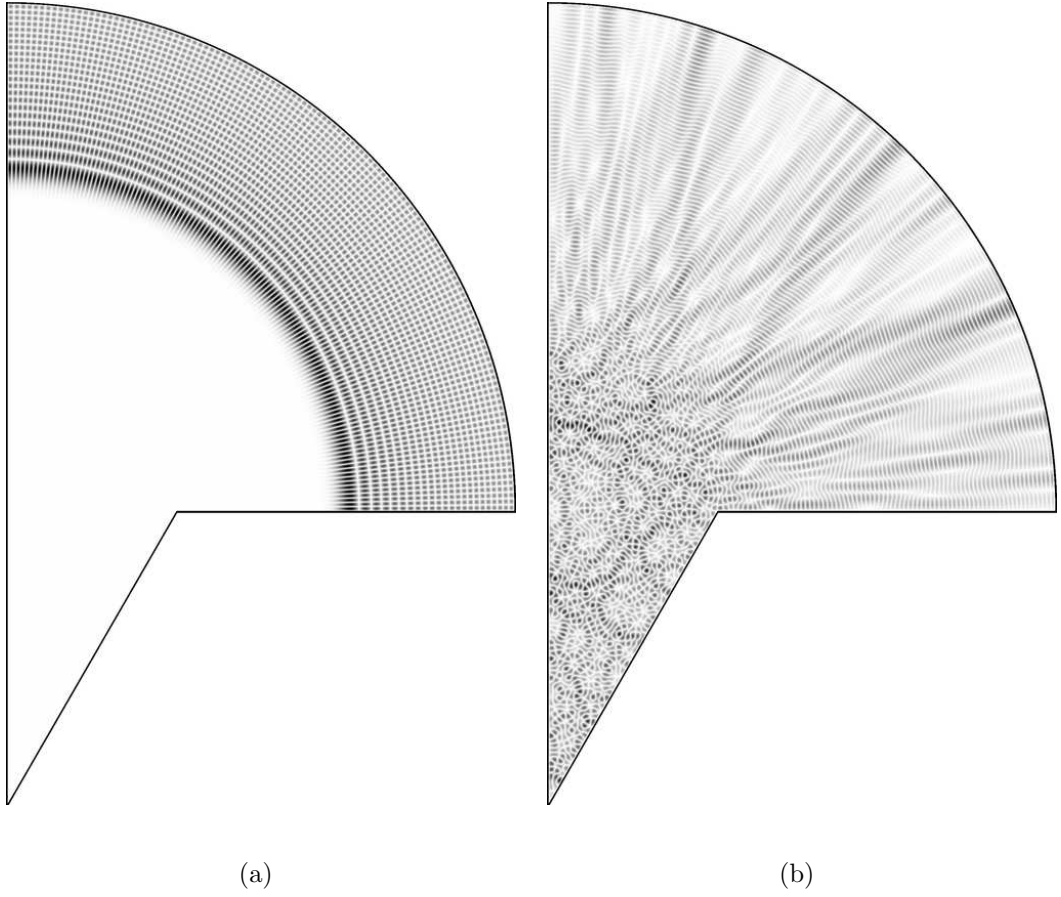


Figure 3.3: (a) Magnitude squared of the $n \approx 10,002$ -th eigenmode (regular) and $k_n \approx 253.496413$. (b) $n \approx 10,003$ -th eigenmode (chaotic) and $k_n \approx 253.501722$.

For eigenmodes with $R_{mn} < \rho_0$, the classical orbit in the full, quarter-circle billiard will travel to the root of the mushroom so the orbit in the mushroom is no longer integrable, and the corresponding $\phi_{mn}^{(0)}$ modes in (3.32) are not present in our system. Thus, we can approximate (3.29b) using the quarter circle eigenfunctions $\phi_{mn}^{(0)}$ given by Eq. (3.32),

$$Z_{ij,R} = -jkh\eta_0 \sum_{\substack{m,n \\ \rho_0 < R_{mn} < R}} \frac{\langle u_i \phi_{mn}^{(0)} \rangle \langle u_j \phi_{mn}^{(0)} \rangle}{k^2 - k_{mn}^2}. \quad (3.36)$$

In order to apply the RCM for the chaotic contribution to the mushroom cavity, we need the statistics of k_c^2 (the eigenvalues of the chaotic modes) and $\phi_c(\vec{x})$ (the corresponding eigenmodes). The distribution of k_c^2 is taken to be the same as that of the eigenvalues of a random matrix with same mean spacing $\Delta_C = \langle k_{c+1}^2 - k_c^2 \rangle = 4\pi/A_C$. Using Eq. (3.28), we can calculate the equivalent chaotic area of the mushroom cavity,

$$A_C = \frac{\sqrt{3}}{2} \rho_0^2 + \frac{1}{2} \left[\rho_0 \sqrt{R^2 - \rho_0^2} + R^2 \arcsin \left(\frac{\rho_0}{R} \right) \right]. \quad (3.37)$$

To develop a random coupling model in a mixed system, we need to rewrite Eq. (3.23) as

$$\Phi_n = \mathbf{Q} \mathbf{w}_n, \quad (3.38)$$

where \mathbf{Q} is a $M \times M$ diagonal matrix, which describes the classical chaotic probability at each port

$$Q_{ii}^2 = \int_{\Omega} u_i(\vec{x}) \sigma^2(\vec{x}) d^2 \vec{x}, \quad (3.39)$$

where $\sigma(\vec{x})$ has been defined in Eq. (3.31). Thus in the case where all transmission lines are identical, the chaotic contribution to the impedance matrix (3.29c) can be

written

$$Z_{C,ij}(k^2) = j \frac{kh\eta_0}{4} A_C Q_{ii} Q_{jj} \Xi_{ij}. \quad (3.40)$$

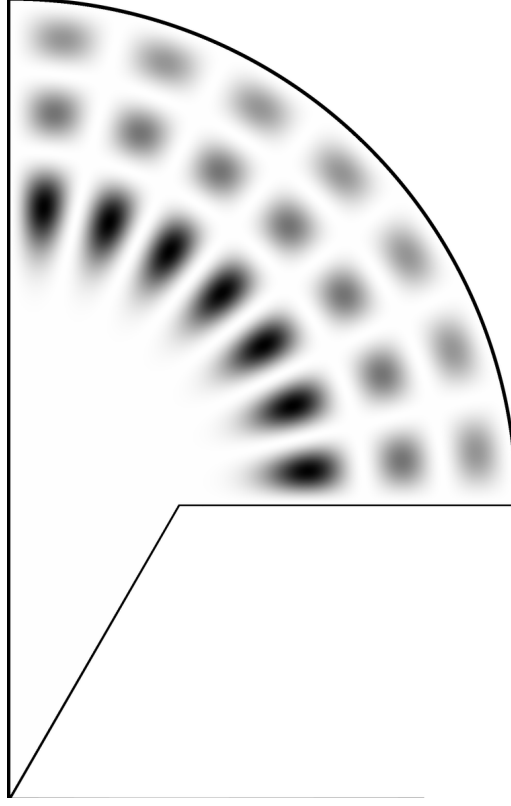
Figures 3.3(a) and 3.3(b), respectively, show representative, numerically computed, regular and chaotic eigenfunctions. These figures and others (not shown) demonstrate that, consistent with Percival’s conjecture [42], the eigenfunctions concentrate either in the regular or chaotic phase space regions thus justifying the decomposition (3.29). We next test the statistics predicted by Eq. (3.40) by comparison with direct numerical computations on our mushroom billiard example.

3.3 Numerical Experiment

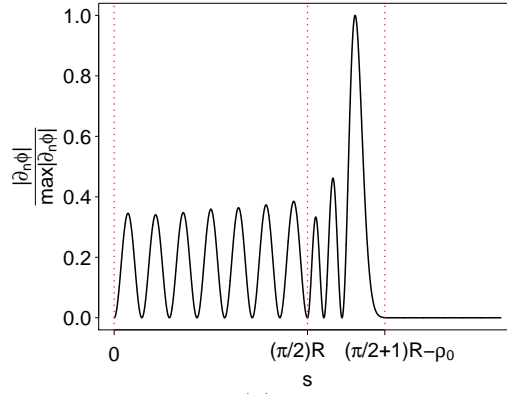
In order to test our theory for the impedance in mixed system, we numerically solve the Helmholtz equation for its eigenfunctions and eigenvalues to calculate Eq. (3.29) and compare with our statistical model, Eqs. (3.36) and (3.40). We use about 10,000 eigenmodes for the sum in Eq. (3.16). For our numerical eigenmode solutions, we use the scaling method introduced by Vergini and Saraceno [73, 63] which facilitates relatively fast solutions. More detail of this numerical technique is described in Appendix B. It has already been shown that this method yields accurate results for the eigenmodes of the Mushroom billiard [71]. We use $\alpha = 3/4$ (see Fig. 3.1(a)) rather than the value $\alpha = 2/3$ employed in Ref. [71], in order to allow application of Steed’s Method [74] for efficient evaluation of the Bessel function.

After solving for all eigenmodes, we classify these eigenfunctions by examining

the magnitude of their normal derivative as a function of the boundary coordinate s (see Fig. 3.4). By this means we can associate all our numerically calculated regular



(a)



(b)

Figure 3.4: (a) Regular eigenmode, $\phi_{14,3}(\vec{x})$, in Ω . (b) Corresponding magnitude of the normal derivative of $\phi_{14,3}(\vec{x})$ versus s .

eigenmodes with one of the analytically predicted approximate eigenmodes (3.32).

Moreover, we have also compared the regular eigenfunctions and eigenvalues determined by our numerical solutions with the approximate analytic solutions; they agree well. Thus, the regular contribution to the impedance matrix (3.29b) is very well-approximated by Eq. (3.36) with our approximate analytic regular eigenfunctions (3.32). [Alternatively, one can also characterize the regular contribution to \mathbf{Z} in a more universal manner, independent of specific geometry, as described in Appendix E.]

Our first goal is to test our statistical model for the chaotic contribution to $\mathbf{Z}_C = \mathbf{Z} - \mathbf{Z}_R$, where our model requires only simple system information (cavity area, phase space distribution) rather than all numerical eigenfunctions. For simplicity, we choose all ports to be identical, uncorrelated and point-like, i.e., $u_i(\vec{x}) = \delta(\vec{x} - \vec{x}_i)$; thus, $Q_{ii} = \sigma(\vec{x}_i)$ and Eq. (3.16) becomes

$$Z_{ij}(k^2) = jkh\eta_0\xi_{ij}(k^2), \quad (3.41)$$

where

$$\xi_{ij}(k^2) = \sum_{n=1}^N \frac{\phi_n(\vec{x}_i)\phi_n(\vec{x}_j)}{k^2 - k_n^2}, \quad (3.42)$$

and we similarly define ξ_C and ξ_R .

We choose the cutoff $N_C = N \times A_C/A = 2k^2/\Delta_C$. With this definition, the expectation value of

$$\xi_{C,ij}(k^2) = \sum_{c=1}^{2k^2/\Delta_C} \frac{\phi_c(\vec{x}_i)\phi_c(\vec{x}_j)}{k^2 - k_c^2}, \quad (3.43)$$

is zero since we expect equal number of k_c^2 such that $k_c^2 > k^2$ and $k_c^2 < k^2$. Our goal is to find the probability density functions of $\xi_{C,ij}$ if we randomly choose a k^2 (see Fig. 3.5).

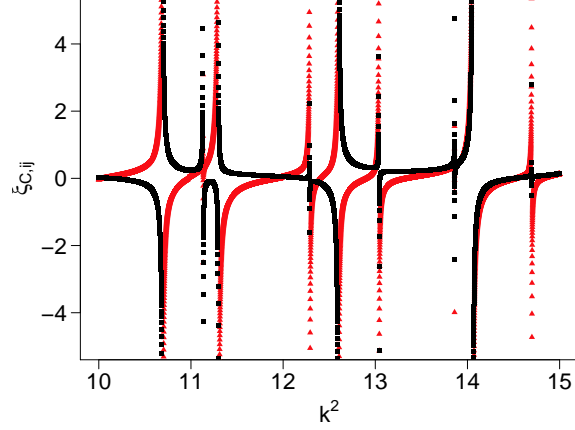


Figure 3.5: Numerical calculation of $\xi_{C,ii}$ (red triangle) and $\xi_{C,ij}$ (black square) in the mushroom cavity vs. energy (k^2).

We use a Monte Carlo method to generate realizations of Eq. (3.43). In each realization, we generate $k_1^2, k_2^2, \dots, k_{N_C}^2$ by calculating the eigenvalues of a GOE random matrix and unfold the spectra [1] such that the mean spacing is $4\pi/A_C$; we also generate $(\phi_1(\vec{x}_i), \phi_1(\vec{x}_j)), (\phi_2(\vec{x}_i), \phi_2(\vec{x}_j)), \dots, (\phi_{N_C}(\vec{x}_i), \phi_{N_C}(\vec{x}_j))$ according to Eqs. (3.30) and (3.31); then, we calculate $\xi_{C,ij}$ at each value of k^2 ; finally, we construct a probability density function for $\xi_{C,ij}$. After N_R realizations, we have N_R probability density functions for $\xi_{C,ij}$, i.e, $p_n(\xi), n = 1, \dots, N_R$. We then calculate the mean and variance of the probability density at each ξ , i.e,

$$\bar{p}(\xi) = \frac{1}{N_R} \sum_{n=1}^{N_R} p_n(\xi), \quad (3.44)$$

$$\sigma_p^2(\xi) = \frac{1}{N_R} \sum_{n=1}^{N_R} [p_n(\xi) - \bar{p}(\xi)]^2. \quad (3.45)$$

We also calculate Eq. (3.43) numerically for different port positions from the numerically determined eigenfunctions and eigenvalues and compare with our statistical model Monte Carlo method (see Fig. 3.6). Our statistical model of impedance in different port positions is the statistical model of the same normal-

ized impedance (Eq. (3.25)) with a position dependent factor, $A_C Q_{ii} Q_{jj}$, defined in Eqs. (3.28), (3.31), (3.39) and (3.40). The agreement between the numerical result and our statistical model for the different cases in Fig. 3.6 shows that the chaotic contribution to the impedance in a mixed system has the same statistics as the impedance in a purely chaotic system, provided one accounts for variations in the size of the chaotic portion of phase space accessible at the locations of the ports.

Our second goal is to compare the previous statistical model of ξ_{ij} in Ref. [58, 59] (which assumes that the classical trajectories are all chaotic) with our statistical model of ξ_{ij} [which includes chaotic contributions ($\xi_{C,ij}$) and an approximated formula for regular contributions ($\xi_{R,ij}$) defined in Eq. (3.42)]. Figure 3.7 shows that our statistical model (red solid curves) predicts the probability density function of ξ_{ij} much better than the previous result (blue dashed curves) that one would obtain by supposing that the entire phase space was chaotic.

Note that, in our formulation in Eq. (3.32), $\phi_{mn}(\vec{x}_i) = 0$ if \vec{x}_i is located in the stem of the mushroom. Therefore, if at least one port, say port i , is located in the stem of the mushroom, then $\xi_{R,ij} = 0$ and only chaotic modes contribute to the impedance, i.e., $\xi_{ij} = \xi_{C,ij}$. In the insets of Fig. 3.7, we show probability density functions of $\xi_{R,ij}$ calculated from numerically obtained regular eigenmodes and the probability density function of $\xi_{R,ij}$ calculated from our approximate regular eigenmodes (delta function (red) at $\xi_{R,ij} = 0$ for the insets to Figs. 3.7(a and b) and red curve in the inset to Fig. 3.7 (c)). In particular, we observe that the pdf widths in the insets to Figs. 3.7 (a and b) are much less than for the inset to Fig. 3.7(c). The small pdf widths in the insets to Figs. 3.7 (a and b) can perhaps be explained

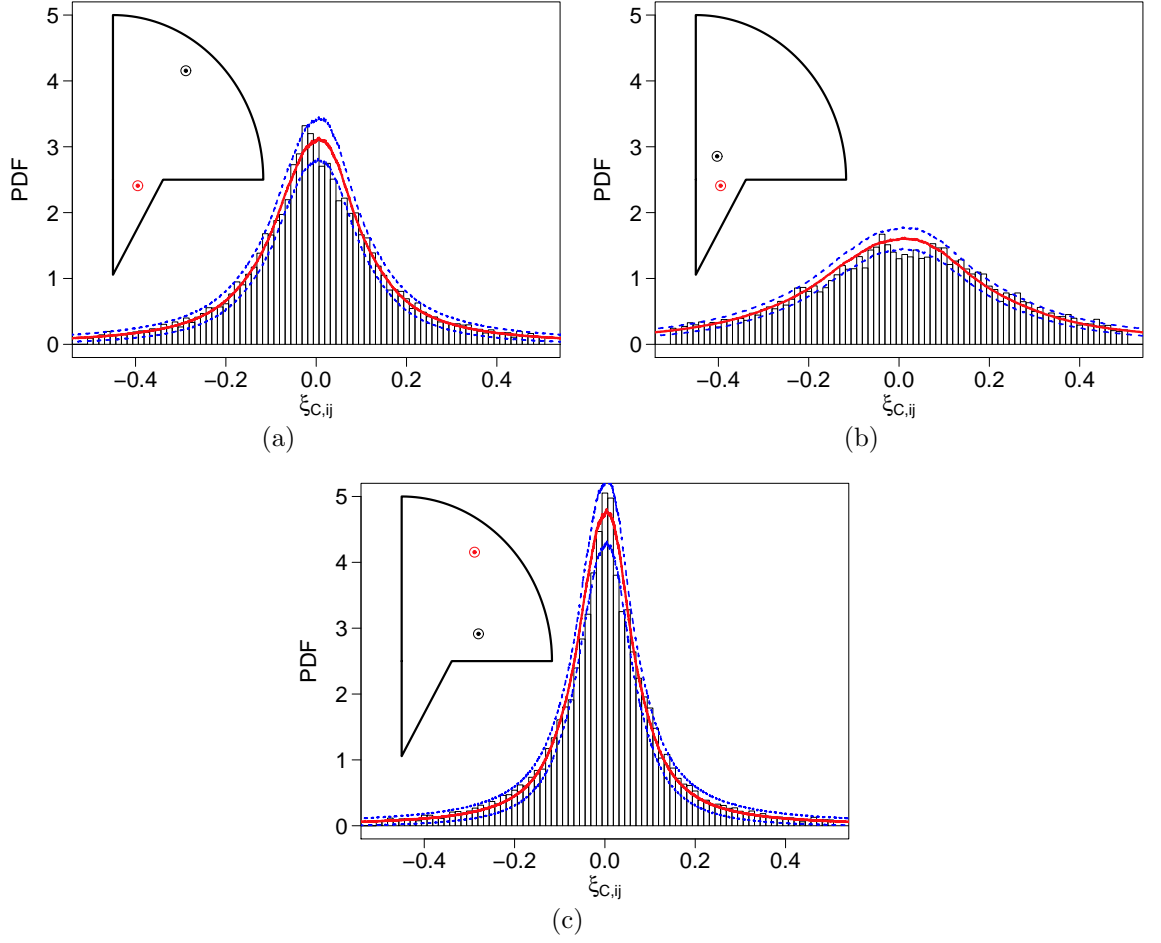


Figure 3.6: Plot of the probability density function from numerical solution (black histogram) and mean probability density function from Monte Carlo simulation (red solid curve), Eq. (3.44), with root mean squared error bounds (blue dashed curve), Eq. (3.45). The black and red dots are the position of coaxial transmission lines (ports) in case (a) one port in chaotic region and the other in mixed region (b) both pots in chaotic region (c) both ports in mixed region.

by dynamical tunneling (see [80, 81]); however, this effect is not significant in the probability density function of $\xi_{ij} = \xi_{R,ij} + \xi_{C,ij}$ which is the convolution of the probability density function of $\xi_{C,ij}$ and $\xi_{R,ij}$.

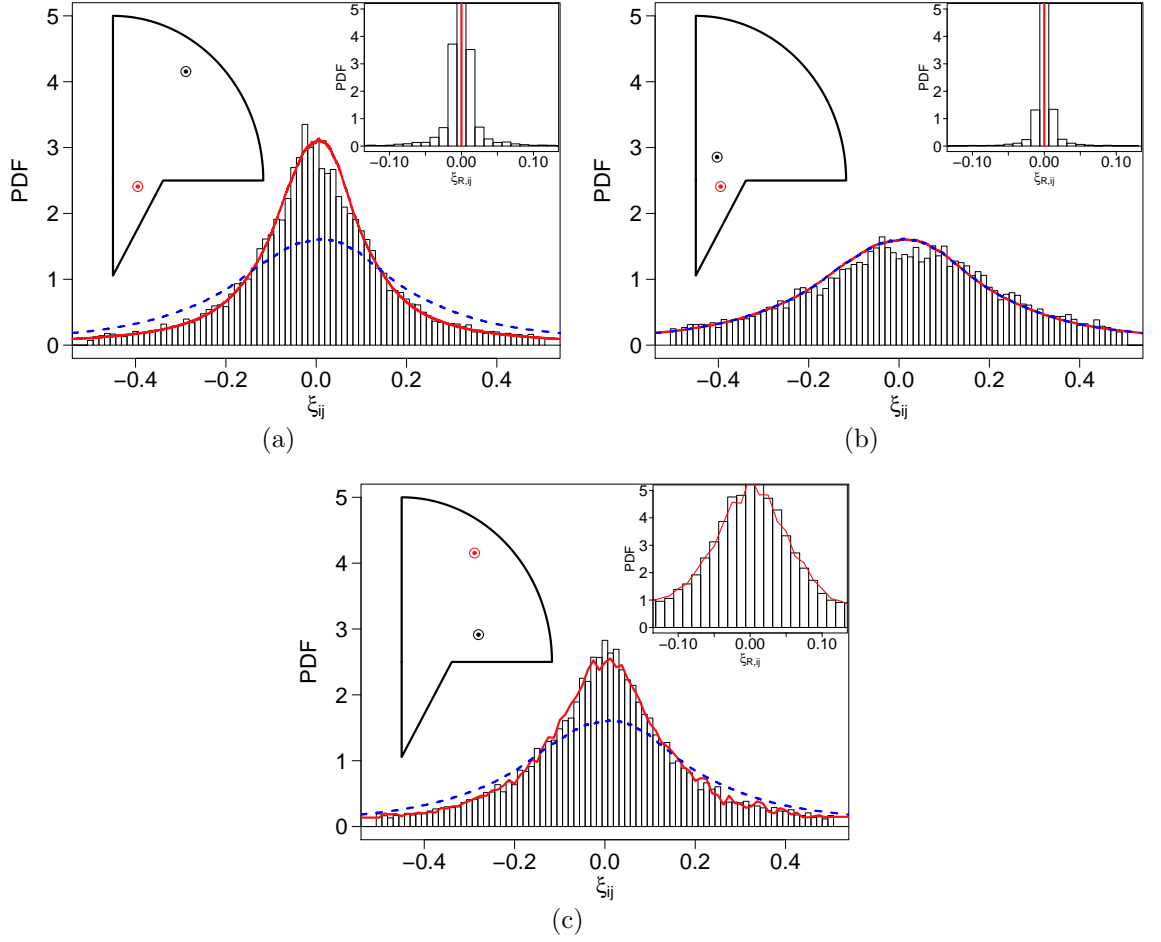


Figure 3.7: Plot of the probability density function of $\xi_{ij} = \xi_{R,ij} + \xi_{C,ij}$ from numerical eigenmode solution (black histogram), our statistical model that treats regular and chaotic contributions separately (red solid curve), and previous statistical model that assumes that all eigenmodes are chaotic (blue dashed curve). The black and red dots are the position of coaxial transmission lines (ports) in case (a) one port in chaotic region and the other in mixed region (b) both pots in chaotic region (c) both ports in mixed region. The insets show the probability density function of the regular contribution, $\xi_{R,ij}$, for numerical eigenmode solutions (black histogram) and for the approximate eigenmode in Eq. (3.32) (red solid curve).

3.4 Discussion

In this chapter, we develop a method for obtaining the short wavelength statistical properties of the impedance matrix of wave systems whose ray equations yield a ‘mixed’ phase space with coexisting chaotic and regular orbits.

In obtaining our results for the mushroom billiard, we assume that the regular eigenmodes are approximately the same as the eigenmodes in a quarter circle cavity. In formulating our theory, we have neglected the possibility that there may be some modes where the regular and chaotic phase space regions are coupled by dynamical tunneling, thus changing both the eigenfunctions and eigenenergies. These mixed modes, whose eigenfunctions show characteristic of both regular and chaotic behavior, can change the wave scattering properties at k^2 near these resonances and this effect can be treated semiclassically for the particular modes under consideration. However, in our formulation, we are not interested in specific k^2 values but rather the pdf for a randomly chosen k^2 values. In our system the number of these chaos/regular mixed modes appears to be relatively small compared with modes that are predominantly confined to either the regular or the chaotic phase space regions. Thus, we expect mixed chaos/regular modes do not make a significant contribution to the mode counting formula in Eq. (3.27), and this expectation is confirmed by the good agreement between our numerical results and theory.

In our model, appropriate to the situation that we numerically tested, we assume that $\phi_n(\vec{x}_i)$ and $\phi_n(\vec{x}_j)$ are independent Gaussian random variables for chaotic wavefunctions, which only applies if ports i and j are far apart, $k|\vec{x}_i - \vec{x}_j| \gg 1$, and

both ports are not close to the cavity boundary. This assumption, however, is not essential: two-point correlations in the random wave model have been previously studied [78, 79] and can be accounted for by regarding $\phi_n(\vec{x}_i)$ and $\phi_n(\vec{x}_j)$ as correlated bivariate Gaussian random variables with a correlation that takes into account direct and indirect ray paths between \vec{x}_i and \vec{x}_j [82].

Chapter 4

Conclusions and Future Work

In chapter ??, we have presented a semiclassical analysis of energy level splitting of symmetric, quantum-dot-type, double-well systems, where the wells are separated by a tunneling barrier. Our analysis quantitatively explains the observed mean splittings and their fluctuations. The mean is found to be independent of the well shape and independent of whether the well orbits are chaotic or not. In contrast, the fluctuation statistics are vastly different when the well orbits are integrable, as compared to when they are chaotic, with the chaotic case yielding much reduced fluctuations when the lateral barrier length is large compared to a wavelength. Future elucidation of such fluctuations might be to employ Bogomolny's semiclassical Green function approach.

In chapter 3, we develop a method for obtaining the short wavelength statistical properties of the lossless impedance matrix of wave systems whose ray equations yield a 'mixed' phase space with coexisting chaotic and regular orbits. We use a specific mixed system, mushroom billiard, which has clearly divided phase space. More generic systems can display infinite hierarchies of KAM island chains encircling other KAM island chains with chaos intermixed. This type of intermingling of chaotic and nonchaotic orbits on all scales is not present in the mushroom billiard where non-smooth shape is designed to yield a clear division between chaotic and

regular phase space region. Our motivation in using the mushroom shape is that the simplicity provided by its clear division of chaotic and regular phase space allows a potentially simpler theory. We hope that our work can serve as a basis for future study applicable to the case of generic phase space structure.

Appendix A

Efficient Way to Calculate Eigenvalues of Gaussian Random Matrices

In each realization of random coupling model (RCM), we need eigenvalues of an $N \times N$ Gaussian random matrix, where $N > 10^3$ in general. For a $N \times N$ dense matrix, general eigensolvers necessitate $O(N^3)$ operations to solve the problem. Moreover, we also need more than 1000 realization to get a good ensemble average, so solving the eigenvalue of random matrices is the bottleneck of the whole calculation. In this appendix, we brief the tridiagonal technique that allow us to calculate these eigenvalues efficiently.

Suppose a symmetric $N \times N$ Gaussian orthogonal random matrix $\mathbf{H} = (\mathbf{A} + \mathbf{A}^T)/2$, where \mathbf{A} is also an $N \times N$ matrix with A_{ij} are i.i.d. $N(0, 1)$, i.e.,

$$\mathbf{H} \sim \begin{bmatrix} N(0, 1) & N(0, 1/2) & \dots & \dots & N(0, 1/2) \\ N(0, 1/2) & \ddots & \ddots & & \vdots \\ \vdots & \ddots & \ddots & \ddots & \vdots \\ \vdots & & \ddots & \ddots & N(0, 1/2) \\ N(0, 1/2) & \dots & \dots & N(0, 1/2) & N(0, 1) \end{bmatrix}_{N \times N}, \quad (\text{A.1})$$

or

$$H_{ij} = H_{ji} \sim \begin{cases} N(0, 1) & \text{for } i = j \\ N(0, 1/2) & \text{for } i \neq j. \end{cases} \quad (\text{A.2})$$

We can tridiagonalize this matrix with the following steps.

For $n = 1$, we define

$$\mathbf{H}^{(1)} = \mathbf{H} \quad (\text{A.3})$$

$$\alpha^{(1)} = -\text{sgn}(H_{2,1}^{(1)}) \sqrt{\sum_{j=2}^N (H_{j,1}^{(1)})^2} \quad (\text{A.4})$$

$$r^{(1)} = \sqrt{\frac{1}{2}(\alpha^{(1)})^2 - H_{2,1}^{(1)}\alpha^{(1)}} \quad (\text{A.5})$$

$$\mathbf{v}^{(1)} = [v_1^{(1)}, v_2^{(1)}, \dots, v_N^{(1)}]^T \quad (\text{A.6})$$

$$\mathbf{P}_{N \times N}^{(1)} = \mathbf{I}_{N \times N} - 2\mathbf{v}^{(1)}(\mathbf{v}^{(1)})^T \quad (\text{A.7})$$

where

$$v_k^{(1)} = \begin{cases} 0 & \text{for } k \leq 1 \\ \frac{H_{k,1}^{(1)} - \alpha^{(1)}}{2r^{(1)}} & \text{for } k = 2 \\ \frac{H_{k,1}^{(1)}}{2r^{(1)}} & \text{for } k \geq 3, \end{cases} \quad (\text{A.8})$$

and it can be shown with some algebra manipulation to prove that $\mathbf{P}^{(1)}$ is symmetric and orthogonal, and thus $\mathbf{P}^{(1)}\mathbf{H}^{(1)}\mathbf{P}^{(1)}$ is an orthogonal transform and we can define

$$\mathbf{H}^{(2)} = \mathbf{P}^{(1)}\mathbf{H}^{(1)}\mathbf{P}^{(1)}. \quad (\text{A.9})$$

For $n = 2, \dots, N-2$, we define

$$\alpha^{(n)} = -\text{sgn}(H_{n+1,n}^{(n)}) \sqrt{\sum_{j=n+1}^N (H_{j,n}^{(n)})^2} \quad (\text{A.10})$$

$$r^{(n)} = \sqrt{\frac{1}{2}(\alpha^{(n)})^2 - H_{n+1,n}^{(n)}\alpha^{(n)}} \quad (\text{A.11})$$

$$\mathbf{v}^{(n)} = [v_1^{(n)}, v_2^{(n)}, \dots, v_N^{(n)}]^T \quad (\text{A.12})$$

$$\mathbf{P}_{N \times N}^{(n)} = \mathbf{I}_{N \times N} - 2\mathbf{v}^{(n)}(\mathbf{v}^{(n)})^T \quad (\text{A.13})$$

where

$$v_k^{(n)} = \begin{cases} 0 & \text{for } k \leq n \\ \frac{H_{k,n}^{(n)} - \alpha^{(n)}}{2r^{(n)}} & \text{for } k = n+1 \\ \frac{H_{k,n}^{(n)}}{2r^{(n)}} & \text{for } k \geq n+2. \end{cases} \quad (\text{A.14})$$

and we can show that $\mathbf{P}^{(n)}$ is symmetric and orthogonal; thus, $\mathbf{P}^{(n)}\mathbf{H}^{(n)}\mathbf{P}^{(n)}$ is an orthogonal transform and we can define

$$\mathbf{H}^{(n+1)} = \mathbf{P}^{(n)}\mathbf{H}^{(n)}\mathbf{P}^{(n)} \quad (\text{A.15})$$

Finally, we reach

$$\mathbf{H}^{(N-1)} = \mathbf{P}^{(N-2)} \dots \mathbf{P}^{(1)} \mathbf{H} \mathbf{P}^{(1)} \dots \mathbf{P}^{(N-2)}, \quad (\text{A.16})$$

which is an orthogonal transform of \mathbf{H} . Thus, the eigenvalues of \mathbf{H} and $\mathbf{H}^{(N-1)}$ should have the same distribution.

Furthermore, it can be shown that

$$\mathbf{H}^{(N-1)} \sim \frac{1}{\sqrt{2}} \begin{bmatrix} N(0, 2) & \chi_{N-1} & 0 & \dots & 0 \\ \chi_{N-1} & N(0, 2) & \chi_{N-2} & \ddots & \vdots \\ 0 & \chi_{N-2} & \ddots & \ddots & 0 \\ \vdots & \ddots & \ddots & N(0, 2) & \chi_1 \\ 0 & \dots & 0 & \chi_1 & N(0, 2) \end{bmatrix}_{N \times N}, \quad (\text{A.17})$$

where χ_n is a Chi-distributed random variable with n degree of freedom.

For a symmetric tridiagonal $N \times N$ sparse matrix, we only need $O(N^2)$ operations to solve the eigenvalue problem, which is $O(N)$ faster than dense matrix, see Fig. A.1.

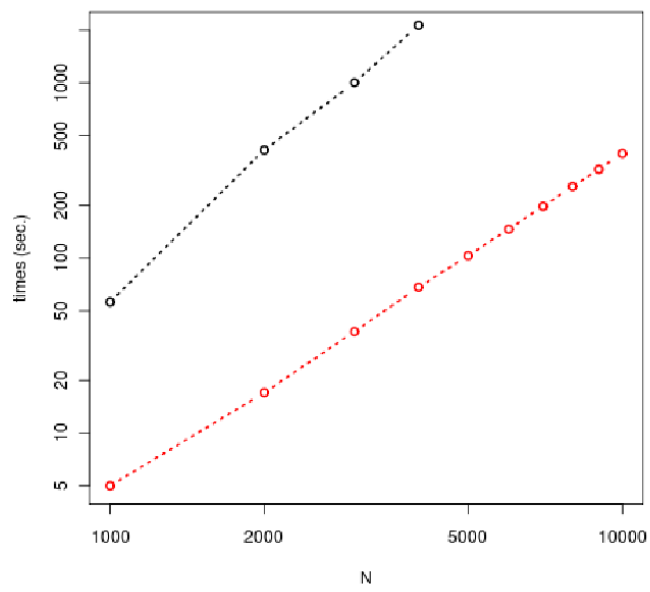


Figure A.1: Comparison between average time required to solve the eigenvalues of a $N \times N$ GOE matrix using (black) Eq.(A.1) and (red) Eq.(A.17) in log-log plot.

Note that, this method apply not only to calculate the eigenvalues of GOE matrices but also GUE and GSE matrices.

$$\mathbf{H}_\beta^{(N-1)} \sim \frac{1}{\sqrt{2}} \begin{bmatrix} N(0,2) & \chi_{\beta(N-1)} & 0 & \dots & 0 \\ \chi_{\beta(N-1)} & N(0,2) & \chi_{\beta(N-2)} & \ddots & \vdots \\ 0 & \chi_{\beta(N-2)} & \ddots & \ddots & 0 \\ \vdots & \ddots & \ddots & N(0,2) & \chi_\beta \\ 0 & \dots & 0 & \chi_\beta & N(0,2) \end{bmatrix}_{N \times N} . \quad (\text{A.18})$$

where $\beta = 1$ for GOE matrices, $\beta = 2$ for GUE matrices and $\beta = 4$ for GSE matrices.

Matlab source code for Eq. (A.18)

```
% off-diagonal term
d0=normrnd(0,sqrt(2),1,N)';

% diagonal term
d1=sqrt(chi2rnd(beta*((N-1):-1:1)))';

% form tri-diagonal matrix
H=spdiags([d1;0],d0,[0;d1],[-1,0,1],N,N)/sqrt(2);

% solve eigenvalue
ks=eig(H);
```

Appendix B

Method of Particular Solutions

In chapter 3, numerical calculation of eigenvalue problems of the two-dimensional Helmholtz equation plays the major role to examine our theoretical prediction. In this appendix, we briefly introduce numerical techniques to solve the two-dimensional Helmholtz equation efficiently and more detail can be found in [63, 73, 71, 83]. Numerical result of two billiards (stadium and mushroom) has been provided. New discover of over counting eigenmodes in previous algorithm has been discussed. More statistical properties of eigenvalues and eigenfunctions will be covered in Appendix C.

B.1 Introduction

Considering $u(\mathbf{x})$ satisfies the Helmholtz equation with Dirichlet boundary condition in a two-dimensional domain Ω

$$(\nabla^2 + k^2)u(\mathbf{x}) = 0 \quad \text{for } \mathbf{x} \in \Omega \quad (\text{B.1})$$

$$u(\mathbf{x}) = 0 \quad \text{for } \mathbf{x} \in \partial\Omega, \quad (\text{B.2})$$

with normalization condition

$$\int_{\Omega} |u|^2 d^2x = 1. \quad (\text{B.3})$$

B.2 Method of Particular Solutions

The idea of method of particular solutions (MPS) is to approximate the eigenfunction with wavenumber k , $u(k; \vec{x})$, by a linear combination of basis function, $\{\phi_1(k; \vec{x}), \phi_2(k; \vec{x}), \dots\}$, which satisfy Eq. (B.1) but not necessary satisfy the boundary condition (B.2), i.e.,

$$u(k; \vec{x}) = \sum_m c_m \phi_m(k; \vec{x}). \quad (\text{B.4})$$

We define boundary tension function and area norm for $u(k; \vec{x})$ as

$$T_B[u] \equiv \oint_{\partial\Omega} |u(k; s)|^2 ds, \quad (\text{B.5})$$

$$T_I[u] \equiv \int_{\Omega} |u(k; \vec{x})|^2 d^2\mathbf{x}. \quad (\text{B.6})$$

If k_n is an eigenvalue of Eqs. (B.1) and (B.2), we can find a nonzero set of coefficient, $\{c_{nm}\}$, such that $T_B[u] = 0$. Moreover, $u(k_n; \vec{x})$ should always satisfies the normalization condition, i.e., $T_I[u] = 1$.

To solve k_n and $\{c_{nm}\}$, we discretize Eqs. (B.5) and (B.6) as

$$\tilde{T}_B[u] \equiv \sum_{b=1, \vec{x}_b \in \partial\Omega}^{M_B} |u(\vec{x}_b)|^2 \Delta s_b, \quad (\text{B.7})$$

$$\tilde{T}_I[u] \equiv \sum_{i=1, \vec{x}_i \in \Omega}^{M_I} |u(\vec{x}_i)|^2 \Delta \sigma_i. \quad (\text{B.8})$$

For simplicity, we choose $\Delta s_b = \Delta s$ for all s_b and $\Delta \sigma_i = \Delta \sigma$ for all σ_i . Finding zero of $\tilde{T}_B[u]$ usually reaches a trivial solution, $c_{mn} = 0$, for all m . To avoid this undesired solution, we try to find zeros of $\tilde{T}_B[u]/\tilde{T}_I[u]$; however, we still cannot solve $\{c_{nm}\}$, since there are infinity terms of $\{c_{nm}\}$, so we truncate the infinite sum in

Eq. (B.4) by a finite sum

$$u(k_n; \vec{x}) \approx \sum_m^M c_{nm} \phi_m(k_n; \vec{x}). \quad (\text{B.9})$$

Instead of finding zeros of $\tilde{T}_B[u]/\tilde{T}_I[u]$, we look for local minimums of $\tilde{T}_B[u]/\tilde{T}_I[u]$.

We define a $M_B \times M$ matrix, $\mathbf{A}_B(k)$, and a $M_I \times M$ matrix, $\mathbf{A}_I(k)$, and their matrix elements are

$$A_{B,bm} = \phi_m(\vec{x}_b), \quad \text{for } \vec{x}_b \in \partial\Omega, \quad b = 1, \dots, M_B \quad (\text{B.10})$$

$$A_{I,im} = \phi_m(\vec{x}_i), \quad \text{for } \vec{x}_i \in \Omega, \quad i = 1, \dots, M_I \quad (\text{B.11})$$

Thus, finding local minimums of $\tilde{T}_B[u]/\tilde{T}_I[u]$ is equivalent to finding local minimum of

$$t(k; \mathbf{c}) \equiv \frac{\tilde{T}_B[u]}{\tilde{T}_I[u]} = \frac{|\mathbf{A}_B(k)\mathbf{c}|^2}{|\mathbf{A}_I(k)\mathbf{c}|^2}, \quad (\text{B.12})$$

where $\mathbf{c} = [c_1, \dots, c_M]^T$, $|\cdot|$ is the Euclidean norm, and this problem can be solved by the general singular value decomposition (GSVD).

Assuming $\mathbf{A} \in \Re^{n \times p}$ and $\mathbf{B} \in \Re^{m \times p}$ and $n \geq p$. There exist orthogonal matrices $\mathbf{U} \in \Re^{n \times n}$ and $\mathbf{W} \in \Re^{m \times m}$ and an invertible matrix $\mathbf{X} \in \Re^{p \times p}$ such that

$$\mathbf{A} = \mathbf{UCX}^{-1}, \quad \mathbf{B} = \mathbf{WSX}^{-1},$$

where $\mathbf{C} \in \Re^{n \times p}$ and $\mathbf{S} \in \Re^{m \times p}$ are diagonal matrices with $0 \leq c_1 \leq \dots \leq c_p \leq 1$ and $0 \leq s_j \leq 1$ for $j = 1, \dots, \min\{m, p\}$ with $s_j^2 + c_j^2 = 1$ and $c_j = 1$ for $j > \min\{m, p\}$, i.e., $s_j = 0$ for $j > \min\{m, p\}$. The values $\sigma_j = c_j/s_j$ are the generalized singular values of \mathbf{A} and \mathbf{B} . Define $\mathbf{x}_i = [X_{1i}, \dots, X_{pi}]^T$, we have

$$\begin{aligned} |\mathbf{Ax}_i|^2 &= c_i^2 \\ |\mathbf{Bx}_i|^2 &= s_i^2. \end{aligned} \quad (\text{B.13})$$

Applying the GSVD to our problem, we assume that $\mathbf{A} = \mathbf{A}_B(k)$ and $\mathbf{B} = \mathbf{A}_I(k)$ and choose number of boundary discrete point greater than basis. We do not describe the procedure of GSVD here, but in MATLAB, there is a built-in `gsvd()` function that allow us to perform the GSVD easily. At each k , we can find out the minimal singular value, say $\sigma_1(k)$; scanning over k , we can find out at k_n , $\sigma_1(k_n)$ is the local minimal. From Eq. (B.13), we know the corresponding $\mathbf{c}_n = \mathbf{x}_1(k_n)$.

The method of particular solutions can solve the eigenvalue problem precisely by scanning over k very carefully, but slow down the performance; furthermore, this method easily neglects one of two eigenmodes whose eigenvalues are close each other. In practical, we only use this method to find out the first few eigenmodes.

B.3 Scaling Method for MPS

Given a wavefunction $\psi(k; \vec{r})$, we can define its scaling function near a given wave number, k_0 , as

$$\psi(k; \vec{r}) \equiv \psi\left(\frac{k}{k_0}r\right), \quad (\text{B.14})$$

the first derivative over k near k_0 is

$$\frac{\partial}{\partial k}\psi(k; \vec{r})|_{k=k_0} = \frac{1}{k_0} \frac{\partial}{\partial \alpha}\psi(\alpha \vec{r})\Big|_{\alpha=1} = \frac{1}{k_0} \vec{r} \cdot \nabla \psi(\alpha \vec{r}), \quad (\text{B.15})$$

and the Taylor expansion for the wavefunction can be written down as

$$\psi(k_0 + \delta; \vec{r}) = \left[1 + \frac{\delta}{k_0}(\vec{r} \cdot \nabla) + \frac{1}{2} \frac{\delta^2}{k_0^2}(\vec{r} \cdot \nabla)^2 + O(\delta^3)\right] \psi(\vec{r}). \quad (\text{B.16})$$

For $\vec{s} \in \partial\Omega$, since $\nabla = \hat{\mathbf{n}}\partial_n + \hat{\mathbf{t}}\partial_t$, where $\hat{\mathbf{t}}$ and $\hat{\mathbf{n}}$ are tangential and outgoing normal direction at boundary, see Fig. B.3(a), we can write down the scaling function for

an exact eigenfunction, $\psi_\mu(k_\mu, \vec{r})$, with $(\nabla^2 + k_\mu^2)\psi_\mu = 0$ and Dirichlet boundary condition, at $k = k_\mu + \delta$ as

$$\psi_\mu(k_\mu + \delta; \vec{s}) = \left[\frac{\delta}{k_\mu} r_n \partial_n + \frac{\delta^2}{k_\mu^2} r_n r_t \partial_n \partial_t + \frac{\delta^2}{k_\mu^2} \frac{\alpha}{2} (r_t^2 - r_n^2) \partial_n \right] \psi_\mu(\vec{s}) + O(\delta^3), \quad (\text{B.17})$$

where α is the inverse of radius of curvature at \vec{s} .

For a general sum of scaling eigenfunction, i.e.,

$$\psi(k; \vec{r}) = \sum_\mu \tilde{x}_\mu \psi_\mu(k; \vec{r}), \quad (\text{B.18})$$

the tension is

$$f(k) = \oint_{\partial D} d\vec{s} w(\vec{s}) |\psi(k; \vec{s})|^2. \quad (\text{B.19})$$

where $w(\vec{s}) = 1/r_n$ is a boundary weighting function. The tension can be expressed as a quadratic form

$$f(k) = \tilde{\mathbf{x}}^T \tilde{\mathbf{F}}(k) \tilde{\mathbf{x}}, \quad (\text{B.20})$$

where the matrix element of $\tilde{\mathbf{F}}(k)$ is

$$\begin{aligned} \tilde{F}_{\mu\nu}(k) &= \oint_{\partial D} d\vec{s} w(\vec{s}) \psi_\mu(k, \vec{s}) \psi_\nu(k, \vec{s}) \\ &= \frac{\delta_\mu}{k_\mu} \frac{\delta_\nu}{k_\nu} \oint_{\partial D} d\vec{s} w(\vec{s}) r_n^2 (\partial_n \psi_\mu(k, \vec{s})) (\partial_n \psi_\nu(k, \vec{s})) + O(\delta^3) \\ &= 2\delta_\mu \delta_\nu M_{\mu\nu}(k) + O(\delta^3) \end{aligned} \quad (\text{B.21})$$

and

$$M_{\mu\nu}(k) = \frac{1}{2k^2} \oint_{\partial D} d\vec{s} w(\vec{s}) r_n^2 (\partial_n \psi_\mu(k, \vec{s})) (\partial_n \psi_\nu(k, \vec{s})) \quad (\text{B.22})$$

where we assume that $k_\mu \cong k_\nu \cong k$.

It has been proven that [83]

$$M_{\mu\nu}(k) \approx \delta_{\mu\nu}. \quad (\text{B.23})$$

Combining with Eq. (B.21) and using the fact that $\partial_k \delta = 1$ [since $k = k_\mu + \delta$], we get

$$\frac{d\tilde{F}_{\mu\nu}}{dk}(k) = 2(\delta_\mu + \delta_\nu)M_{\mu\nu} + O(\delta^2). \quad (\text{B.24})$$

Now, we want to express the scaling eigenfunction as a linear combination of basis function, i.e.,

$$\psi_\mu(\vec{s}) = \sum_i Y_{i\mu} \phi_i(\vec{s}), \quad (\text{B.25})$$

and we have

$$\tilde{\mathbf{F}}(k) = \mathbf{Y}^T \mathbf{F}(k) \mathbf{Y}, \quad (\text{B.26})$$

$$\frac{\partial \tilde{\mathbf{F}}}{\partial k}(k) = \mathbf{Y}^T \frac{\partial \mathbf{F}}{\partial k}(k) \mathbf{Y}, \quad (\text{B.27})$$

where the matrix element of $\mathbf{F}(k)$ and $\partial \mathbf{F}(k)/\partial k$ are

$$F_{ij}(k) = \oint_{\partial D} d\vec{s} \frac{1}{r_n} \phi_i(k; \vec{s}) \phi_j(k; \vec{s}) \quad (\text{B.28})$$

$$\frac{dF_{ij}}{dk}(k) = \frac{1}{k} \oint_{\partial D} d\vec{s} \frac{1}{r_n} \phi_i(k; \vec{s}) \vec{s} \cdot \nabla \phi_j(k; \vec{s}) + \text{transpose}. \quad (\text{B.29})$$

Combining Eqs. (B.21), (B.24), (B.23), (B.26), (B.27), (B.28) and (B.29), we can solve the following generalized eigenvalue problem

$$\left(\frac{d\mathbf{F}}{dk} - \lambda_\mu \mathbf{F} \right) \mathbf{y}_\mu = 0 \quad (\text{B.30})$$

where $\lambda_\mu = \frac{2}{\delta_\mu}$ is the generalized eigenvalues such that $k_\mu = k - \delta_\mu$ and $\mathbf{y}_\mu = [Y_{1\mu}, \dots, Y_{M\mu}]^T$ is the generalized eigenvectors such that $\psi_\mu(\vec{r}) = \sum_{i=1}^M Y_{i\mu} \phi_i(\vec{r})$.

The advantage of scaling method for MPS is that at each time we solve the generalized eigenvalue problem of \mathbf{F} and $d\mathbf{F}/dk$, Eq. (B.30), we would be able to solve all eigenmodes near k . Using proper number of basis function and discrete boundary

point (see Refs[add something]), we would be find out all eigenmodes, $k_\mu \in [k - dk, k + dk]$ by solving the generalized eigenvalue problem once. To solve all eigenvalue $k_\mu \leq k_{Max}$, we only need to choose proper dk and solve N generalized eigenvalue problems on the following N interval, $[0, 2dk], (2dk, 4dk], \dots, (2(N - 1)dk, 2Ndk]$, where $2(N - 1)dk < k_{Max} \leq 2Ndk$.

B.4 Over Counting Eigenmodes

The scaling method for MPS allows us to find out all eigenmodes of two-dimensional Helmholtz equation with Dirichlet boundary condition. Actually, it find out more eigenmodes than the Weyl's formula prediction. To explain this over counting phenomena, we focus on all eigenmodes we solved in the two consecutive interval, $(k - dk, k + dk]$ and $(k + dk, k + 3dk]$, say $k - dk < \dots < k_{n-1} < k_n \leq k + dk$ and $k + dk < k_{n+1} < k_{n+2} < \dots \leq k + 3dk$. Since the numerical solution is not absolutely precise to the exact eigenvalue, it is possible that k_n and k_{n+1} actually represent the same eigenmodes. To eliminate these over counting eigenmodes, we can solve the generalized eigenvalue problem in $(k, k + 2dk]$ to verify whether there are one or two eigenmodes near $k + dk$ (see Fig. B.1).

We compare the difference mode counting function from numerically calculated eigenmodes of stadium billiard, see Fig. B.3(a), and the Weyl's formula (1.8) in Fig. B.2, and mode counting function excluding the over counting eigenmodes agrees with Weyl's formula better.

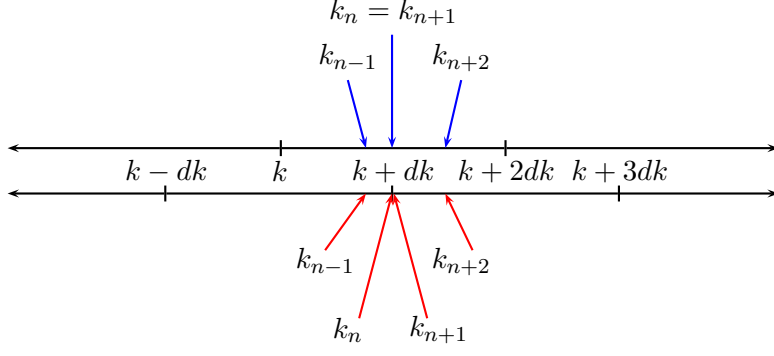


Figure B.1: Illustration of over counting eigenmodes.

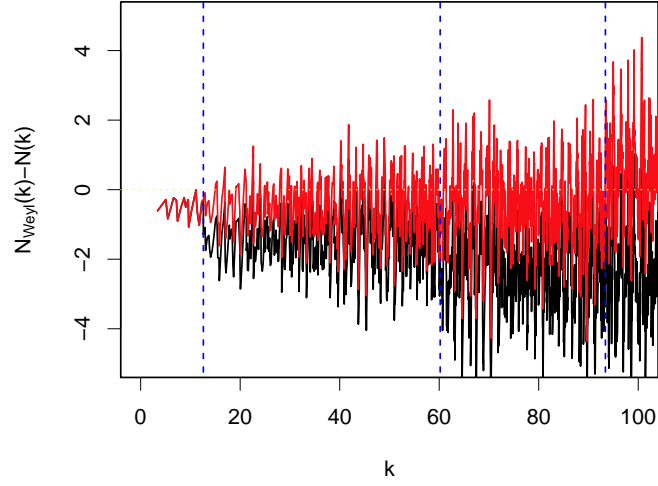


Figure B.2: Difference between mode counting function from numerical calculated eigenmodes (black solid curve) including over counting eigenmodes (red solid curve) excluding over counting eigenmodes and Weyl's formula prediction. The vertical blue dashed line label the location of over counting eigenmodes.

B.5 Choice of Basis

The most natural choice of basis is motivated by the random plane wave hypothesis. We use the stadium billiard as our example, see Fig. B.3(a). We can

choose $\mathbf{r}_0 \in \Omega$, and

$$\phi_n(\vec{r}) = \begin{cases} \cos [\mathbf{k}_m \cdot (\mathbf{r} - \mathbf{r}_0)] & \text{for } n = 2m - 1 \\ \sin [\mathbf{k}_m \cdot (\mathbf{r} - \mathbf{r}_0)] & \text{for } n = 2m \end{cases} \quad (\text{B.31})$$

where $\mathbf{k}_m = k \cos\left(\frac{m\pi}{M}\right) \hat{\mathbf{x}} + k \sin\left(\frac{m\pi}{M}\right) \hat{\mathbf{y}}$, $n = 1, \dots, 2M$. Some eigenfunctions are plotted in Figs. B.4 and B.5 .

In case that Ω has a corner, like the mushroom billiard(B.3(b)), we can choose Fourier Bessel basis function

$$\phi_n(\vec{r}) = J_{\alpha n}(kr) \sin(\alpha n \theta), \quad (\text{B.32})$$

where $J_{\alpha n}$ is the Bessel function of the first kind with order αn . In our numerical work, we choose $\alpha = 3/4$. Some eigenfunctions are plotted in Figs. B.6 and B.7 .

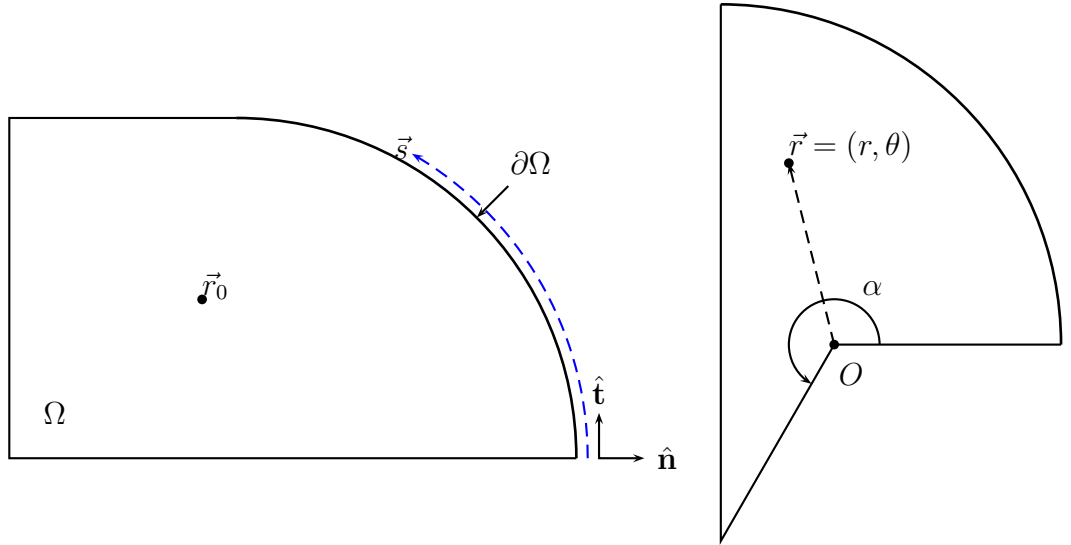


Figure B.3: (a) Stadium billiard and (b) Mushroom billiard.

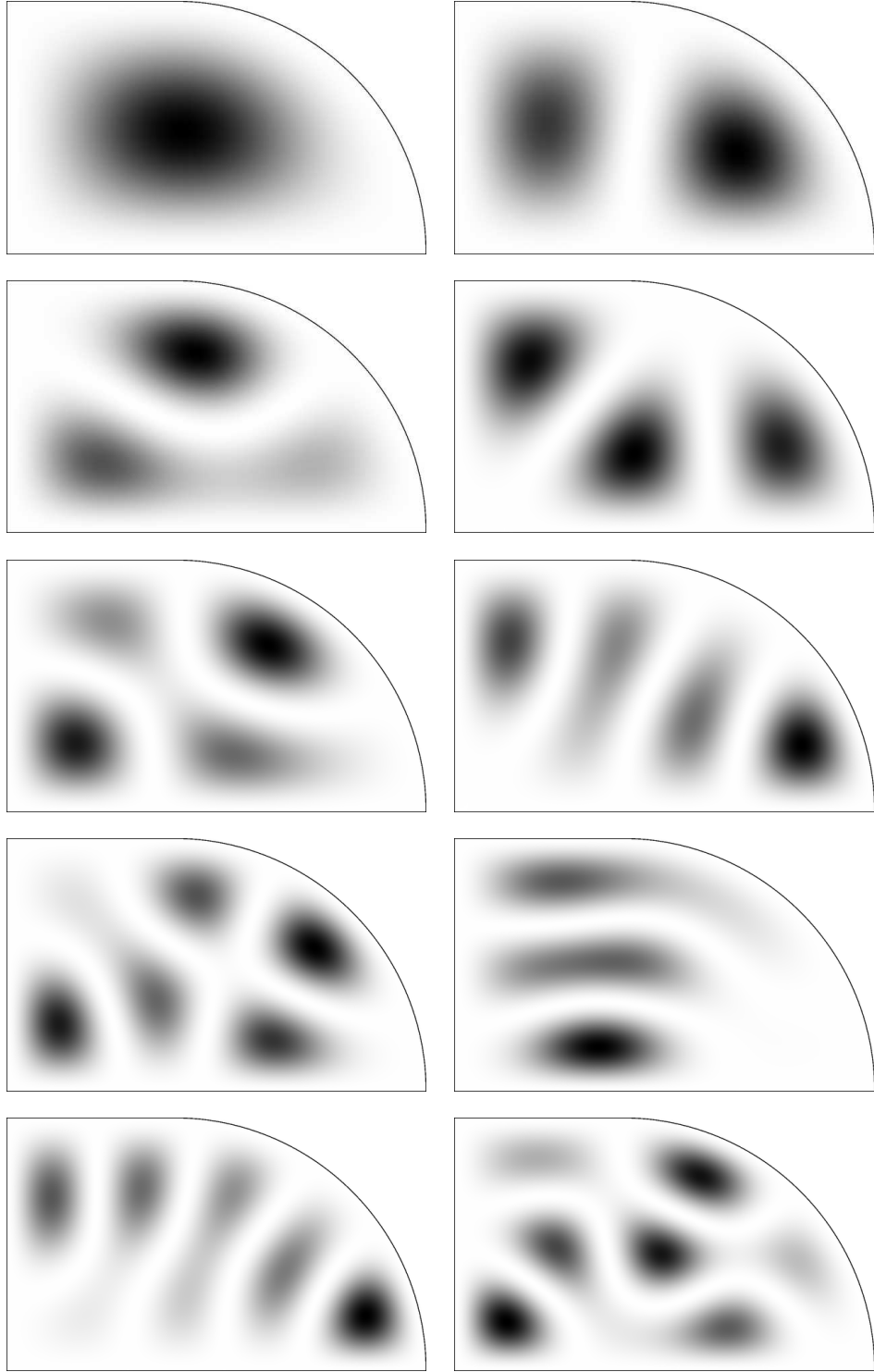


Figure B.4: The first 10 engenmodes of the stadium billiard, shown as density plots.

Eigenvalue increases rightwards from the top left.

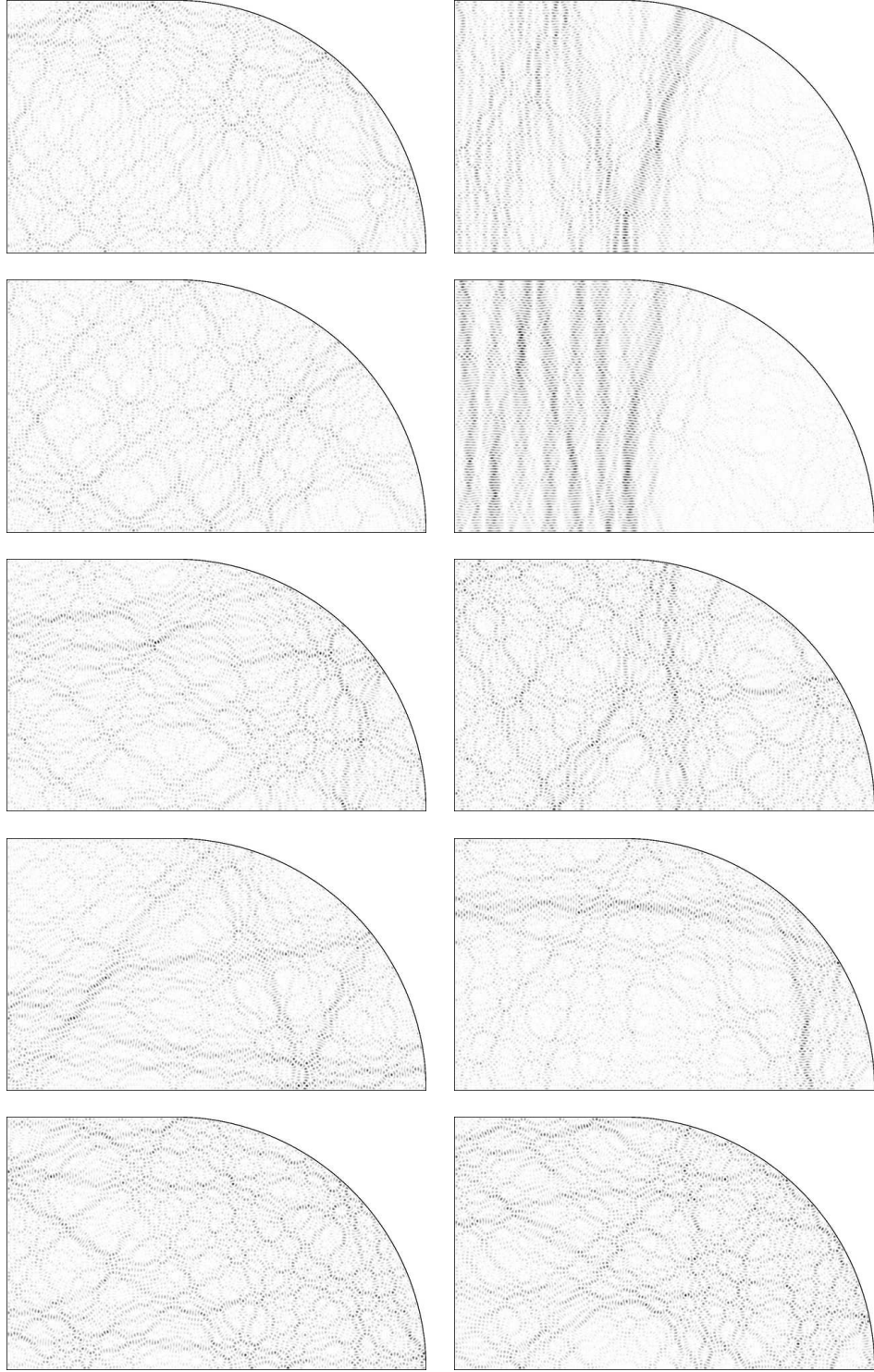


Figure B.5: Density plot of the 10 engenmodes of the stadium billiard whose eigenenergies $k_n^2 \in (39139, 39191)$, at $n \approx 10000$.

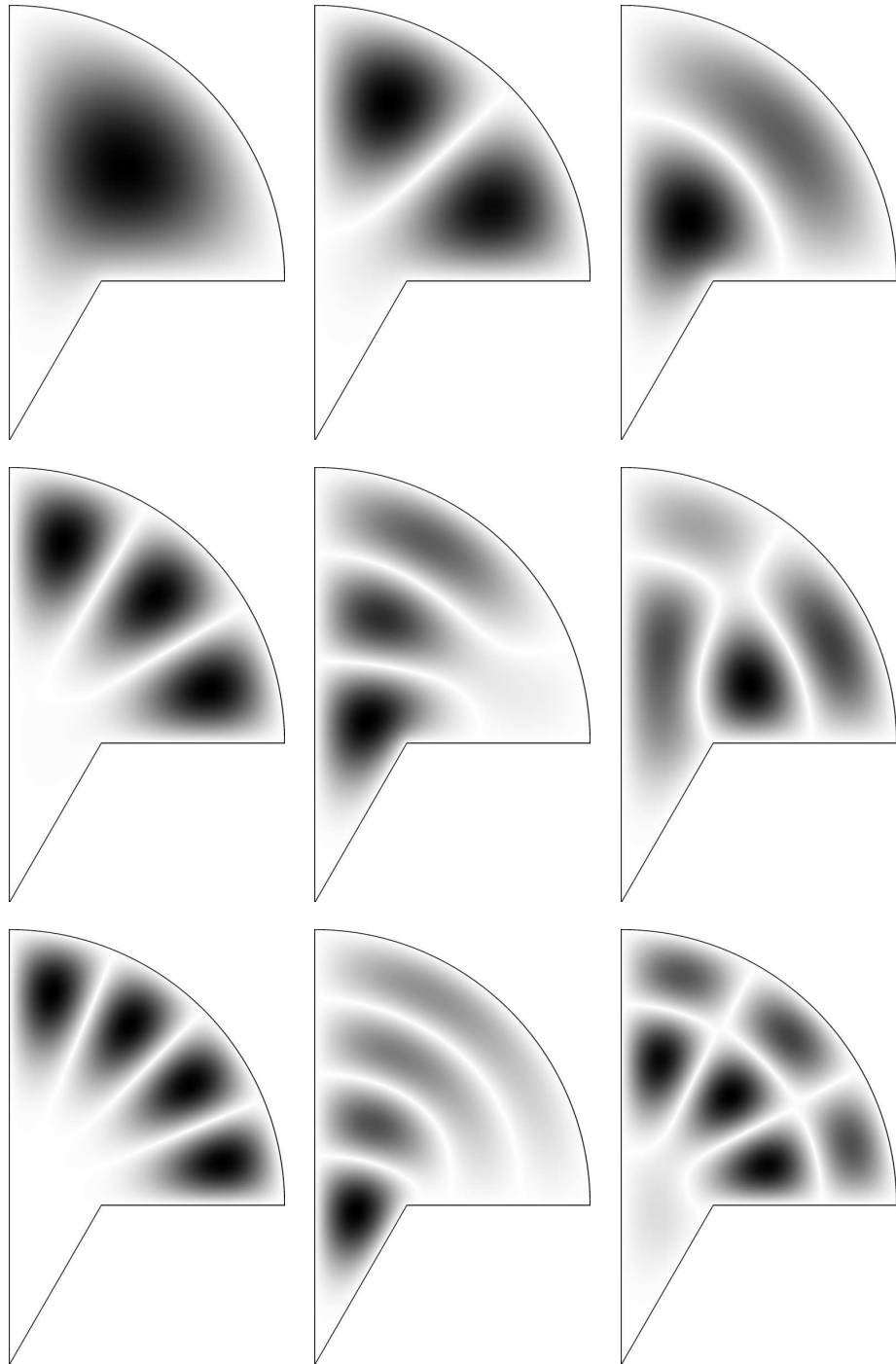


Figure B.6: The first 9 engenmodes of the mushroom billiard, shown as density plots. Eigenvalue increases rightwards from the top left.

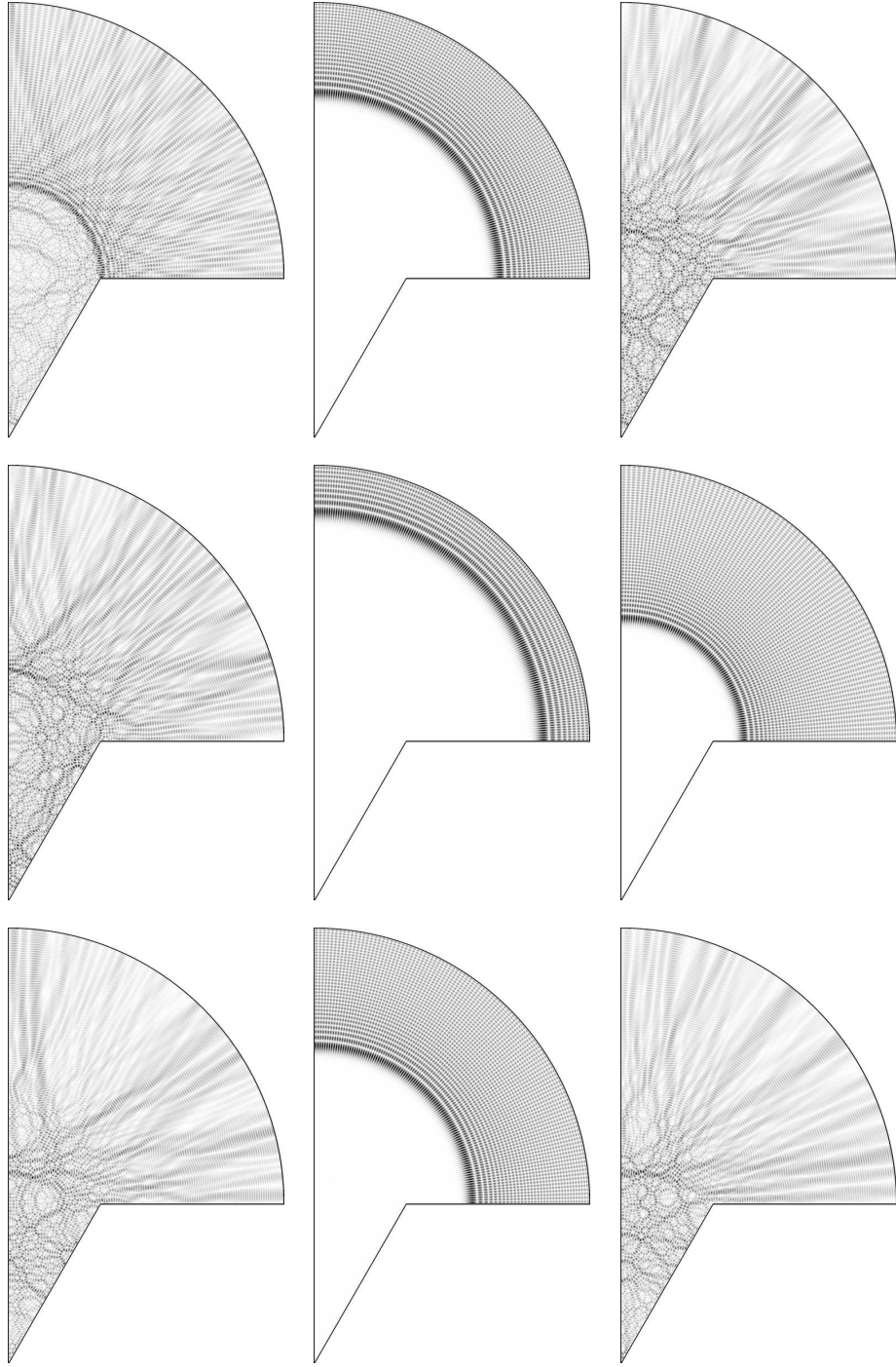


Figure B.7: Density plot of the 9 engenmodes of the mushroom billiard whose eigenenergies $k_n^2 \in (64234, 64285)$, at $n \approx 10000$.

Appendix C

Statistics of Eigenmode

In this section, we compare the numerically calculated wavefunction amplitude with the prediction of random matrix theory and random plane wave hypothesis. We use the numerically calculated eigenmodes of stadium and mushroom billiard in Appendix B as our example of chaotic and mixed system.

C.1 Chaotic Billiard

We solve the first 23,072 eigenmodes ($k_n \leq 300$) of the stadium billiard, see Fig. B.3(a), use Eq. (1.11) to normalize the spacing between two consecutive eigenvalue and get good agreement with the random matrix theory (1.14), see Fig. C.1.

We also compared the eigenfunction amplitude at different position, $\phi(\mathbf{x})$, in the billiard and compare the probability density function of $\phi(\mathbf{x})$ with Eq. (1.18) and get good agreement, see Fig. C.2.

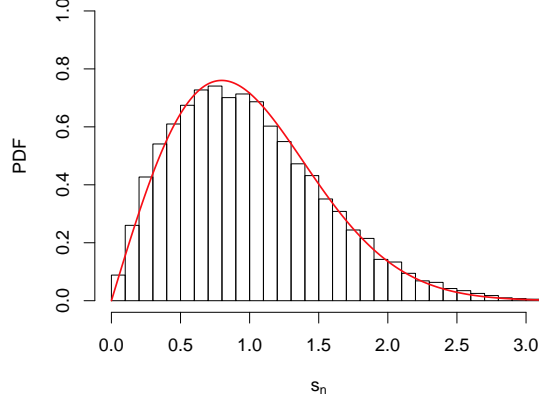


Figure C.1: Comparison between the probability density function of normalized nearest neighbor eigenvalue spacings of (black histogram) stadium billiard and (red curve) Wigner GOE distribution.

C.2 Mixed Billiard

We solve the first 39,114 eigenmodes ($k_n \leq 500$) of the mushroom billiard, see Fig. B.3(b), and use the outward normal derivative of eigenfunction at the boundary to classify whether eigenmodes are either regular (ϕ_r, k_r^2) or chaotic (ϕ_c, k_c^2), see Sec. 3.3. In Fig. C.3, we use Eq. (1.11) to normalize the spacing between two consecutive (chaotic/regular/mixed) eigenvalue and get good agreement with the random matrix theory (1.14), Poisson distribution (1.16), and Berry-Robnik distribution (C.1),

$$P_{BR}(\rho_r, \rho_c; s) = \frac{d^2}{ds^2} \left[\exp(-\rho_r s) \operatorname{erfc} \left(\frac{\sqrt{\pi}}{2} \rho_c s \right) \right], \quad (\text{C.1})$$

where

$$\operatorname{erfc}(x) = \frac{2}{\pi} \int_x^\infty \exp(-t^2) dt. \quad (\text{C.2})$$

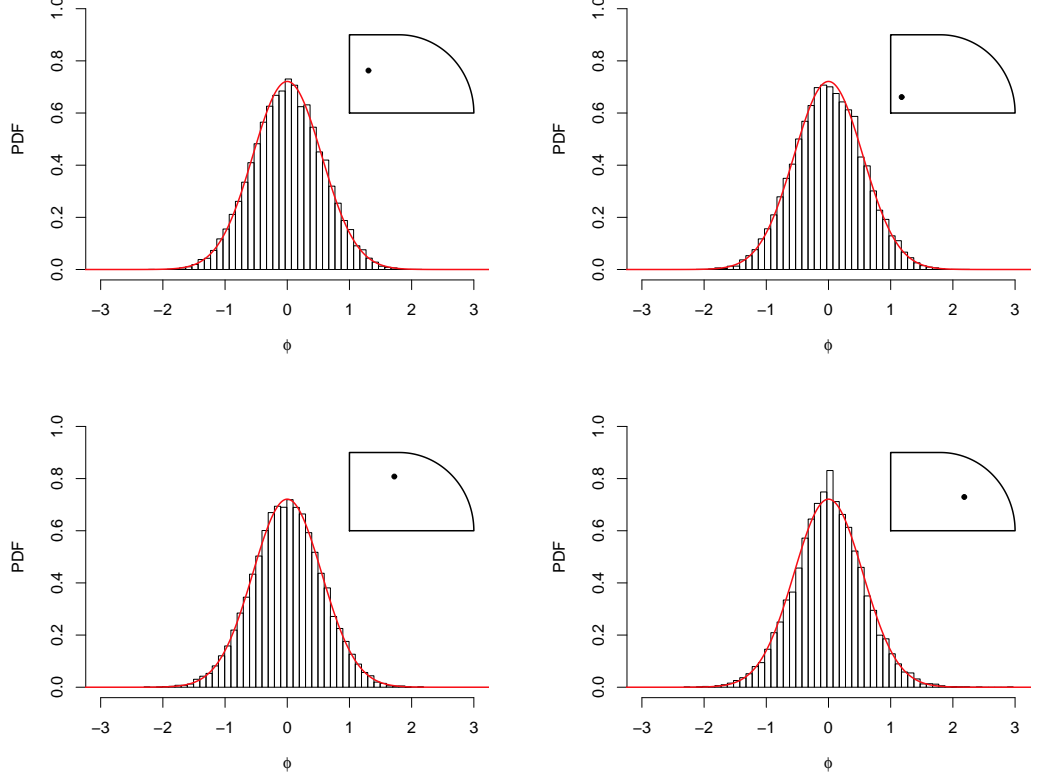


Figure C.2: Comparison between (black histogram) the probability density function of the first 23,072 eigenfunction amplitudes of the stadium billiard at different position (see inset) and (red curve) Gaussian distribution.

Note that in Berry-Robnik distribution (C.1), it requires the information of phase space volume ratio of regular and chaotic region, i.e., ρ_r and ρ_c . Using Eqs. (3.28) and (3.37), we get $\rho_c = A_c/A$ and $\rho_r = 1 - \rho_c$, where A is the total area of the mushroom cavity.

We also compared the chaotic eigenfunction amplitude at different position, $\phi_C(\mathbf{x})$, in the billiard and compare the probability density function of $\phi_C(\mathbf{x})$ with Eqs. (3.30) and (3.31) and get good agreement, see Fig. C.4.

There is no universal theorem to predict the probability density function of

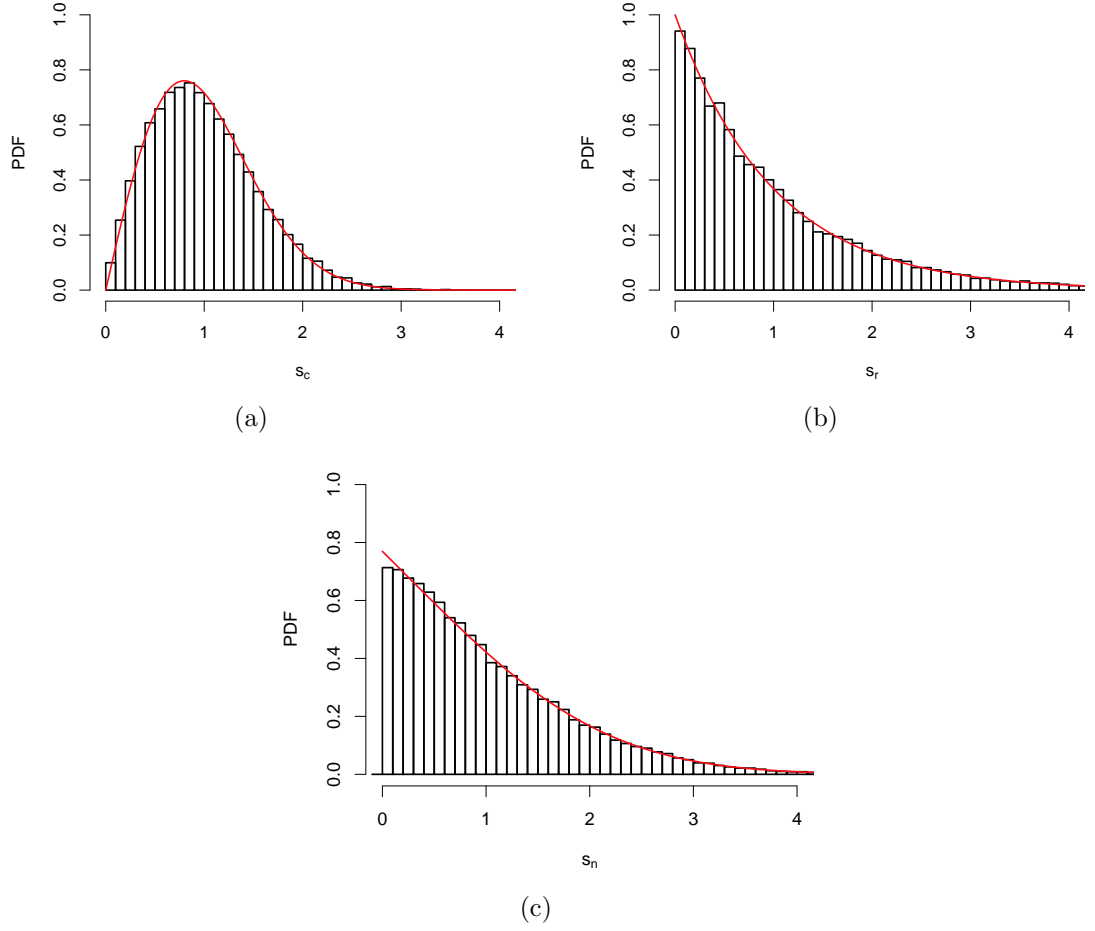


Figure C.3: (a) Comparison between the probability density function of normalized nearest neighbor chaotic eigenvalue spacings of (black histogram) mushroom billiard and (red curve) GOE matrix. (b) Comparison between (black histogram) the probability density function of normalized nearest neighbor regular eigenvalue spacings of mushroom billiard and (red curve) Poisson distribution. (a) Comparison between (black histogram) the probability density function of normalized nearest neighbor eigenvalue spacings of mushroom billiard and (red curve) Berry-Robnik distribution.

$\phi_R(\mathbf{x})$ over a wide range of k^2 , see Fig. C.5.

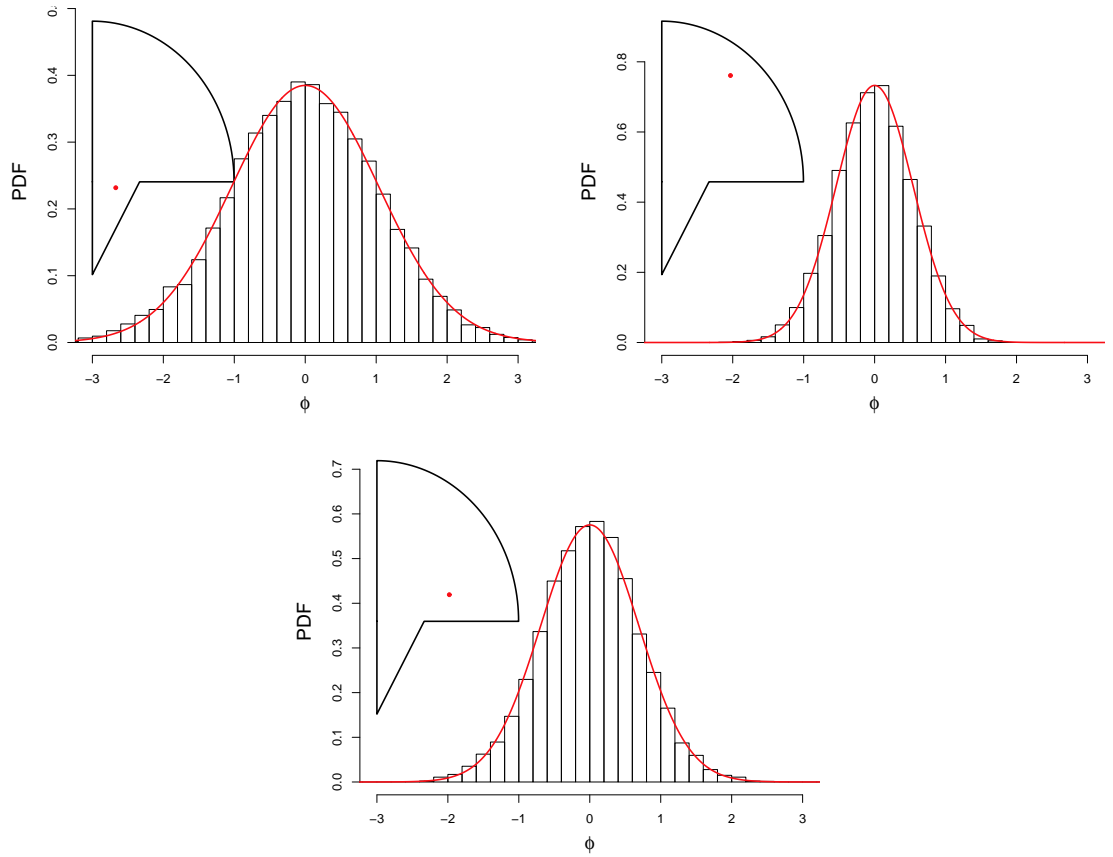


Figure C.4: Comparison between (black histogram) the probability density function of the first 19,198 chaotic eigenfunction amplitudes of the mushroom billiard at different position (see inset) and (red curve) Gaussian distribution.

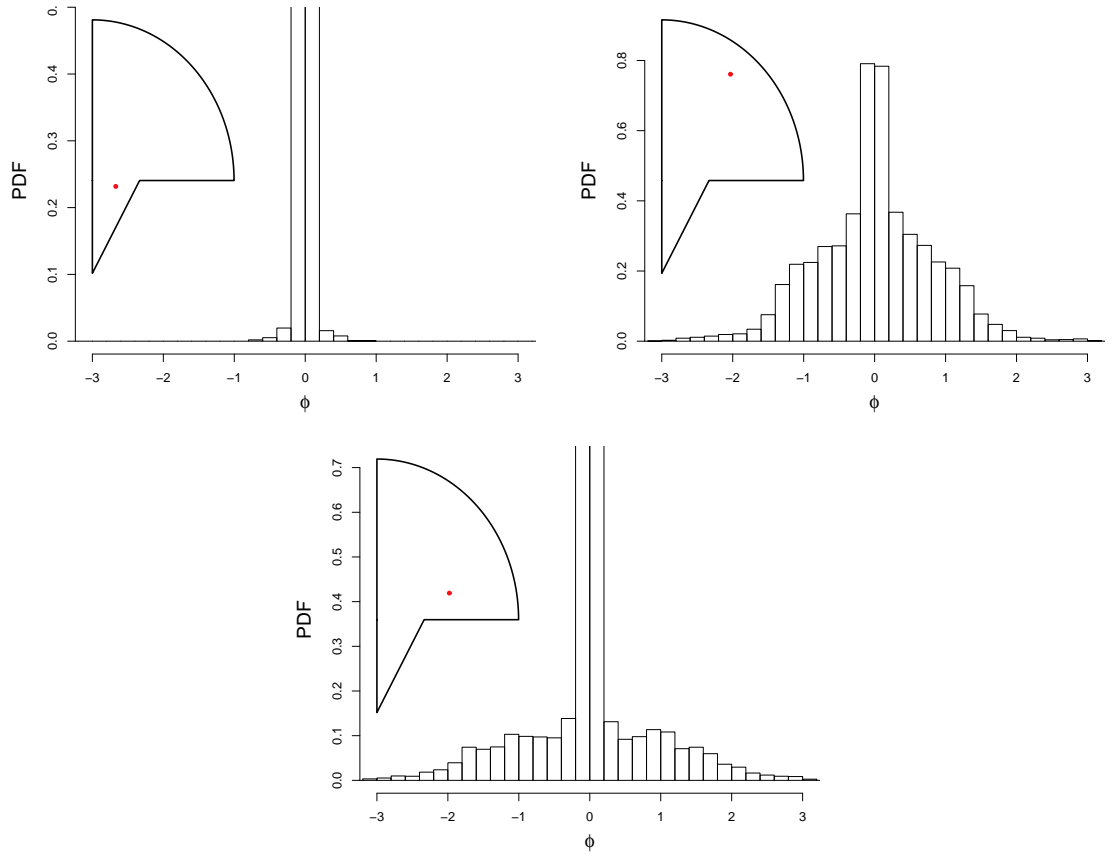


Figure C.5: The probability density function of the first 19,916 regular eigenfunction amplitudes of the mushroom billiard at different position (see inset).

Appendix D

Random Wave Model with Boundary Conditions

Given a two-dimensional chaotic region Ω with area A , we assume that $\mathbf{r}_i, \mathbf{r}_j \in \Omega$ and $|\mathbf{r}_i - \mathbf{r}_j|$ much less than the distance of \mathbf{r}_i or \mathbf{r}_j to the boundary $\partial\Omega$. From Berry's conjecture, the eigenfunction amplitudes at \mathbf{r}_i and \mathbf{r}_j , $(\phi(\mathbf{r}_i), \phi(\mathbf{r}_j)) \equiv (\phi_i, \phi_j)$, are normal distributed, and the correlation between ϕ_i, ϕ_j is $J_0(k|\mathbf{r}_i - \mathbf{r}_j|)$. Thus, (ϕ_i, ϕ_j) can be described as a bivariate Gaussian distribution

$$p(\phi_i, \phi_j) = \frac{1}{2\pi\sigma^2\sqrt{1-c_{ij}^2}} \exp\left[-\frac{\phi_i^2 + \phi_j^2}{2\sigma^2(1-\rho^2)}\right], \quad (\text{D.1})$$

where $\sigma^2 = 1/A$ and

$$c_{ij} \equiv C(\mathbf{r}_i, \mathbf{r}_j) = \frac{\langle \phi_i \phi_j \rangle}{\sqrt{\langle \phi_j^2 \rangle \langle \phi_i^2 \rangle}}, \quad (\text{D.2})$$

is the two-point correlation function in closed system.

We are able to remove the distance and boundary constraints in Berry's conjecture by using the semiclassical Green's function for d-dimensional space,

$$G_{scl}(\mathbf{r}_i, \mathbf{r}_j; k) = \frac{1}{i\hbar(2\pi i\hbar)^{(d-1)/2}} \sum_{paths} |D_p|^{1/2} e^{iS_p/\hbar - i\nu_p\pi/2} \quad (\text{D.3})$$

where the sum is over all classical paths connecting between \mathbf{r}_i and \mathbf{r}_j , ν_p is number of classical focal points along the path,

$$S_p = \int_{\mathbf{r}_i}^{\mathbf{r}_j} \mathbf{p} \cdot d\mathbf{q} \quad (\text{D.4})$$

is the actions of the path and

$$D_p = \det \begin{pmatrix} \frac{\partial^2 n S_p}{\partial \mathbf{r}_j \partial \mathbf{r}_i} & \frac{\partial^2 n S_p}{\partial E \partial \mathbf{r}_i} \\ \frac{\partial^2 n S_p}{\partial \mathbf{r}_j \partial E} & \frac{\partial^2 n S_p}{\partial E^2} \end{pmatrix} \quad (\text{D.5})$$

is the determinant of the second derivative matrix of S_p . Then the two-point correlation function at a given wavenumber k is

$$\begin{aligned} C(\mathbf{r}_i, \mathbf{r}_j; k) &= \frac{1}{2\pi i \bar{\rho}(k^2)} [G_{scl}(\mathbf{r}_j, \mathbf{r}_i; k)^* - G_{scl}(\mathbf{r}_j, \mathbf{r}_i; k)] \\ &= \frac{2}{\bar{\rho}(k^2)(2\pi\hbar)^{(d+1)/2}} \sum_{paths} |D_p|^{1/2} \cos [S_p/\hbar - (2\nu_p + d - 1)\pi/4]. \end{aligned} \quad (\text{D.6})$$

Using the asymptotic form of the Bessel function of the first kind,

$$J_0(z) \approx \sqrt{\frac{2}{\pi z}} \cos \left(z - \frac{\pi}{4} \right), \quad (\text{D.7})$$

we get

$$C_0(\mathbf{r}_i, \mathbf{r}_j, k) = \frac{1}{A} J_0(k|\mathbf{r}_i - \mathbf{r}_j|), \quad (\text{D.8})$$

which is identical with Berry's original result.

Taking $\mathbf{r}_i = \mathbf{r}_j$, we get

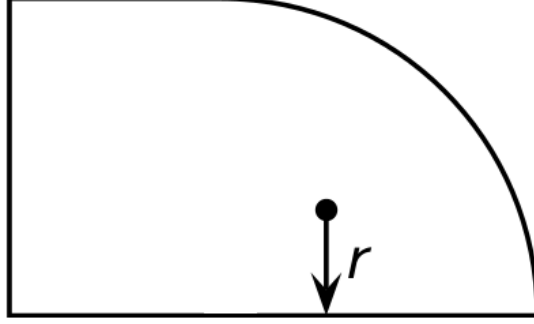
$$\sigma^2(\mathbf{r}_i; k) = C(\mathbf{r}_i, \mathbf{r}_i, k) = \frac{1}{A} [1 + \text{boundary term}(k)], \quad (\text{D.9})$$

which is depend on wavenumber k and position \mathbf{r}_i . To examine this boundary effect,

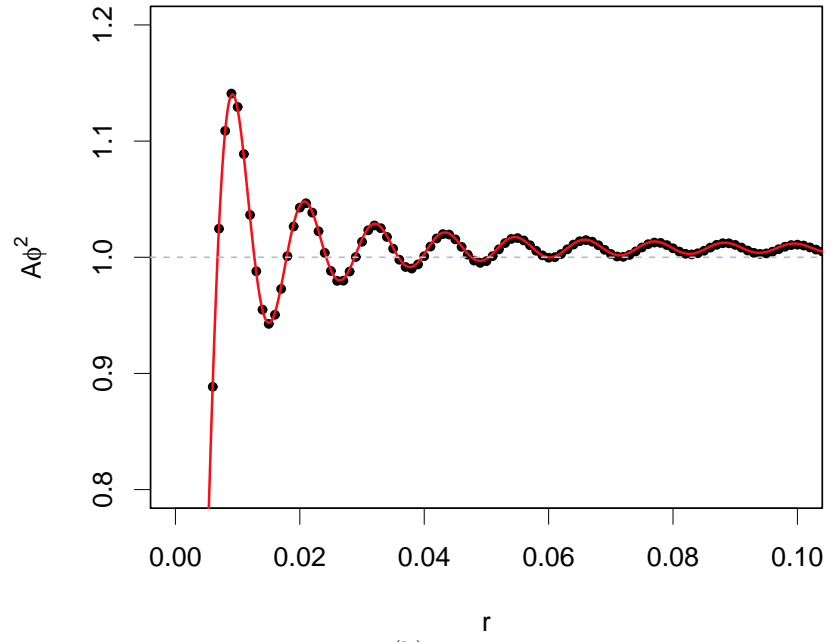
we average over k^2 from 0 to k_M^2

$$\langle \sigma^2(\mathbf{r}_i) \rangle = \frac{\int_0^{k_M^2} C(\mathbf{r}_i, \mathbf{r}_i, k) \rho(k^2) dk^2}{\int_0^{k_M^2} \rho(k^2) dk^2}, \quad (\text{D.10})$$

and replace $\sigma^2(\mathbf{x})$ in Eq. (3.30). In Fig. D.1, the semiclassical correction predict the average eigenfunction density over k^2 agree with numerical calculated 23,072 stadium eigenfunctions pretty well



(a)



(b)

Figure D.1: (a) Stadium Billiard (b) Comparison between (Black Dots) average over $n = 1, \dots, 23072$ of numerical calculated $\phi_n^2(r)$ and (red curves) Eq. (D.10).

Appendix E

Lorentzian Distribution of the Regular Normalized Impedance

Consider the normalized impedance,

$$\Xi_{ij} = -\frac{1}{\pi} \sum_{n=1}^N \frac{w_{ni}w_{nj}}{\tilde{k}^2 - \tilde{k}_n^2}, \quad (\text{E.1})$$

where (w_{ni}, w_{nj}) are bivariate random variables with probability density function (PDF) $f_{ij}(w_{ni}, w_{nj})$, and \tilde{k}_n^2 are independent random variables distributed uniformly on $(0, \tilde{k}_N^2)$, i.e., the PDF is $f_{\tilde{k}^2}(\tilde{k}^2) = 1/\tilde{k}_N^2$. Let

$$\xi_{n,ij} = -\frac{1}{\pi} \frac{w_{ni}w_{nj}}{\tilde{k}^2 - \tilde{k}_n^2}, \quad (\text{E.2})$$

such that

$$\Xi_{ij} = \sum_n \xi_{n,ij}. \quad (\text{E.3})$$

The PDF, $f_{\Xi}(z)$, and the characteristic function of Ξ , $\Phi_{\Xi}(t)$ are given by

$$f_{\Xi}(z) = \int d\xi_1 \dots d\xi_N \prod_{n=1}^N f_{\xi}(\xi_n) \delta(z - \sum_{n'} \xi_{n'}), \quad (\text{E.4})$$

$$\Phi_{\Xi}(t) = \int d\xi_1 \dots d\xi_N \prod_{n=1}^N f_{\xi}(\xi_n) \exp(it \sum_{n'} \xi_{n'}) = [\Phi_{\xi}(t)]^N, \quad (\text{E.5})$$

where $f_{\xi}(\xi_n)$ is the PDF of ξ and $\Phi_{\xi}(t) = \int d\xi_n \exp(it\xi_n) f_{\xi}(\xi_n)$ is the characteristic function of ξ . We can calculate $\Phi_{\xi}(t)$ by directly evaluating the integral,

$$\begin{aligned} \Phi_{\xi}(t) &= \int dw_{ni} dw_{nj} f_{ij}(w_{ni}, w_{nj}) \\ &\quad \times \int_0^{\tilde{k}_N^2} d\tilde{k}_n^2 \frac{1}{\tilde{k}_N^2} \exp\left(-it \frac{1}{\pi} \frac{w_{ni}w_{nj}}{\tilde{k}^2 - \tilde{k}_n^2}\right). \end{aligned} \quad (\text{E.6})$$

For small values of t , relevant in the limit $N \gg 1$, the second integral of (E.6) is

$$\begin{aligned} & \frac{1}{\tilde{k}_N^2} \int_0^{\tilde{k}_N^2} d\tilde{k}_n^2 \exp\left(-it \frac{1}{\pi} \frac{w_{ni}w_{nj}}{\tilde{k}^2 - \tilde{k}_n^2}\right) \\ &= 1 + \frac{|t||w_{ni}w_{nj}|}{\tilde{k}_N^2} - it \frac{1}{\pi} \frac{w_{ni}w_{nj}}{\tilde{k}_N^2} \log \left| \frac{\tilde{k}^2}{\tilde{k}_N^2 - \tilde{k}^2} \right| + O(t^2), \end{aligned} \quad (\text{E.7})$$

which to first order in t yields

$$\begin{aligned} \Phi_\xi(t) &\approx \int dw_{ni} dw_{nj} f_{ij}(w_{ni}, w_{nj}) \\ &\quad \times \left(1 + \frac{|t||w_{ni}w_{nj}|}{\tilde{k}_N^2} - it \frac{1}{\pi} \frac{w_{ni}w_{nj}}{\tilde{k}_N^2} \log \left| \frac{\tilde{k}^2}{\tilde{k}_N^2 - \tilde{k}^2} \right| \right) \\ &= 1 - \frac{1}{\tilde{k}_N^2} \left(-it \frac{E\{w_{ni}w_{nj}\}}{\pi} \log \left| \frac{\tilde{k}^2}{\tilde{k}_N^2 - \tilde{k}^2} \right| \right. \\ &\quad \left. + |t|E\{|w_{ni}w_{nj}|\} \right), \end{aligned} \quad (\text{E.8})$$

where $E\{\cdots\} = \int \cdots f_{ij}(w_{ni}, w_{nj}) dw_{ni} dw_{nj}$. Now, we calculate $\Phi_\Xi(t)$; since the mean spacing between adjacent \tilde{k}_n^2 is normalized to unity, we can replace \tilde{k}_N^2 in (E.8) by N and insert it into (E.5). As $N \rightarrow \infty$, we obtain

$$\begin{aligned} \Phi_\Xi(t) &= \left[1 - \frac{1}{N} \left(-it \frac{E\{w_{ni}w_{nj}\}}{\pi} \log \left| \frac{\tilde{k}^2}{\tilde{k}_N^2 - \tilde{k}^2} \right| \right. \right. \\ &\quad \left. \left. + |t|E\{|w_{ni}w_{nj}|\} \right) \right]^N \\ &\rightarrow \exp \left(it \frac{E\{w_{ni}w_{nj}\}}{\pi} \log \left| \frac{\tilde{k}^2}{\tilde{k}_N^2 - \tilde{k}^2} \right| - |t|E\{|w_{ni}w_{nj}|\} \right). \end{aligned} \quad (\text{E.9})$$

Comparing with the characteristic function of a Lorentzian RV with mode x_0 and width W , $\Phi(t) = \exp(itx_0 - W|t|)$, we know Ξ_{ij} is Lorentzian distributed with mode $E\{w_{ni}w_{nj}\}(\log|\tilde{k}^2| - \log|\tilde{k}_N^2 - \tilde{k}^2|)/\pi$ and width $E\{|w_{ni}w_{nj}|\}$. Since the spacing distribution of \tilde{k}_n^2 for regular systems is exponential distributed, as $N \rightarrow \infty$, the distribution of \tilde{k}_n^2 is uniformly distributed in $(0, N)$; thus, the normalized impedance

of regular systems are also Lorentzian distributed and all the system specific informations are included in mode and width of the Lorentzian.

Bibliography

- [1] F. Haake, *Quantum Signature of Chaos* (Springer-Verlag, New York, 2001).
- [2] M. C. Gutzwiller, *Chaos in Classical and Quantum Mechanics* (Springer-Verlag, New York, 1990).
- [3] H.-J. Stöckmann, *Quantum Chaos: An Introduction* (Cambridge University Press, Cambridge, 1999).
- [4] R. Blumel, W. P. Reinhardt, *Chaos in Atomic Physics* (Cambridge University Press, Cambridge, 1997).
- [5] E. Ott, *Dynamical Systems* (Cambridge University Press, Cambridge, 2002).
- [6] E. P. Wigner, Ann. Math. **53**, 36 (1951)
- [7] E. P. Wigner, Ann. Math. **62**, 548 (1955)
- [8] E. P. Wigner, Ann. Math. **65**, 203 (1957)
- [9] E. P. Wigner, Ann. Math. **67**, 325 (1958)
- [10] R. G. Newton, *Scattering theory of waves and particles* (McGraw-Hill, New York, 1966).
- [11] V. Pagneux and A. Maurel, Phys. Rev. Lett. **86**, 1199 (2001).
- [12] E. Doron, U. Smilansky, and A. Frenkel, Phys. Rev. Lett. **65**, 3072 (1990)
- [13] P. W. Brouwer and C. W. J. Beenakker, Phys. Rev. B **55**, 4695 (1997)
- [14] U. Kuhl, M. Martínez-Mares, R. A. Méndez-Sánchez, and H.-J. Stöckmann, Phys. Rev. Lett. **94**, 144101 (2005)
- [15] S. Hemmady, X. Zheng, E. Ott, T. M. Antonsen, and S. M. Anlage, Phys. Rev. Lett. **94**, 014102 (2005)
- [16] Y. Alhassid, , Rev. Mod. Phys. **72**, 895 (2000)
- [17] C. W. J. Beenakker, Rev. Mod. Phys. **69**, 731 (1997)

- [18] P. A. Mello, P. Pereyra, and T. H. Seligman, *Annals of Physics* **161**, 254 (1985)
- [19] P. W. Brouwer, *Phys. Rev. B* **51**, 16878 (1995)
- [20] D. V. Savin, Y. V. Fyodorov, and H.-J. Sommers, *Phys. Rev. E* **63**, 035202 (2001)
- [21] R. A. Méndez-Sánchez, U. Kuhl, M. Barth, C. H. Lewenkopf, and H.-J. Stöckmann, *Phys. Rev. Lett.* **91**, 174102 (2003)
- [22] M. J. Davis and E. J. Heller, *J. Chem. Phys.* **75** 246 (1981).
- [23] J. D. Hanson, E. Ott, and T. M. Antonsen, *Phys. Rev. A* **29**, 819 (1984)
- [24] T. Geisel, G. Radons, and J. Rubner, *Phys. Rev. Lett.* **57**, 2883 (1986)
- [25] W. A. Lin and L. E. Ballentine, *Phys. Rev. Lett.* **65**, 2927 (1990)
- [26] O. Bohigas, S. Tomsovic, and D. Ullmo, *Phys. Rev. Lett.* **64**, 1479 (1990)
- [27] O. Bohigas, S. Tomsovic, and D. Ullmo, *Physics Reports* **223**, 43 (1993)
- [28] S. Tomsovic and D. Ullmo, *Phys. Rev. E* **50**, 145 (1994)
- [29] E. Doron and S. D. Frischat, *Phys. Rev. Lett.* **75**, 3661 (1995)
- [30] D. A. Steck, W. H. Oskay, and M. G. Raizen, *Science* **293**, 274 (2001)
- [31] M. Sheinman, S. Fishman, I. Guarneri, and L. Rebuzzini, *Phys. Rev. A* **73**, 052110 (2006)
- [32] S. Löck, A. B äcker, R. Ketzmerick, and P. Schlagheck, *Phys. Rev. Lett.* **104**, 114101 (2010)
- [33] M. Wilkinson and J. Hannay, *Physica D* **27**, 201 (1987)
- [34] S. C. Creagh and N. D. Whelan, *Phys. Rev. Lett.* **77**, 4975 (1996)
- [35] S. C. Creagh and N. D. Whelan, *Phys. Rev. Lett.* **82**, 5237 (1999)
- [36] S. C. Creagh and N. D. Whelan, *Ann. Phys.* **272**, 196 (1999)

- [37] S. C. Creagh and N. D. Whelan, Phys. Rev. Lett. **84**, 4084 (2000)
- [38] M. C. Gutzwiller, Phys. Rev. Lett. **45**, 150 (1980)
- [39] H. Weyl, Nachr. Akad. Wiss. Göttingen, **110** (1911)
- [40] O. Bohigas, M. J. Giannoni and C. Schmit, Phys. Rev. Lett., **52**, 1 (1984)
- [41] M. V. Berry and M. Tabor, Proc. R. Soc. London A **365**, 375 (1977)
- [42] I. C. Percival, J. Phys. B: Atom. and Mol. **6**, L229 (1973)
- [43] M. V. Berry, and M. Robnik, Journal of Physics A: Mathematical and General **17**, 2413 (1984)
- [44] M. V. Berry, J. Phys. A **10**, 2083 (1977).
- [45] M.-J. Lee, T. M. Antonsen, E. Ott, and L. M. Pecora Phys. Rev. E **86**, 056212 (2012)
- [46] M.-J. Lee, T. M. Antonsen, and E. Ott Phys. Rev. E **87**, 062906 (2013)
- [47] L. M. Pecora, H. Lee, D.-H. Wu, T. Antonsen, M.-J. Lee, and E. Ott, Phys. Rev. E **83**, 065201 (2011)
- [48] C. Herring, Rev. Mod. Phys. **34**, 631 (1962)
- [49] R. Balian and C. Bloch, Ann. Phys. **60**, 401 (1970)
- [50] R. Balian and C. Bloch, Ann. Phys. **63**, 592 (1971)
- [51] R. Balian and C. Bloch, Ann. Phys. **64**, 401 (1971)
- [52] R. E. Prange, E. Ott, T. M. Antonsen, B. Georgeot, and R. Blümel, Phys. Rev. E **53**, 207 (1996)
- [53] M. V. Berry, Proc. Roy. Soc. London A **423**, 219 (1989).
- [54] T. M. Antonsen, E. Ott, Q. Chen, and R. N. Oerter, Phys. Rev. E **51**, 111 (1995).
- [55] E. Bogomolny, Physica D: Nonlinear Phenomena **31**,169 (1988)

- [56] D. Ullmo, S. Tomsovic, and A. Bäcker, Phys. Rev. E **79**, 056217 (2009)
- [57] X. Zheng, Ph.D. thesis, University of Maryland (2005)
- [58] T. M. Antonsen X. Zheng and E. Ott, Electromagnetics **26**, 3 (2006)
- [59] T. M. Antonsen X. Zheng and E. Ott, Electromagnetics **26**, 37 (2006)
- [60] L. A. Bunimovich, Chaos **11**, 802 (2001)
- [61] J. D. Meiss, and E. Ott Phys. Rev. Lett. **55**, 2741 (1985)
- [62] L. A. Bunimovich, Comm. Math. Phys., **65**, 295 (1979).
- [63] A. H. Barnett, Commun. Math. Phys. **59**, 1457 (2006)
- [64] T. Prosen, and M. Robnik, Journal of Physics A: Mathematical and General **26**, 5365 (1993)
- [65] B. Li and M. Robnik, Journal of Physics A: Mathematical and General **28**, 4843 (1995)
- [66] Y.-C. Lai, R. Blümel, E. Ott, and C. Grebogi, Phys. Rev. Lett. **68**, 3491 (1992)
- [67] R. Ketzmerick, Phys. Rev. B **54**, 10841 (1996)
- [68] A. M. Chang, H. U. Baranger, L. N. Pfeiffer, and K. W. West, Phys. Rev. Lett. **73**, 2111 (1994)
- [69] A. Bäcker, R. Ketzmerick, S. Löck, and H. Schanz, Eur. Phys. J. **94**, 30004 (2011)
- [70] A. Bäcker and R. Schubert, J. Phys. A: Math. and Gen. **35**, 527 (2002)
- [71] A. H. Barnett and T. Betcke, Chaos **17**, 043125 (2007)
- [72] R. W. Robinett, Am. J. Phys. **64**, 440 (1996)
- [73] E. Vergini and M. Saraceno, Phys. Rev. E **52**, 2204 (1995)
- [74] A. Barnett, D. Feng, J. Steed, and L. Goldfarb, Comput. Phys. Commun. **8**, 377 (1974)

- [75] J. B. Keller and S. I. Rubinow, Ann. of Phys. **9**, 24 (1960)
- [76] J. B. Keller and S. I. Rubinow, Ann. of Phys. **10**, 303 (1960)
- [77] E. J. Heller , Phys. Rev. Lett. **53**, 1515 (1984)
- [78] J. D. Urbina and K. Richter, Eur. Phys. J. Special Topics **145**, 255 (2007)
- [79] M. Srednicki, Phys. Rev. E **54**, 954 (1996)
- [80] B. Dietz, T. Friedrich, M. Miski-Oglu, A. Richter, and F. Schäfer, Phys. Rev. E **75**, 035203 (2007)
- [81] A. Bäcker, R. Ketzmerick, S. Löck, M. Robnik, G. Vidmar, R. Höhmann, U. Kuhl and H.-J. Stöckmann, H.-J., Phys. Rev. Lett. **100**, 174103 (2008)
- [82] S. Hortikar and M. Srednicki, Phys. Rev. Lett. **80**, 1646 (1998)
- [83] A. H. Barnett, Ph.D. thesis, Harvard University (2000)